PROBING FISSION TIME SCALES AND DYNAMICS VIA GDR γ RAYS AND NEUTRON ANGULAR DISTRIBUTIONS

A Dissertation

by

TYE WILLIAM BOTTING

Submitted to the Office of Graduate Studies of
Texas A&M University
in partial fulfillment of the requirements for the degree of

DOCTOR OF PHILOSOPHY

December 1999

Major Subject: Chemistry

PROBING FISSION TIME SCALES AND DYNAMICS VIA GDR γ RAYS AND NEUTRON ANGULAR DISTRIBUTIONS

A Dissertation

by

TYE WILLIAM BOTTING

Submitted to Texas A&M University
in partial fulfillment of the requirements
for the degree of

DOCTOR OF PHILOSOPHY

Approved as to style and content by:

Richard P. Schmitt (Chair of Committee)	Joseph B. Natowitz (Member)
Che-Ming Ko (Member)	Rand L. Watson (Member)
	Emile A. Schweikert (Head of Department)

December 1999

Major Subject: Chemistry

PROBING FISSION TIME SCALES AND DYNAMICS VIA GDR γ RAYS AND NEUTRON ANGULAR DISTRIBUTIONS

A Dissertation

by

TYE WILLIAM BOTTING

Submitted to Texas A&M University
in partial fulfillment of the requirements
for the degree of

DOCTOR OF PHILOSOPHY

Approved as to style and content by:

Richard P. Schmitt
(Chair of Committee)

Joseph B. Natowitz
(Member)

Che-Ming Ko
(Member)

Rand L. Watson
(Member)

Emile A. Schweikert
(Head of Department)

December 1999

Major Subject: Chemistry

TEXAS A&M UNIVERSITY

Office of Graduate Studies

REPORT OF THE FINAL EXAMINATION FOR DOCTORAL CANDIDATES

The undersigned duly appointed examining committee has conducted the final examination of TYE WILLIAM BOTTING 465-57-5024

candidate for the degree of DOCTOR OF PHILOSOPHY

with a major in CHEMISTRY

We have examined the candidate's area(s) of specialization, and so far as can be determined from such examination, we **(do)** ~~**(do not)**~~† consider that the candidate has fulfilled this part of the University's requirement for the degree.

†Please strike through the inappropriate words in bold face.

Date Oct. 29, 1999 Signed _____ Chair

_____ Co-Chair

_____ Member

_____ Member

_____ Member

_____ Member

_____ GCR

I hereby **(do)** ~~**(do not)**~~† authorize all Incomplete (I) grades for 691/692/684 coursework for which the above-named student enrolled be changed to Satisfactory (S).

†Please strike through the inappropriate words in bold face.

Signed _____ Chair

_____ Co-Chair

In compliance with the Texas Open Records Law, the student will be allowed to review this form upon written request.

PLEASE MAKE A COPY FOR YOUR RECORDS AND RETURN ORGINAL TO THE OFFICE OF GRADUATE STUDIES

ABSTRACT

Probing Fission Time Scales and Dynamics via GDR γ Rays

and Neutron Angular Distributions. (December 1999)

Tye William Botting, B.S., Texas A&M University

Chair of Advisory Committee: Dr. Richard P. Schmitt

This dissertation presents a study of fission dynamics and time scales for the following reactions; 133 MeV ^{16}O + ^{208}Pb, 104 MeV ^{4}He + ^{209}Bi, 133 MeV ^{16}O + ^{176}Yb, and 104 MeV ^{4}He + ^{188}Os. Two disparate means were utilized: fission coincidence measurements of pre- and post-scission neutrons and of γ rays. These measurements were accomplished simultaneously and analyzed similarly, so as to minimize experimental differences and systematic model-dependent biases.

Fission fragments were detected via large x-y position-sensitive parallel plate avalanche counters (PPAC's) mounted in compact geometry to maximize their geometric efficiency. The fission fragment emission angles and relative velocities were used to reconstruct masses via standard kinematics.

The γ rays were detected by 144 BaF_2 crystals from the U. S. Barium Fluoride Array (BFA). These detectors were arranged into two pods of 72 crystals placed at backward angles to minimize the neutron flux. The high granularity made it possible to reconstruct the event showers to obtain the total energy deposited by each detected γ ray. The reconstructed energy spectra were then analyzed in the giant dipole resonance (GDR) region with the aid of statistical model calculations,

giving the time scales for fission, τ_{fiss_γ}. From the γ-ray data, the time scales obtained for the reactions ^{16}O + ^{208}Pb, ^{4}He + ^{209}Bi, and ^{16}O + ^{176}Yb were τ_{fiss_γ}= 67 $\pm$ 10 zs, 45 $\pm$ 9 zs, and 84 $\pm$ 16 zs, respectively.

Neutrons were detected by 8 liquid scintillator detectors from the DEMON Array, which were positioned around the target to ensure separation of neutrons and γ rays and to obtain the multiplicities of pre- and post-scission neutrons. With the help of statistical model calculations, these multiplicities were also analyzed to extract the fission time scales, τ_{fiss_n}. From the neutron data, the time scales obtained for the reactions ^{16}O + ^{208}Pb, ^{4}He + ^{209}Bi, ^{16}O + ^{176}Yb, and ^{4}He + ^{188}Os were τ_{fiss_n}= 105 $\pm$ 10 zs, 72 $\pm$ 7 zs, 112 $\pm$ 12 zs, and 31 $\pm$ 4 zs, respectively.

DEDICATION

To my family, Shaleen and Kira, and to my parents, Neil and Michal

ACKNOWLEDGMENTS

I am extremely grateful for the support and encouragement provided by my advisor, Richard P. Schmitt, as well as for his guidance and patience. This work could not have been completed without his thoughtful input and his valuable expertise.

The assistance of Greg Chubarian has been invaluable. His efforts in the fission analysis are especially appreciated, as are his continual help and instructive conversations. I also sincerely appreciate all his time and hard work in the construction and maintenance of the fission fragment detectors. Thanks also go out to Vladimir Salamatin, for his custom PPAC analysis code, which was instrumental in the analysis.

Very special thanks go out to the late Kevin L. Wolf for his insightful comments and suggestions both during these experiments and in the early stages of the analysis. He will be sorely missed.

During the experiment, members of the DEMON collaboration were invaluable in providing and taking care of the neutron detectors. They also made available the use of their optimized analysis code for DEMON in the neutron analysis. The Dubna group, especially Nikolai Kondratiev and Igor Pokrovski, were very helpful with regards to the non-BaF_2 electronics and reaction chamber, respectively. The ORNL people, especially Robert Varner, Mel Halbert and Ning Gan, were instrumental in optimizing the performance of the BaF_2 detectors and their associated electronics. I thank each and every one of these people here.

Thanks also are due Kris Hagel for his valuable and tireless computer help, and in particular his help with the analysis code LISA.

I also wish to thank my committee members for their continual support and patience. Their inputs regarding the analysis and the preparation of this manuscript have been invaluable.

The financial support from the Department of Energy and the Welch Foundation is most gratefully acknowledged.

Finally, the support over the years from my wife and my parents was unending and is certainly deserving of its own award. Without such support, none of this would have been possible.

TABLE OF CONTENTS

CHAPTER Page

LIST OF TABLES

TABLE Page

LIST OF FIGURES

FIGURE Page

FIGURE Page

FIGURE Page

CHAPTER I

INTRODUCTION

I.1 Overview

Some of the most spectacular developments in the nuclear sciences have been the events leading to the discovery of nuclear fission in the late 1930's [1–4]. This dramatically showed that an atom of one element could cataclysmically rearrange into wholly separate and different atoms. The most widely used tool for understanding this behavior is the liquid drop model of the nucleus [3, 5]. Fission has influenced all of our lives individually and on a global scale. The socio-economic implications of fission cannot be overstated, ranging from alternative power sources to the problems of nuclear waste disposal.

In contradistinction to outward manifestations such as the "cold war" and its various backlashes, fission remains an exceedingly interesting process from a scientific perspective. In spite of all the work on fission motivated by everything from greed to world domination, fission has always remained a mysterious process. A deeper understanding of fission will improve our knowledge of nuclear processes in the short term, but from a more general perspective, will enhance our understanding of many-body systems. The latter is obviously the major reason for the study of fission.

This dissertation follows the style and format of Physical Review C.

Over the years [6] the relative importance of the dynamical and statistical nature of fission has been hotly debated. A dynamical process is sensitive to the initial conditions in which the system was produced. Its subsequent time evolution is governed by equations of motion such as Hamilton's equations or the Schödinger equation. In contrast, a statistical process treats all possible time evolutions of the system on an equal footing. In the vernacular, a dynamical behavior reflects a strong governing force, such as a monarchy, while statistical evolution represents total democracy. Using scientific terms, dynamical processes involve specific phases of motion while statistical processes place all phases of motion on an equal basis.

In many respects, the division between the two approaches is artificial. There is little doubt that fission is inherently a dynamical process. The real questions are how well can fission be described by statistical models and when must dynamical effects necessarily be taken into account.

One of the major tests of the relative strengths of the dynamical and statistical contributions in fission involves the measurement of fission time scales. Such information gives valuable insight into the types and relative importance of dissipation of collective excitation into internal degrees of freedom, i. e. friction or damping. Of course, friction is a somewhat artificial term which addresses the relevancy of the overall collective participation of many nucleons. Nevertheless, it is very useful for describing the coupling between the behavior of single nucleonic and collective motion.

The remainder of this introduction will focus on specific aspects of fissioning systems, especially in regard to the time scale. The next section presents a brief

review of fission time scales and basic considerations in their study. This is followed by discussion of the methodologies used for investigating fission time scales, including the history and theoretical bases. Finally, a brief summary will review what can be learned by comparing and contrasting these two methods.

I.2 Review of Fission Time Scales

Over the years, fission time scales have mainly been determined from neutron emission accompanying fission [7–14]. Studies have also been conducted using light charged particle emission [15–22] and giant dipole resonance γ-ray emission [23–32]. Some newer studies have utilized the method of crystal blocking for very asymmetric entrance channels and inverse kinematics [33]. Using the various decay modes to measure fission time scales has met with limited success. In particular, the time scales obtained by the various methods have differed by an order of magnitude or more [14, 34, 33]. This puzzling situation indicates that further work is needed to reconcile these differences. The work discussed here is intended to distinguish effects attributable to experimental techniques, the underlying physics, and systematic model analyses. This should provide a better understanding of the physics involved. Two of the major tools for determining the time scale for the fission process have been employed here: neutron emission and giant dipole γ-ray emission.

When two nuclei collide and fuse, the resulting compound nucleus can decay through a variety of channels. Frequently the system decays through emission of neutrons, γ rays, charged particles, and by fission. At any given time in the decay process, each of these will compete with each other according to their decay widths,

Γ (see below). In the case of fission, the daughter nuclei can also be sufficiently excited to decay by these modes, although a second fission is very unlikely at modest excitation energies ($\approx$100-200 MeV).

Neutrons emitted from the compound nucleus, i.e. before scission, have an essentially isotropic distribution in the center of mass frame, whereas those emitted from the fission fragments are kinematically focussed in the direction of their fragment of origin. Thus, separation of the isotropic component from the focussed component in the neutron angular distribution leads to pre- and post-scission neutron multiplicities (ν_{pre} and ν_{post}), respectively. Similarly, giant dipole resonance γ rays emitted from the compound system and the daughter fragments can be recognized by their different energies.

The giant dipole resonance (GDR) is a strongly collective mode of excitation wherein protons and neutrons oscillate out of phase with respect to each other. This oscillation of charge creates an electric dipole. This is discussed in greater detail in Section I.3.

Being a collective mode of excitation involving nearly all nucleons, γ rays from the GDR are typically quite high in energy. For a GDR built on the nuclear ground state, the energy spectrum peaks at about

$$E = \frac{79}{A^{1/3}}, \tag{1}$$

where A is the mass number [35]. For a nucleus with mass around 220 amu, this corresponds to about 13 MeV. In contrast, the peak energies from symmetric fission fragments should be about 3.5 MeV higher. A fit to the overall energy spectrum thus

provides the relative number of each, from which an estimate to the time scales of fission can be derived.

In the case of neutron measurements, the time for fission can be approximated by a sum of time scales of several different processes. This can be written as [36]

$$\tau = \tau_{form} + \tau_{sadd} + \tau_{scis} + \tau_{acc}, \tag{2}$$

where τ_{form} is the time associated with the formation of the compound nucleus, τ_{sadd} is the time required to achieve quasi-static equilibrium at the saddle point, τ_{scis} is the time for the system to evolve to scission, and τ_{acc} is the time for the fragments to gain most of their asymptotic velocities. The last term is technically not part of the fission time scale, but is included because neutrons emitted by the fragments before they have attained their asymptotic velocities are indistinguishable from neutrons emitted by the compound nucleus. Analogously, for GDR γ-ray measurements the form would be

$$\tau = \tau_{form} + \tau_{sadd} + \tau_{scis}. \tag{3}$$

Note that τ_{acc} is not present in the time scale given by analysis of GDR γ-ray data simply because the energies of the GDR γ rays are dependent upon the shape and size of the nucleus. Once fission has occurred, any GDR γ rays observed from the fragments will have higher energies than those from the parent system.

The quantity τ_{sadd} is of special interest, as it is identified with the so-called fission time delay or transient time [37]. Determination of this quantity is expected to provide the value of the nuclear viscosity. Following Kramers' work in 1940 the

values for the effective fission decay width including dissipative effects should be smaller than the standard Bohr-Wheeler decay width [5] according to the viscosity of the system [38], i. e.

$$\Gamma_{eff} = \Gamma_{BW}(\sqrt{1+\gamma^2} - \gamma), \tag{4}$$

where Γ_{eff} is the effective decay width, γ is the nuclear friction constant, and Γ_{BW} is the Bohr-Wheeler decay width. This expression for the dissipative fission width has become a cornerstone for many works on nuclear time scales.

Ideally, one would like to determine experimentally each of the contributions to the fission time separately. So far this has not been achieved reliably. One might be able to set some limits on τ_{form} by forming the same compound nucleus through different entrance channels, as in the 133 MeV ^{16}O + ^{176}Yb and the 104 MeV ^{4}He + ^{188}Os cases investigated here. For a lighter projectile τ_{form} should be shorter simply due to the lessened importance of dynamical complications in the entrance channel, e. g. neck formation, diffusion, and viscosity. This would be reflected in the measurements as smaller values of the pre-fission neutron multiplicity, ν_{pre}, and a reduced yield of pre-fission GDR γ rays. Similarly, it might be possible to gain insight into τ_{acc} by comparing the τ's from the two techniques. A complication with this approach is that the nascent fragments in the vicinity of scission can be quite deformed. Some additional time is required for the fragments to shape equilibrate.

The separation of τ_{sadd} and τ_{scis} has proven to be a tricky business. In some early works, deviations in the yield of pre-fission neutrons and γ rays from statistical model predictions were used as a measure of τ_{sadd} [39, 40]. However, it is now clear that

failure of statistical models to reproduce ν_{pre} does not necessarily mean that there is a significant time delay before the system reaches the saddle. Conventional statistical model codes do not account for neutron evaporation during fission. Neutrons emitted during both time intervals cannot be separated kinematically. This has prompted the use of other approaches, such as studies of the mass distributions [21, 41, 42], fission excitation functions [43–47], and evaporation residue cross sections [48]. Still, there is no consensus on τ_{sadd}. Possibly more constrained measurements and analyses, such as those presented here, will offer some new insight into the problem. Even if they do not, they should yield a better determination of the overall fission time.

I.3 Statistical Approach to Neutron Evaporation and Fission Time Scales

The evaporation of neutrons from excited nuclei has been studied for many years. Our knowledge of neutron emission has proven to be a valuable tool in estimating excitation energies [49–51], momentum transfer [52], time scales [7–14], and other properties of excited nuclei. This has mainly been accomplished with the aid of the statistical model of nuclear decay.

From first order perturbation theory the decay rate, Γ, of any quantum system, such as an excited nucleus, should follow Fermi's second golden rule [53],

$$\Gamma = \frac{2\pi}{\hbar}|\langle\psi_f|Op|\psi_i\rangle|^2\rho(E_{final}), \tag{5}$$

where $\langle\psi_f|Op|\psi_i\rangle$ is the nuclear matrix element for the transition, $|M_{if}|$, and $\rho(E_{final})$ is the number of final states per unity energy, i. e. the density of final states.

The operator Op depends on the nature of the transition. The ψ's incorporate all "knowable" information about the initial and final states. For transitions between

specific states (the low excitation energy regime), ρ is often easy to calculate. In contrast, for many-body systems, the ψ's can only be approximated, usually with considerable effort. At excitation energies where many initial and final states are possible (high excitation regime), the reverse is true. In this case, the effects of the M_{if}'s are washed out, making ρ the determining factor in Γ. Such is the case in the systems studied here.

Specific examples of Γ for statistical decay are abundant in the literature [5, 54, 55], to which the reader is also referred. If there are many modes of decay, the total decay width is simply the sum of the Γ's over all the n available decay widths,

$$\Gamma_{tot} = \sum_{i=1}^{n} \Gamma_i. \tag{6}$$

The density of final states is a function of the final excitation energy so it can be considered as the density of initial excitation energy minus all energy consumed in the decay, i. e.

$$\Gamma_i \propto \rho(E_{final}) = \rho(E^* - E_i), \tag{7}$$

where E^* is the excitation energy of the emitting system and E_i is all energy taken away by decay mode i. The quantity E_i is the sum of the binding energy of the evaporated particle, S_i, and its kinetic energy, ϵ. The total width for evaporating i is obtained by integrating over ϵ. In what follows, it will be assumed that this integration has been performed.

The branching ratio, or relative probability, of each mode is defined as the ratio of the decay width of that mode to the total decay width,

$$\frac{\Gamma_i}{\Gamma_{tot}} \approx \frac{\rho(E^* - E_i)}{\sum_{j=1}^{n} \rho(E^* - E_j)}, \tag{8}$$

letting the leading constants cancel out. This can be related through the Bohr hypothesis to a partial cross section for a given decay mode by [55]

$$\sigma_i = \sigma_{CN}\frac{\Gamma_i}{\Gamma_{tot}}, \tag{9}$$

where σ_{CN} is the cross section for compound nucleus formation.

Expansion of the term $\rho(E^* - E_i)$ in Equation (8) to the second term gives

$$\ln\rho(E^* - E_i) = \ln\rho(E^*) - \frac{d\ln\rho(E^*)}{dE}E_i - \ldots. \tag{10}$$

As in thermodynamics, this satisfies the relation,

$$\frac{d\ln\rho}{dE} = \frac{dS}{dE} = \frac{1}{T}, \tag{11}$$

which defines the nuclear entropy, S, and the temperature, T. After neglecting higher order terms, Equation (10) can be rewritten,

$$\rho(E^* - E_i) \approx \rho(E^*)e^{-E_i/T}. \tag{12}$$

Finally, combining this equation with the expression for the branching ratio, from Equation (8), yields

$$\frac{\Gamma_i}{\Gamma_{tot}} \approx \frac{e^{-E_i/T}}{\sum_{j=1}^{n} e^{-E_j/T}}, \tag{13}$$

after canceling out the like terms $\rho(E^*)$. In the case of the systems considered here, the main contributors are neutron evaporation, light charged particle (LCP) evaporation, GDR γ-ray decay, and fission. Thus, the branching ratio for a given type of decay can be expressed

$$\frac{\Gamma_i}{\Gamma_{tot}} \approx \frac{e^{-E_i/T}}{e^{(-S_n-2T)/T} + e^{-E_{LCP}/T} + e^{-E_\gamma/T} + e^{-B_f/T}}, \tag{14}$$

where S_n is the separation energy of a neutron, and B_f is the fission barrier. Since the denominator is a sum of exponentials, only the largest terms will contribute significantly. For the reactions studied here, $T \approx$ 1.7–2.2 MeV, $S_n \approx$ 7–10 MeV, $E_{LCP} \approx$ 20-25 MeV, $E_\gamma \approx$ 10–14 MeV, and $B_f \approx$ 5–16 MeV, depending on the system and the assumptions made. Thus, Equation (14) can be further simplified to

$$\frac{\Gamma_i}{\Gamma_{tot}} \approx \frac{e^{-E_i/T}}{e^{(-S_n-2T)/T} + e^{-B_f/T}}. \tag{15}$$

The most prominent term in this expression is usually the neutron evaporation term, especially for low-A or low-angular-momentum nuclei. For systems with B_f considerably greater than S_n, a number of neutrons can be emitted before fission. Thus the total neutron decay width is given by a sum of terms; i. e.

$$\Gamma_n = \Gamma_{n1} + \Gamma_{n2} + \Gamma_{n3} + \ldots, \tag{16}$$

where Γ_{nj} is the partial width for decay at the j^{th} step. A similar expression holds for fission.

It should be noted that Equations (12)–(15) assume a constant T and neglect a variety of factors. Obviously, T varies throughout the decay chain, so these equations give only a qualitative description. This is nonetheless useful. More accurate expressions for the branching ratio can be found in the literature [6, 55].

Another important point that is not obvious in the above treatment is that the fission width is calculated in a different way than the other decay widths. For evaporation, Γ is calculated for a final state in which the decay products are separated by an infinite distance. In contrast, Γ_f is generally evaluated at the top of the fission

barrier, B_f. This is the so-called Bohr-Wheeler transition state approach, which will be further discussed below.

The lifetime for a decay mode is related to its decay width through the Heisenberg Uncertainty Principle. For neutron emission

$$\tau_n = \frac{\hbar}{\Gamma_n}. \tag{17}$$

The average pre-fission lifetime for the fissioning nucleus is simply the sum of the lifetimes for neutron decay for each step in the decay,

$$\langle \tau_f \rangle = \sum_i \tau_{n_i}, \tag{18}$$

where i refers to each individual neutron emission before fission.

The determination of the number of pre-scission neutrons is complicated by the fact that neutrons can come from a variety of sources. This includes the decay of the compound nucleus, pre-equilibrium neutrons, and scission neutrons which are emitted when the fission fragments separate. Another complication is that statistical model codes generally ignore the fact that neutrons can be evaporated as the system evolves from saddle to scission. Neutrons can also be emitted during τ_{acc}.

The number of pre-fission, ν_{pre}, and post-fission neutrons, ν_{post}, have been estimated from the neutron angular distributions as already described. However, neutrons emitted at scission or during acceleration will also be emitted essentially isotropically in the center of mass. These neutrons can contribute to the apparent ν_{pre}. Pre-equilibrium neutrons associated with fission are expected to be nearly negligible for the systems considered here.

TABLE 1. Previous results for time scale measurements using the neutron method.

Reaction	Fission time scale (zs)	Reference
216 MeV ^{40}Ar + ^{141}Pr	≈23	[7]
192 MeV ^{12}C + ^{175}Lu	≈50	
220 MeV ^{20}Ne + ^{165}Ho	≈110	
205 MeV ^{36}Ar + ^{169}Tm	10-100	[11]
838 MeV ^{32}S + ^{197}Au,^{232}Th	5-30	[13]
many systems (see ref.)	20-50	[14]
838 MeV ^{32}S + ^{144,154}Sm	≈10	[58]
many systems (see ref.)	≈30	[59]
(180,190,216,249) MeV ^{40}Ar + ^{180}Hf	17-40	[60]

Once ν_{pre} has been determined, various statistical model codes (e. g.Julian [11], Joanne [20], Cascade [56], and Pace [57]) have been used to determine the time required for neutron emission at each step before fission. From this, Equation (18) can give the average pre-fission lifetime of the compound system.

This procedure has been carried out by a number of researchers, as mentioned previously. The consensus of past work is that fission seems to be a much slower process than given by the Bohr-Wheeler formalism [7–14]. A summary of some of the results is given in Table 1. For standard fusion-fission reactions over a range of excitation energies (60-200 MeV) and a wide range of massnumbers (100-250 amu) there is little variation. Fission appears to take on the order of 5-110 zs, where 1 zs = 10^{-21} seconds. This is much longer than previous estimates, by a factor of 10 or more, from a number of statistical model calculations that do not include fission hindrance. The friction coefficient, γ, required for a number of similar neutron analyses seems to

range from 8–50 [9, 36, 59, 61]. (Most of the authors listed in Table 1 did not report γ values.)

The disparity in fission time scales has sparked quite a bit of interest in the field. Explanations for the long fission time include increased nuclear viscosity [39, 62], the increased importance of one- and two-body dissipation [63, 64], and sampling of different portions of the time distribution [33], among other reasons.

I.4 GDR γ Rays and the Fission Time Scale

Before discussing the use of GDR (giant dipole resonance) γ rays to investigate the fission time scale, it is useful to briefly review the emission of these energetic photons. A GDR corresponds to an oscillation of neutrons and protons in the emitting system. There are many other types of GR's (giant resonances) which have been extensively investigated. A GDR γ ray is produced when a γ ray is emitted in the de-excitation of a dipole resonance built on excited nuclear states.

The various GR's are collective modes of nuclear excitation involving the coherent movement of many nucleons within the nucleus. In general, these types of nuclear excitations have been of great interest since they were first discovered (the GDR in 1947 [65] and other multipolarities after 1971 [66]). There are a number of general reviews on the subject [35, 66, 67, 68, 69, 70].

Giant multipole resonances are classified by the type of collective motion. For the GDR the isospin-phase, ΔT, refers to whether protons and neutrons are oscillating against each other (ΔT=1, "isovector") or with (ΔT=0, "isoscalar"). In the isovector oscillation the charge density in the nucleus is in phase, creating a vector of charge

differential along the axis of the oscillation. The other modes and multipolarities can be found in the literature.

The GDR can be understood in either of two ways. In one limit, a sphere of protons can oscillate back and forth against a sphere of neutrons, without conserving the total volume of the nucleus. This is the so-called Goldhaber-Teller (GT) displacement mode [71], which exhibits an energy-dependence proportional to $A^{-1/6}$. In the second mode, imagine an oscillation of the neutrons and protons within a confined volume. This is the so-called Steinwedel-Jensen (SJ) acoustic mode [72], which exhibits an energy dependence proportional to $A^{-1/3}$. In nature, one expects some combination of both modes. In 1975, Berman and Fultz devised an empirical expression similar to that of Equation (1) that accounted for both of these contributions by correlating GDR energy peaks from many experiments [73],

$$E = \frac{31.2}{A^{1/3}} + \frac{20.6}{A^{1/6}}. \tag{19}$$

This shows that neither the acoustic nor the displacement effects dominate the restoring force. Thinking wholly in terms of one or the other type of oscillation is incorrect. However, the GT mode seems to provide a somewhat larger contribution for heavier compound nuclei. Still, over the whole periodic table there is no region where either mode can be said to truly dominate [74].

The associated oscillations of GDR's can decay by a variety of means. These include neutron emission, fission, as well as γ-ray decay. Crude estimates using Equation (13) suggest that GDR γ-ray emission has a probability of 10^{-3}–10^{-4}. If the decay of a GDR by γ-ray emission leads to the ground state, the energy of the

photon corresponds to the excitation energy of that giant resonance. Examples of the A-dependence of this energy are given in Equation (1) and Equation (19). The energy distributions are Lorentzian, with typical widths of 4–5 MeV. The strength of the GDR resonance is expressed in terms of the Thomas-Reiche-Kuhn (TRK) sum rule [75],

$$\int_{0\mathrm{MeV}}^{30\mathrm{MeV}} \sigma_{abs}(E_\gamma)\mathrm{d}E_\gamma \;=\; \frac{2\pi^2 e^2 \hbar}{Mc}\frac{NZ}{A} \;\approx\; \frac{60NZ}{A}(1+\kappa) \qquad \mathrm{MeV{\cdot}mb}, \qquad (20)$$

where $\sigma_{abs}(E_\gamma)$ is the absolute cross-section as a function of γ-ray energy. For the central portion of the equation, M is the mass of a nucleon, c the speed of light, N the number of neutrons, and Z is the atomic number. The value κ is an empirical enhancement factor as deduced from a high-energy photo-absorption tail extending beyond E_γ=100 MeV. Usually, 100% of the TRK sum rule is recovered in GDR studies, though it is not unusual for greater amounts to be used when fitting experimental spectra.

In 1955, Brink first proposed that giant resonances could be built on all excited states [76]. This was somewhat hinted at by early fission γ-ray correlations [77] but was not confirmed until 1981 by Newton *et al.* [78]. This opened the field to many more studies of γ rays from the decay of GDR's built on excited states [35]. A number of these were devoted to the determination of fission time scales [23–32].

GDR γ-ray investigations of the fission time scale also rely on the statistical model of nuclear decay. As mentioned above, the branching ratio for GDR γ-ray emission, $\Gamma_{GDR}/\Gamma_{tot}$, is $\approx$0.1% or less for the reactions considered here. Nevertheless it is possible to observe compound-nucleus GDR γ rays in the fission-correlated γ-ray

TABLE 2. Previous results of time scale measurements using the GDR method.

Reaction	Fission time scale (zs)	Reference
120,140 MeV ^{16}O + ^{208}Pb	≈290	[24]
^{252}Cf (spont. fission)	≈100	[26]
(180-245) MeV ^{32}S + ^{nat}W,^{208}Pb	≈30	[31]
216,238 MeV ^{40}Ar + ^{116}Cd	≈140	[32]
420,600 MeV ^{40}Ar + ^{232}Th	60-200	[79]
120 MeV ^{16}O + ^{208}Pb	96±24	[80]

spectrum. This contribution is visible as a broad enhancement in the region around 11 MeV for the systems considered here (see Chapter III for examples from the current study).

The first studies of GDR γ-ray emission accompanying fission were performed by Thoennessen *et al.*, in 1987 [23]. The reasoning behind their work was that any fission time delay should not only enhance neutron emission but all other available decay modes as well, including GDR γ-ray emission. Their investigations involving ^{224}Th* at various excitation energies did indeed exhibit such an enhancement relative to calculations using their extended version [23] of the statistical code CASCADE [56]. Initially, the modifications to the code assumed that the fission decay width was decreased due to fission dynamics. The factor decreasing Γ_f was termed a fission hindrance factor. In subsequent analyses, the Kramers expression for Γ_f was used to extract the fission time scale. Table 2 lists several of the time scales determined in these and other works using the GDR method. The inferred time scales for fusion-fission reactions from GDR γ-ray studies are on the order of 30–300 zs. This is

significantly longer than the time scales deduced from the neutron studies by more than a factor of three to an order of magnitude. The difference in time scales needs to be investigated to provide a more consistent understanding of the fission time scale and the dynamics of nuclear fission.

The friction coefficient, γ, required for the results in Table 2 and other GDR γ-ray fission studies ranges from 5 to 15 [24, 25, 26, 28, 31, 32, 34, 79, 80], which overlaps the lower end of the range of values reported for the neutron method. Thus, the GDR method would seem to imply less friction than the neutron analyses, leading to shorter time scales for fission. This is not borne out in the reported time scales, which show the opposite trend. Clearly, there are contradictions not only in the time scales reported by these two methods, but also in their behaviors regarding nuclear viscosity.

I.5 Motivations

The current work is aimed at deriving time scales in a more constrained approach by using two separate methods applied to the same experimental data and the same statistical model code. This could quite possibly resolve the discrepancies between these two time scales and friction coefficients (γ's). Simultaneous measurement of both neutrons and γ rays for a number of fissioning systems should limit systematic errors and produce time scales and γ's suitable for more direct comparison. The application of both methods in the same experiment has not been attempted before and could provide new insights into any remaining discrepancies.

CHAPTER II

EXPERIMENTAL TECHNIQUES

This chapter presents a detailed description of the experimental apparatus and the techniques used. The first section deals with the reasoning behind the equipment configuration. This is followed by a discussion of the various characteristics of each component in the equipment. Immediately following this, the experimental setup is presented, including electronics setup, detector placement, and data acquisition. Calibration procedures are discussed next. Finally, a brief summary is given.

II.1 Experimental Background

The experiments involved detection of γ rays, neutrons, and fission fragments and their various correlations. This necessitated the use of a wide variety of facilities and equipment. The beams were provided from the Texas A&M cyclotron. Additional components and support were provided by the Texas A&M Cyclotron Institute, the National Barium Fluoride Array (BFA), the Joint Institute of Nuclear Research (JINR) at Dubna, Russia, and the DEMON Collaboration (for the French *Détecteur Modulaire de Neutrons*, or Modular Neutron Detector) from Belgium and France.

Four reactions were investigated: ^{16}O + ^{208}Pb, ^{4}He + ^{209}Bi, ^{16}O + ^{176}Yb, and ^{4}He + ^{188}Os. The reactions ^{16}O + ^{208}Pb and ^{4}He + ^{209}Bi were chosen to illustrate the effect of angular momenta on the dynamics of fission in systems likely to have enough fission cross-section to give good statistics for GDR γ rays. Also, systems like ^{16}O + ^{208}Pb have been extensively studied in other work, thus allowing comparison

with previous studies. Comparison of the ^{16}O + ^{208}Pb and ^{4}He + ^{209}Bi results could provide insight into the formation time, τ_{form}, for the compound system. It is important to note that the saddle and scission points for these two systems occur at very different positions in deformation space while those points should be nearly coincident for the lighter systems. Comparison of the two types of systems could provide a measure of any fission time delay before the saddle point it reached. The reactions ^{16}O + ^{176}Yb and ^{4}He + ^{188}Os were also chosen because they form the same compound system with different angular momentum. Because the fission cross section is quite low for the latter systems, they were not expected to yield much information on GDR γ rays.

The targets, beams, and other important parameters are summarized in the first part of Table 3. The remainder of the table lists various parameters pertinent to the formation and decay of the compound nucleus. The average sustained beam rate for each reaction was on the order of 1–2 particle nanoamps. Each system was formed with roughly similar excitation energy. The fusion cross sections were taken using the work of Wilke *et al.* [81]. Fission cross sections were taken from fission excitation function studies in the literature [82, 83, 84, 85]. Note the much lower fission cross section for the ^{4}He + ^{188}Os system in particular.

The experiments were carried out in a low background area, away from walls and equipment to avoid neutron scattering and pile-up. The beam line in Cave 3 of the K500 area of the Texas A&M Cyclotron Institute was chosen because of these concerns and to allow easy access to the various detectors and the reaction chamber.

TABLE 3. Summary of important reaction parameters for each experiment.

Reaction	O+Pb	He+Bi	O+Yb	He+Os
Beam	$^{16}O^{3+}$	$^{4}He^{+}$	$^{16}O^{3+}$	$^{4}He^{+}$
Energy	133 MeV	104 MeV	133 MeV	104 MeV
Intensity	1 pnA	1 pnA	2 pnA	1 pnA
Target	^{208}Pb	^{209}Bi	^{176}Yb	^{188}Os
Thickness	600 $\mu g/cm^2$	650 $\mu g/cm^2$	325 $\mu g/cm^2$ (on 40 $\mu g/cm^2$ ^{12}C)	350 $\mu g/cm^2$ (on 50 $\mu g/cm^2$ ^{12}C)
CN	$^{224}Th^*$	$^{213}At^*$	$^{192}Pt^*$	$^{192}Pt^*$
E^*	77.0 MeV	92.7 MeV	100.0 MeV	99.3 MeV
B_c (lab)	82.5 MeV	21.7 MeV	73.6 MeV	20.4 MeV
B_c (CM)	76.5 MeV	21.3 MeV	67.5 MeV	20.0 MeV
E_{CM}	123.5 MeV	102.0 MeV	121.9 MeV	101.8 MeV
v_{CM}	.2851 cm/ns	.1325 cm/ns	.3326 cm/ns	.1470 cm/ns
σ_{fus}	1350 mb	1450 mb	1550 mb	1325 mb
σ_{fis}	1340 mb	630 mb	635 mb	7 mb
θ_{crit}	50.0°	13.4°	41.5°	12.2°
ℓ_{crit}	56 $\hbar$	32 $\hbar$	62 $\hbar$	31 $\hbar$
ℓ_{max}	72 $\hbar$	44 $\hbar$	74 $\hbar$	43 $\hbar$
$\ell_{B_f=0}$	76 $\hbar$	82 $\hbar$	84 $\hbar$	84 $\hbar$

The beam transport system had to provide a nearly parallel beam with a diameter of no more than 5 mm in order to avoid hitting the target frame. Transport downstream of the target to the remote beam dump required negligible intensity loss. A magnetic quadrupole lens was 3 meters upstream of the target and was used to focus the beam into the target. Another magnetic quadrupole 5.5 meters downstream from the target was used to refocus the beam. The beam dump was located in the MDM Spectrometer, some 9 meters downstream from the target. A phosphor viewer near the Faraday cup in the spectrometer was used to view the beam position. Both the BaF_2 arrays and the DEMON neutron counters were used as active background detectors during beam tuning. Background levels were examined by sending the beam through a blank target frame and monitoring the various count rates. A schematic layout of the experiment is shown in Figure 1, and will be described in detail below.

A thin-walled reaction chamber was used to minimize absorption and scattering of neutrons. It was constructed to allow direct mounting of the target ladder and the fission fragment and trigger detectors. Standard view-ports and beam line connections were provided. The chamber was relatively small to allow close placement of the BaF_2 pods. It was specially designed and constructed by the Dubna group, which also provided the ^{188}Os target. The remaining targets were produced at Texas A&M.

Parallel plate avalanche counters (PPAC's) were used to detect fission fragments. These were used because they are fast, resistant to radiation damage, and can be constructed with large volumes. They were placed at a close geometry to obtain high geometrical efficiency. The PPAC's were x-y position sensitive to allow

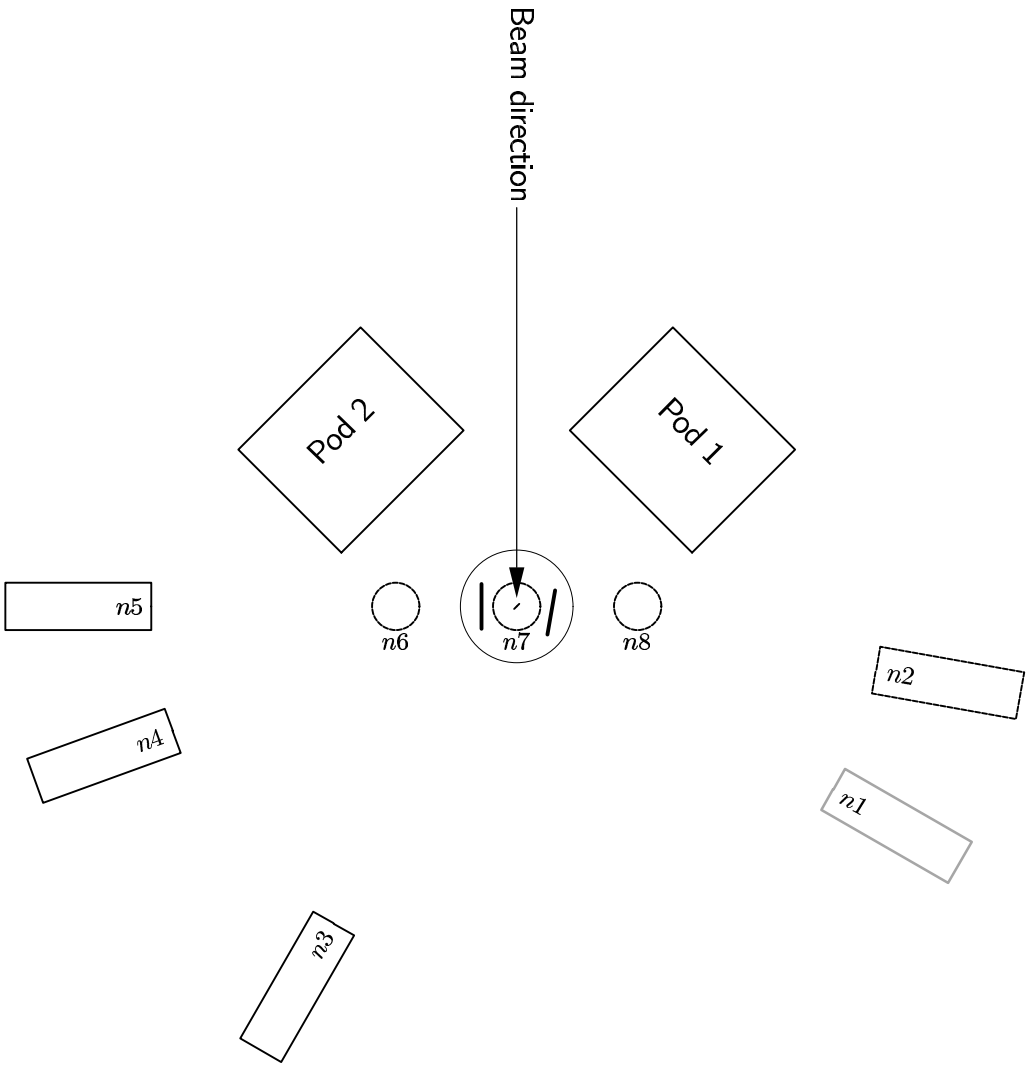

FIG. 1. Schematic of the experimental. The DEMON detectors are indicated by $n1$–$n8$. The detector $n1$ is below the reaction plane, while $n2$ and $n6$–$n8$ are above. The two pods of BaF_2 detectors are also shown. The two large PPAC's are indicated by the thicker straight lines between $n6$, $n7$, and $n8$. The PPAC's are at their locations for the $^{16}O + {}^{208}Pb$ experiment, 90° and 80°.

reconstruction of the fragment energies and masses. A total of four PPAC's were constructed at Texas A&M, together with two smaller PPAC's without position sensitivity for use as start detectors. Only half of these were used during the experiments.

Measurement of the γ-ray energy spectra required a high geometric efficiency while maintaining a reasonable distance from the target to allow for time-of-flight separation of neutrons. The BFA was separated into two rectangular "pods" of 72 crystals (9×8) and placed at backward angles to minimize the neutron background. These detectors could operate at high count rates and gave good time resolution. Since acquisition times were likely to be long, it was important that they have good electronic stability. The whole of the National Barium Fluoride Array and its support electronics and acquisition system were required for these experiments.

The DEMON modules [86] were used for neutron detection and were based on the liquid scintillator NE213. These detectors were relatively efficient and gave good time resolution. Eight detectors from the DEMON Array were used. These were placed at a various angles about the target chamber to gain insight into the angular distribution of ν_{pre} and ν_{post}.

The remainder of this chapter will present more detailed accounts of the apparatus used, the procedure including the placement of detectors, electronics, trigger conditions and data acquisition, and the calibrations.

II.2 Apparatus

This section presents a description of the experimental apparatus. First, the reaction chamber and its construction will be discussed. Following this, the PPAC's, the BaF_2 detectors, and then the DEMON neutron counters will each be examined in detail.

II.2.1 Reaction Chamber

The reaction chamber was designed and constructed in Dubna, Russia specifically for these experiments. Figure 2 shows detailed side and front views. The chamber is a prolate spheroid, 39.3 cm in diameter with a 48.1 cm long axis. It is constructed of thin-walled (2.5 mm) aluminum hemispheres to avoid excessive neutron absorption. The hemispheres are attached to a 9.65 cm wide central support ring of stainless steel. The hemispheres consist of two halves of a sphere with an inner diameter of 38.4 cm. The central support ring provides 24 BNC feed-through connectors, a 4 cm lucite view-port, beam line fittings on either side, and support for a detector mounting table. There is also a connection for an existing electronically-controlled target ladder assembly, capable of being controlled remotely. This assembly accommodates five standard-sized targets. The two aluminum hemispheres are held in position on either side of the ring with metal restraining straps to form a vacuum seal using Viton O-rings.

II.2.2 Parallel Plate Avalanche Counters

Parallel plate avalanche counters (PPAC's) were chosen to detect the fission fragments for a number of reasons. They are relatively inexpensive, easy to fabricate

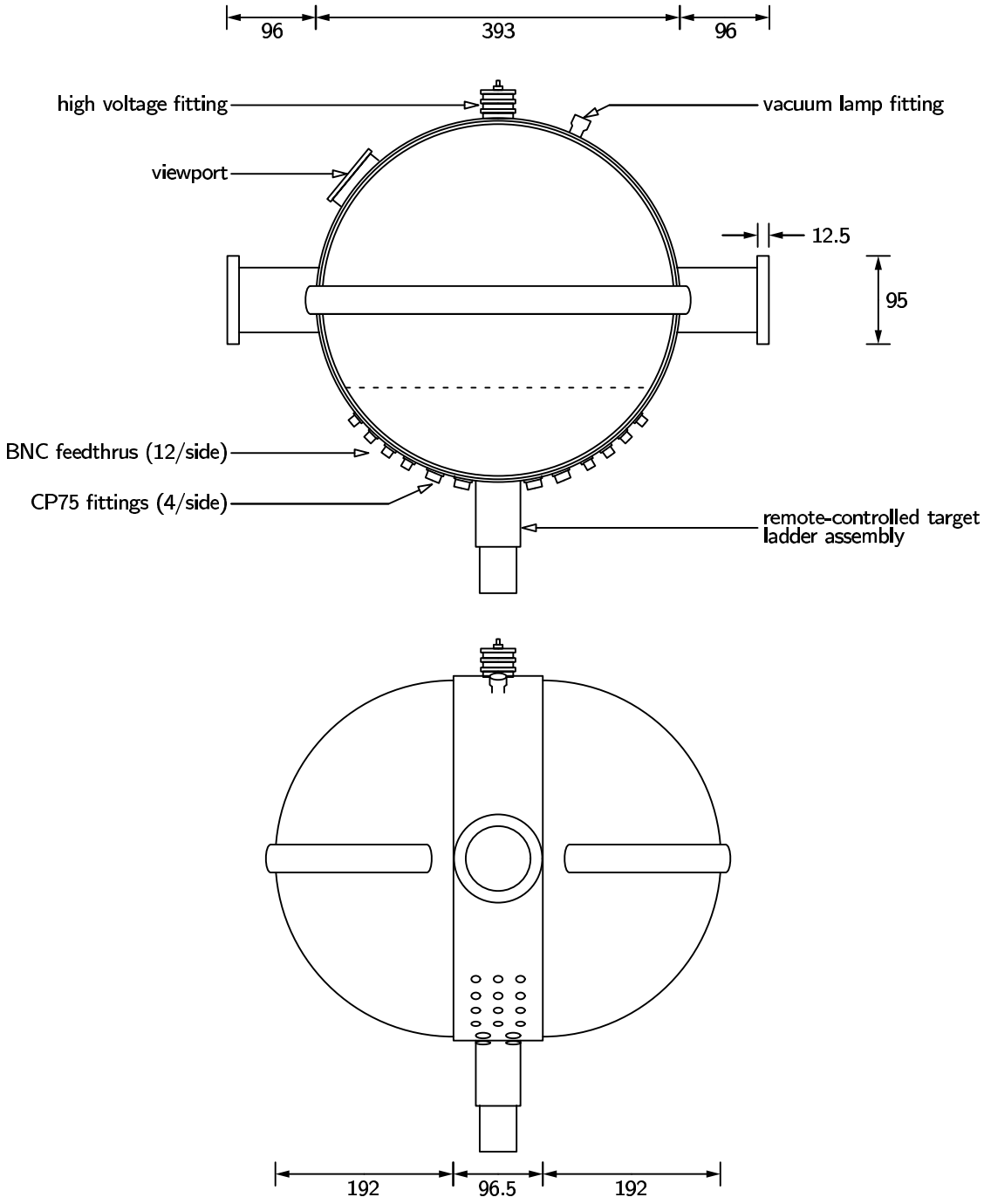

FIG. 2. Schematic of the reaction chamber. Top depicts the side view of the chamber. Dotted line indicates the level of the detector support plate inside the chamber. Bottom shows the view from the cyclotron. All measurements in mm.

in a variety of geometries, are resistant to radiation damage, can have quite large solid angles, and are reusable. In addition to these conveniences, properly designed PPAC's exhibit excellent time resolution and can be made position sensitive. The latter characteristics are critical in the event-by-event reconstruction of the fission fragment mass distributions.

The rise time for the center foil signal is generally very fast and is largely responsible for the excellent time resolution of the detectors (≈150 ps). This time resolution corresponds to a position sensitivity which is usually on the order of the spacing between the wires [27], typically 1 mm. Because of these characteristics, PPAC's have proven useful in previous works investigating fission time scales [14, 27, 34]. A good description of PPAC design and characteristics is given by Mazur and Ribrag [87]. The detectors described therein are similar to those used in the current work [88].

The PPAC's used here consisted of two planes of thin, parallel wires running orthogonal to each other and parallel to a thin, common center foil plane. The foil plane was supplied with negative bias (≈ -0.7 kV) and acted as the common cathode for the anode wire planes. These components were contained in a low pressure of *n*-pentane. The actual experimental operating characteristics are summarized in Table 4.

Detection of energetic charged particles in a PPAC is a multi-step process. Electrons are produced as a fission fragment ionizes this gas and interacts with the center foil. These electrons are then accelerated in the strong electric field, producing

TABLE 4. Operating characteristics for the PPAC's.

Detector	Bias (volts)	Pentane Pressure (torr)	Flow Rate (ml/min)
Start	-590 to -610	5.2	20
PPAC1	-680	"	"
PPAC2	-660	"	"

an avalanche of secondary electrons. The largest amplification occurs near the anode wires [87]. The nearest wire then collects the most electrons, producing a negative electronic signal. This signal is then carried through a delay proportional to the wire's location. By measuring the time difference between the prompt signal from the center foil (cathode) and the delayed signal from the wires (anode), one obtains the relative location of the fission fragment impact in one dimension. Since there are two planes of wires running orthogonal to each other, the detector produces signals in both the x and y coordinates.

The detectors were constructed of several layers of 3 mm thick G-10 PC board. Each detector was made vacuum-tight with silicone caulk, which also functioned as a structural bond between the layers. Fittings were provided at the rear of the detector for gas entry and exit. Connections for the center-foil bias supply and signals were made using LEMO fittings. A second type of PPAC was used in the experiments to detect fission fragments. This was a small (4 cm^2 active area) PPAC start detector. Two larger position-sensitive PPAC's (231 cm^2 active area) were used to detect the fission fragments and define the reaction plane. The start detector

PPAC had entrance and exit windows of 2 μm mylar. This counter was designed to minimize the energy degradation of the fission fragments as much as possible. Two foil planes were fashioned by vacuum evaporation of gold onto mylar to a thickness of 40 μg/cm^2 on each side. The same type of center foil was used for each detector. A major difference between the large and small detectors was that the start PPAC was a transmission counter while the large PPAC's were not. The start detectors were also not position sensitive.

In the large PPAC's there were two planes of 50 μm diameter Be-Cu wires mounted on a 1.5 mm thick G-10 support frame. The wire spacing was one millimeter, providing 152 wires for each plane. The wires were stretched and soldered onto the support. Figure 3 shows a schematic of the alignment of the wire planes on either side of the center foil cathode plane. These wire planes were assembled in the PPAC housing such that the wires of one ran perpendicular to the other when seen from the target. Each wire plane was made contiguous via a 210 ns delay loop of copper wire connecting each wire to its neighbors. This provided a delay of 13.5 ns from wire to wire, which gave sufficient time-separation of the signals for the required position sensitivity. The wire planes were located 3.00 $\pm$ 0.05 mm from the center foil. A detailed cross section of a large detector is shown in Figure 4. A front view (seen from the target position) is shown in Figure 5. Note the presence of two thick calibration wires in the x-direction, allowing for positional self-calibration. These wires were placed 50.7 mm and 50.5 mm apart for the PPAC's #1 and #2, respectively. The y-direction was calibrated using the physical limits of the active area. Each PPAC

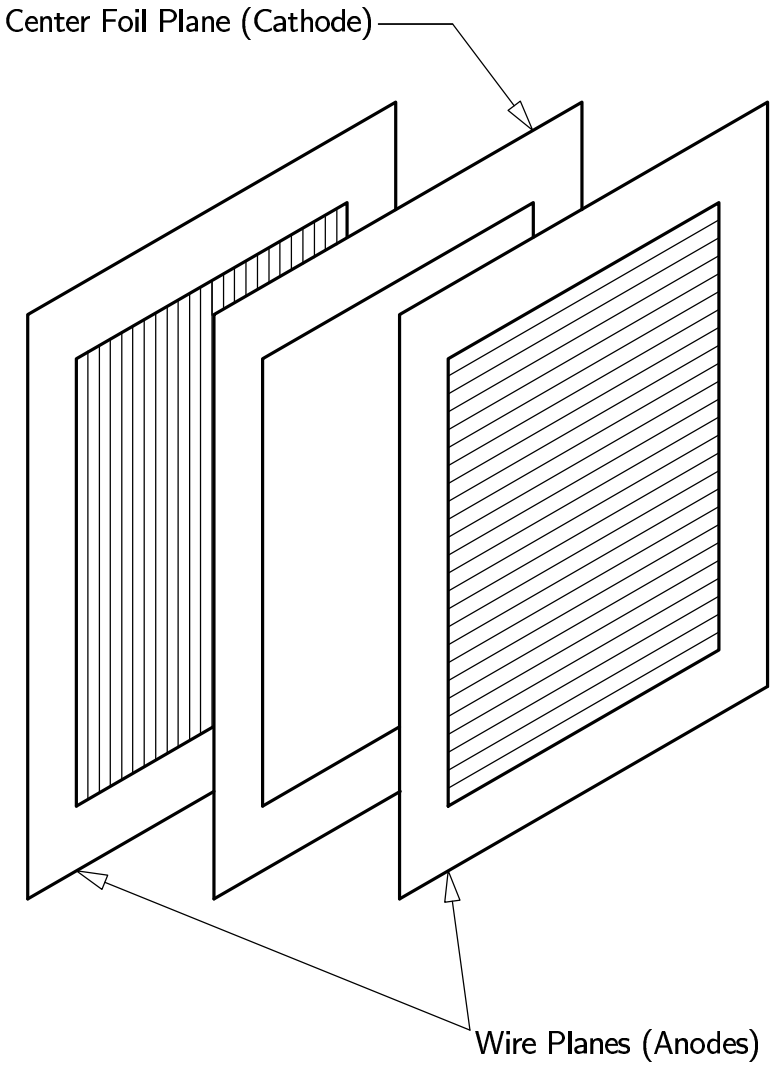

FIG. 3. Schematic of the wire planes and center foil of the PPAC's. Note that the wire planes are perpendicular to each other, allowing for the x- and y-position sensitivity. The distance between the planes is expanded for ease of viewing.

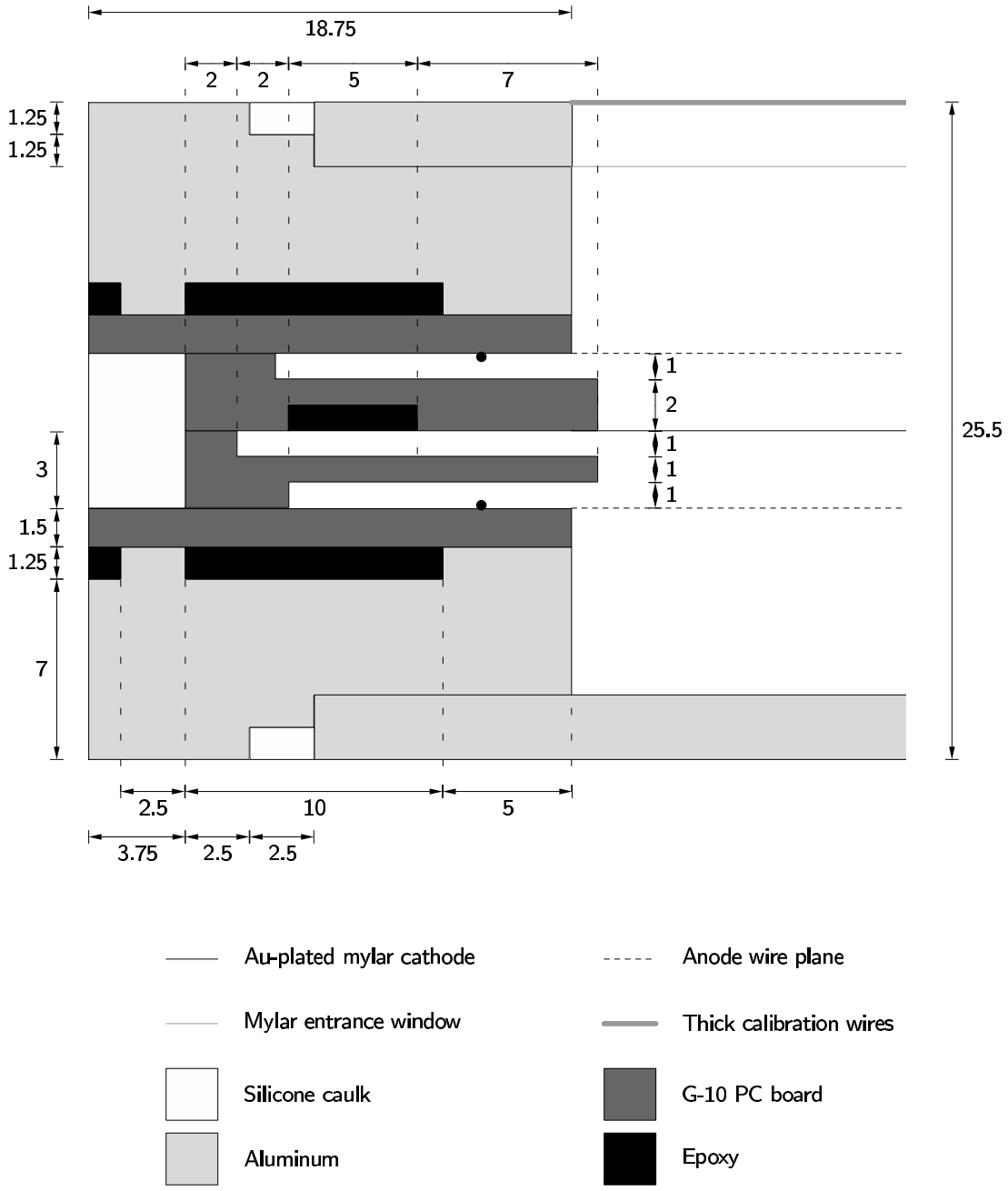

FIG. 4. Cut-away view of part of one PPAC. The center foil, wire planes, entrance window, and calibration wire planes all extend to the right of the shaded part of the figure. The two black dots near the center of the figure indicate solder beads in order to show how the soldering points are shielded from view of the center foil, minimizing sparking in the detector. All dimensions are in millimeters.

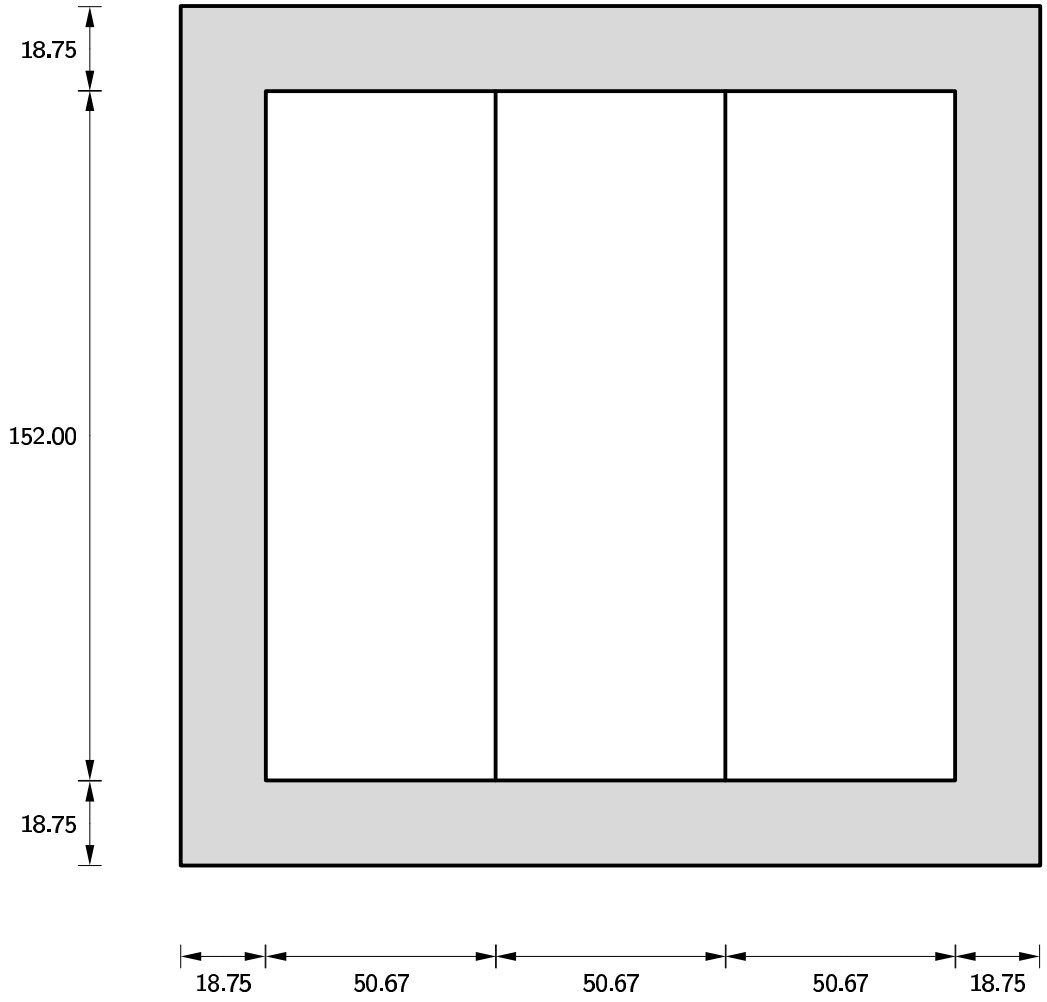

FIG. 5. Front view of one PPAC. Most of the detector is active area, with little wasted space. The two calibration wires are also shown. All dimensions are in millimeters.

provided four outputs; a timing signal from the center foil (start), stops for both wire planes and an energy output for the center-foil. The latter was not used in the analysis, but provided an on-line indicator of the performance of the PPAC's.

II.2.3 Barium Fluoride Detectors

Myriad detector types are available for γ-ray detection ranging from very high resolution semi-conductor devices, such as Si(Li) and Ge(Li), to a wide variety of low energy resolution scintillators, such as NaI(Tl). Though quite expensive, large arrays of the former type of device have been constructed [89, 90]. These have mostly been used for nuclear structure studies. For GDR-fission studies, one does not need such high-resolution detectors; scintillation devices are generally employed. Initially, NaI(Tl) detectors were generally employed. However, there are great advantages to using BaF_2 as a GDR γ-ray detector. Unlike NaI(Tl), BaF_2 is non-hygroscopic. The radiation lengths of the two detectors are comparable. While the energy resolution of BaF_2-based scintillators is somewhat poorer than NaI(Tl), they have proven to have excellent time characteristics. The BaF_2 detectors provide a fast component that differs from the slow component in its decay properties, depending upon the type of particle detected. This was first noted in 1982, by Laval and co-workers [91]. A few years later, it was shown that the yield of the components depended on the incident particle [92]. This allows pulse-shape discrimination (PSD) between neutrons, γ rays, and other species.

Energy resolution for the BaF_2 crystals obtained with ^{137}Cs (0.661 MeV) is approximately 35% and 12.5% for the fast and total components, respectively [93].

TABLE 5. Response characteristics for both the fast and the slow components in BaF_2.

	Fast Component	Slow Component
peak wavelength	220 nm	310 nm
rise time	100 ps	n/a
primary decay const	600 ps	430 ns
secondary decay const	790 ps	620 ns

The rise times of BaF_2 detectors obtained by Laval *et al.* are shown in Table 5 [91]. The energy response of a BaF_2 detector is governed not only by its intrinsic properties but also by its geometry, which determines the fraction of the electromagnetic shower produced by an incident particle that is actually contained in the detector volume. Losses can occur out the sides of the detector and to the rear. With long detectors, losses to the rear can be minimized. In these experiments, losses out the sides were mainly seen by the neighboring crystals, which acted as transverse loss detectors for the crystal they surrounded. Section III.2.1 discusses simulation of these losses and the effects of utilizing the surrounding crystals to reconstruct the shower.

Each individual detector is made up of a sealed crystal of BaF_2 optically coupled to an assembly consisting of a base and a photomultiplier tube (either Hamamatsu R2059 or Philips XP2020Q) with fused silica windows. The photomultiplier tubes provided both dynode and anode outputs. The crystals are 20 cm long with a hexagonal cross section which is 6.5 cm face to face. The final 2.5 cm is ground

into a cylindrical shape to allow optical coupling to the photomultiplier and magnetic shielding with μ-metal. The latter is necessary to minimize electronic crosstalk between detectors and reduce the influence of stray magnetic fields from the focusing magnets. All surfaces are polished, covered by light reflector, and wrapped in black tape.

Finally, the data acquisition system consisted of a DEC Alpha 3000 workstation running Digital Unix and utilizing the Oak Ridge Physics Analysis System (ORPAS). A wide variety of custom software, such as photomultiplier bias control, detector response gain matching, and pedestal subtraction, was provided to control various aspects of the BFA [94]. ORPAS was also used to read out signals from all the other detectors via CAMAC.

II.2.4 Neutron Scintillators

The DEMON array [86], consists of $\approx$100 large volume liquid scintillator (available as NE213 or Bicron BC501A) neutron detectors. The scintillator exhibits many desirable detection properties, including excellent timing, good PSD, the ability to be used in large detectors, and a relatively high efficiency [95]. The PSD characteristics are long established and have been well-studied [96, 97, 98], and in fact NE213 has become quite standard for portable neutron detection.

Eight units from the DEMON array were supplied for this experiment, along with some special electronics. Stands and mounting brackets were constructed in-house. Each detector consists of a 20 cm long $\times$ 16 cm diameter cylindrical aluminum scintillator reservoir optically coupled to a 12.7 cm long $\times$ 13 cm diameter

photomultiplier, Philips model XP4512B [99]. The aluminum reservoir has a 6.35 mm thick front entrance and a 21.5 mm thick side wall. The rear window is 10 mm thick glass. The detector contains 4 liters of NE213 scintillator and is surrounded by μ-metal shielding and contained in a thin-walled steel casing with an overall length of 50 cm. The front face was covered by a 5 mm thick lead plate designed to lower the counting rate of low-energy photons thereby improving the separation of low-energy neutrons and γ rays [100].

The photomultipliers have a gain of $\approx 5.0 \times 10^6$. The standard anode pulse rise time is 2.1 ns, the intrinsic photomultiplier pulse duration at half maximum is 3 ns, and the signal transit time is 49 ± 1.3 ns for full cathode illumination [100]. The DEMON detectors have been well studied over the years, providing very good information on the effects of the photocoupling [101], the size of the detectors, their associated electronics [99, 102], and neutron detection efficiency [100].

Like the BaF_2 detectors, the NE213 scintillator has both fast and slow components, thus allowing for pulse shape discrimination. This enables the separation of neutrons from γ rays in most cases. The exception is due to reactions such as $^{12}C(n,n'\gamma)^{12}C$. This can produce a γ-ray-like signal. However, this process can generally be accounted for in detector simulation codes, such as MENATE [103, 104]. Experimentally, many γ rays from such reactions can be identified by time-of-flight.

Two charge-to-digital converters (QDC's) are used to integrate the different portions of the photomultiplier's response. Time gates were set around the whole pulse to obtain a total component signal and around the slow portion. The total gate usually started 5 ns before the beginning of the pulse and continued for 220 ns.

The slow gate was set 50 ns later and continued for 170 ns. Both gates closed simultaneously.

II.3 Setup

A schematic top view of the overall experimental layout was already given in Figure 1. This figure shows the two position-sensitive parallel plate avalanche counters (PPAC's) centered at 90° and either 60° (for the 104 MeV ^{4}He runs) or 80° (for the 133 MeV ^{16}O runs). The time-of-flight of the fission fragments was determined using the start detector. This was placed very close (≈2 cm) to the target and covered the same solid angle as the larger PPAC (#1), which was directly behind it. Both the large PPAC's functioned as stop detectors.

The BFA was divided into two pods with 72 BaF_2 crystals each, arranged in a 9×8 fashion to give an overall rectangular shape with dimensions 55.25 cm wide by 50.03 cm high. Triangular vinyl support spacers were used to help support the crystals to reduce shearing stress on the detectors. Figure 6 shows a schematic of the BaF_2 layout and its housing. The centers of the pods were the same height as the center of the target. The pods were placed on each side of the beam pipe, centered on 135° at a distance of 55 cm and facing the target. The backwards angles were used to reduce neutron background which interferes with detection of γ rays.

The neutron detectors were placed around the target at a nominal distances of 1.2 meters each. Detectors were mounted in-plane at angles of (θ=30°; ϕ=180°), (θ=70°; ϕ=180°), and (θ=90°; ϕ=180°) and out-of-plane at angles of (θ=-20°; ϕ=60°), (θ=20°; ϕ=80°), (θ=70°; ϕ=90°), (θ=90; ϕ=90°) and (θ=110°; ϕ=90°), taking the

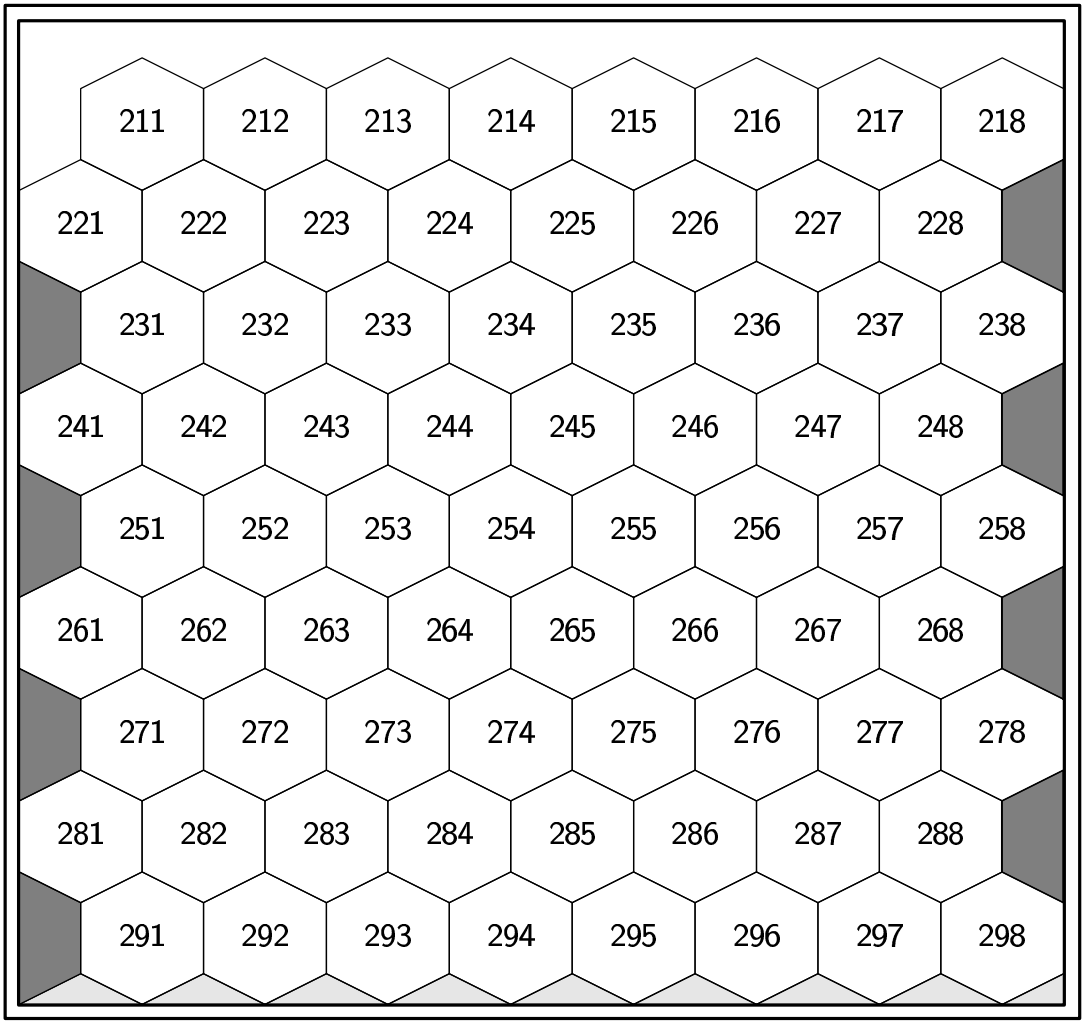

FIG. 6. Front view of BaF_2 Pod 2, including its aluminum housing. The housing consisted of 0.75 cm thick aluminum with inner dimensions of 55.4 cm wide by 52.0 cm high. The lightly shaded regions indicate the vinyl support spacers. The darkly shaded regions represent the plastic side support spacers. The numbering scheme shown for the individual crystals is such that the first digit is the pod number, the second is the row number, and the third is the column number.

TABLE 6. Summary of detector placement in spherical coordinates. The solid angles for each of the detectors are also indicated. For the solid angles for the BaF_2 pods, the values in parentheses are the solid angles for the sum of the "core" crystals (see Section III.2 for details).

Detector	θ	ϕ	R (cm)	Solid Angle (% of 4π)
N1	-20°	60°	120	0.11
N2	20°	80°	117	0.12
N3	30°	180°	159	0.06
N4	70°	180°	122	0.11
N5	90°	180°	124	0.10
N6	90°	110°	122	0.11
N7	90°	90°	114	0.12
N8	90°	70°	123	0.11
PPAC1	180°	90°	12.30	12.15
PPAC2	0°	60°/80°	11.86	13.07
BaF_2 Pod 1	135°	0°	55	6.62 (4.41)
BaF_2 Pod 2	135°	180°	55	6.62 (4.41)

direction of the beam to be (ϕ=0). Figure 1 shows the placement of the various detectors about the target and gives a general sense of their relative locations. Locations and solid angle coverage are summarized in Table 6. The placement of the various detectors was chosen to optimize the detection of neutrons emitted both parallel and perpendicular to the velocity vectors of the fission fragments.

II.3.1 Electronics

The BFA used dedicated electronics and acquisition systems. The remaining electronics for the DEMON neutron scintillators, the PPAC's, and the trigger logic from the DEMON array came from the in-house pool.

For the BFA, the electronics are quite complicated due to the large number of parameters as well as the many different types of modules involved. Only the salient points will be covered here. The energy signals from the BFA were taken from the anode outputs and sent through custom delays and splitters to two sets of fast encoding readout charge sensitive ADC's (FERA). One of these integrated the charge from the short gates (fast signal) and one for the long gates (slow signal). The dynode signal was attenuated, split using a fanout, and fed to two leading edge discriminators which generated the various logic, timing, and trigger signals for the BFA. The attenuation was performed by approximately matching the amplitudes from the fast components of all the crystals. This helped prevent crystals with abnormally high fast light from overwhelming the other detectors in the trigger. The discriminator outputs generated the short and long gates, timing, and the high- and low-γ triggers. The gates were constructed using the logic signal from LeCroy 4413 leading edge discriminators with a nominal threshold of 100 keV. The signals were delayed by 250 ns and refreshed with another discriminator. The signals were logically AND'ed with the "MG.Live" signal (a trigger NAND'ed with the computer busy signal). The long and slow gates were set at 1.5 μs for the slow component and 50 ns for the fast component and delayed by 500 ns. Timing signals for the BFA were constructed from the LeCroy 4413 logic signal to start the Fastbus time-to-digital converters (TDC's) after a delay of 500 ns.

Two types of triggers were formed to read out the BFA. The low-γ trigger was produced from the logical OR of the LeCroy 4413 discriminators from all the BaF_2 detectors. These discriminators were set at their minimum thresholds, 30 mV

(approximately 100–200 keV). This OR was delayed by 250 ns, and refreshed by another discriminator, thus producing the low-γ trigger. The high-γ trigger was formed by first sending the signal through a linear summer for the neighboring detectors and then sending through a different set of LeCroy 4413 discriminators. A logical OR of the signals from the other detectors was formed which was then delayed by 200 ns and refreshed to provide the high-γ trigger.

The motivation for the two triggers is multi-fold. First, either one of the triggers could be used to self-trigger the array. This is useful in calibrating the array with γ-ray sources of different energies. Second, the two triggers are very useful in beam tuning and in monitoring the general performance of the array. Third, the signals from individual crystals forming the low-γ trigger are used to determine which signals are read out and sent to the data acquisition system. This obviously saves computer time and increases the potential data rate. Finally, the high-γ trigger can be incorporated into the overall trigger for the experiment. Normally, this would involve setting the discriminators at several MeV to select high energy photons. However, as discussed below, this capability was not needed in the present work.

The neutron scintillators and PPAC's were read out using CAMAC electronics in a separate crate. In principle, this amounted to simple addition to the existing BFA framework. In practice, it added considerable complexity to the overall experiment. While the Fastbus produced computer-ready information on a time scale of $\approx$10 μs, CAMAC requires about 100 μs to convert. This intrinsic incompatibility lead to considerable complications in matching the timing from the detector subsystems.

The electronics for the neutron scintillators and the BFA were similar since both are scintillation detectors relying on PSD to differentiate particles and photons. Energy signals were taken from the anode of the phototube and fanned out to produce logic gates. These were delayed by 200 ns and sent into custom QDC's provided by the DEMON group.

In the BFA case, separate gates were set around the fast and slow components. For the neutron detectors, total gates were set around the entire pulse and slow gates were set around the slow component. The former signals required an additional $\times 0.3$ attenuation before going into the QDC. Both gates were formed analogously to the BFA gates: a discriminator set with a threshold just above noise. The output was delayed by 250 ns and fed to another discriminator. The slow gate was then formed after an additional 50 ns delay using a gate-and-delay generator. The latter produced a 170 ns wide pulse delayed by 200 ns. The total gate was also set to begin after a 200 ns delay but continued for 220 ns. Timing information was constructed using additional discriminator outputs. These were delayed by 360 ns, and then sent into CAMAC TDC's.

The PPAC's provided the overall trigger for the experiment. Energy signals from the PPAC center foils were sent through custom pre-amplifiers (PMA's), delayed by 250 ns, and sent to CAMAC ADC's. The PMA's also produced fast timing signals. These were further amplified and sent to CFD's with thresholds set just above noise. The logical outputs were then delayed by 450 ns before going into CAMAC TDC's. The time signals in the large position-sensitive PPAC's were used for both time-of-flight (TOF) and for the x- and y-position determination.

Start signals for all TDC's were determined by a master PPAC trigger, which was formed if at least one fission fragment was detected. This trigger was generated from an OR of either of the position-sensitive PPAC's. This required matching the timing of the PPAC's to that of the other detector subsystems. This was nontrivial and took several days of in-beam work. While the bulk of the data were taken with a PPAC trigger, a "singles" mode was also employed in the experiment. In this case, acquisition was triggered on the detection of at least one above-threshold γ ray in the BFA. Though useful in monitoring the performance of the BFA, these results did not provide much quantitative information and thus these data are not addressed in this work.

II.3.2 Data Acquisition System

As mentioned above, all the data were taken using a custom system developed at ORNL for the BFA. Data were collected for 465 parameters. The data were acquired with a Dec Model 3000 workstation over ethernet using VME interfaced to CAMAC, FERA and Fastbus. The acquisition rate varied from 250 to 1500 Hz. The lower rates were associated with lower-mass compound nuclei. The dead time was at most 25%, but more typically around 5%. These relatively low dead-times were obtained by triggering the system on fission fragments. For this reason, it was not necessary to incorporate the high-γ trigger into the master gate. This simplified the timing and subsequent analysis. The only drawback was the vast quantity of accumulated data (almost 100 GB).

The acquisition suite ORPAS (running under Digital Unix) provided subroutines to poll and correlate the data from each of the CAMAC, FERA, and Fastbus subsystems over VME. Each possible signal was given a unique index reflecting its exact location in the electronics. The index number, i, was given by

$$i = 2048c + 64s + n. \tag{21}$$

where c is the crate number, s is the slot number, and n is the channel number associated with the particular parameter being recorded.

These data were then written to double-density 8mm tape by first listing the index number and the corresponding data using 4 byte words for each parameter. Zero skip suppression was used to obtain the smallest possible data files. Due to the large number of parameters and the large number of expected zeroes for each event, this method was much more desirable than either listing the value of each index in order or bit-mapping the data. After writing each index-data pair, the end of an event was indicated by the integer value "-1" repeated twice (FFFF FFFF in hexadecimal). This simple and straightforward method of recording the data proved to be quite helpful in the subsequent analysis. As a precautionary measure, data files were automatically closed out after every 80 MB of data were recorded and a new file was started. Thus, each run actually would consist of any number of data files.

As noted above, the BFA was read out with zero-suppression, meaning that parameters for a given crystal were only recorded if they had non-zero values for the energy in the fast component. For those BaF_2 crystals, the fast energy signal, the slow energy signal, and the TOF signal with respect to the event trigger were

written on tape. Unfortunately, zero-suppression was only possible for the BFA data since only their electronics allowed for this option. Hence, all PPAC and all DEMON parameters were taken for each event. The PPAC parameters consisted of four time differences corresponding to the two sets of x- and y-positions, two times for the TOF between the start detector and the stop detectors, two times for the difference between the PPAC start and the BFA stops, and one time for the Δt between the stops of the large PPAC's. The DEMON parameters each consisted of a fast energy signal, a total energy signal, and a TOF signal measured with respect to the trigger.

II.3.3 In-Beam Tuning

During the experiment, the quality of the data were monitored in a number of ways. Using the PPAC's, it was possible to examine the quality of the fission data with two-dimensional plots of the position data. Figure 7 shows the x versus y data for PPAC #1 during an $^{16}O + {}^{208}Pb$ run. Log contours are used with a power of 3 between each contour. The highest number of counts are in the center-most contour, with decreasing counts moving away from the center. Not only are the calibration wires visible, but also other important features. Note the relatively higher count-rate at the high-x channels. This confirms the placement and orientation of that detector since PPAC #1 had its high-x end at more forward angles. Also, the two dips near the top of the spectrum are due to unavoidable obstruction by the gas lines to the start detector further characterizing PPAC #1. Similarly, in Figure 8 one can distinguish the location of the calibration wires, as well as regions of the highest counting rate. The same contours are used and again the center-most contour marks

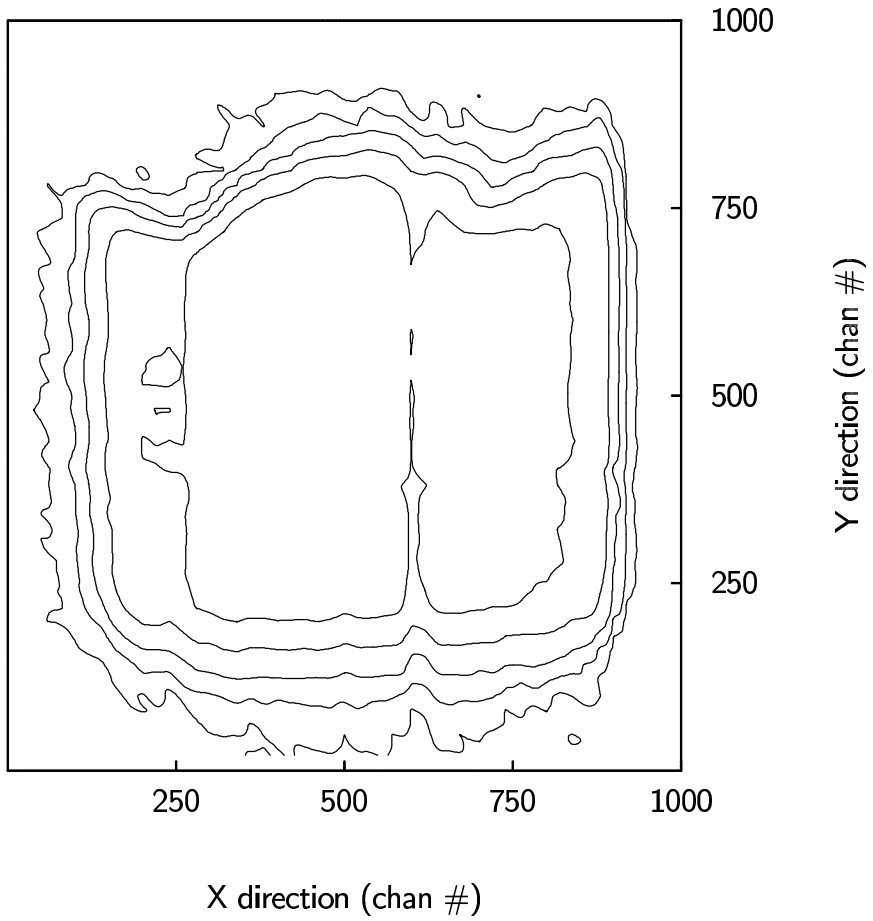

FIG. 7. X versus Y plot for PPAC #1 after PPAC analysis. The calibration wires for the x-direction are clearly visible near channels 260 and 670.

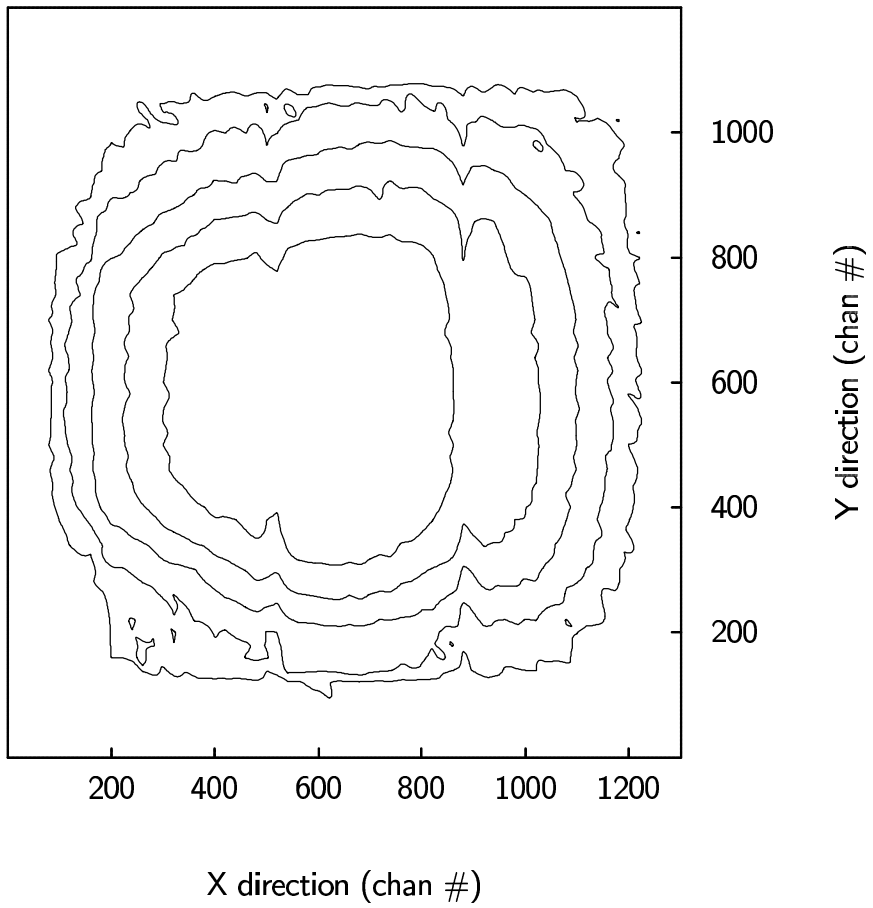

FIG. 8. X versus Y plot for PPAC 2 after PPAC analysis. The calibration wires for the x-direction are also visible here, but at channels 500 and 875.

the highest number of counts. Other two-dimensional plots used included x-x and y-y correlations, and time versus position. Additionally, the timing spectra from all detectors were monitored for anomalies, as were the energy spectra from the BaF_2 detectors and the DEMON scintillators. This was very useful since one or more BaF_2 crystals would "run wild" due to drifts in the discriminator levels, sparking in the PMT bases, or poor shielding in the PMT. Over the course of the experiments, only a few percent of the detectors were not functioning correctly. These were accounted for in the analysis.

II.4 Calibrations

Each of the detector subsystems was calibrated either during and/or at the end of the experiment. Some parameters could be self-calibrated. The various calibrations and their results are described below, beginning with the PPAC's, then the BaF_2 arrays, and finally the DEMON detectors.

II.4.1 PPAC's

The PPAC's required very accurate time calibrations since this quantity was used to extract both the velocity (via center foil timing) and the angle (via x- and y-position timing) of the fission fragments. These quantities are needed to reconstruct the masses and kinetic energies of the fragments. Each TDC channel was calibrated separately with an Ortec Model 462 time calibrator using pulses at 10 ns, over a range of 320 ns. The time response of each channel was found to be linear and reproduceable. The physical position was self-calibrated. In the y-direction, the actual edges of the active area of the detector gave accurate position calibration. In the x-direction, two

vertical copper wires were placed at known positions. The effects of these wires can readily be seen in the x-position spectra as two vertical lines of lower-count regions. No energy calibration was performed for the center foil since it was only used to monitor the detector performance.

II.4.2 BaF_2 Detectors

The total energy signals from the BaF_2 crystals were calibrated using a ≈ 0.1 Ci americium-beryllium (AmBe) source, which emits both fast neutrons and 4.4389 MeV photons. The source was an encapsulated mixture of finely ground americium and beryllium. The characteristic 4.4389 MeV γ ray is produced by the reaction $^{9}Be(\alpha,n\gamma)^{12}C$ [105], giving approximately one γ ray every 10^6 americium alpha decays [106]. Fast neutrons are produced with energies up to 11 MeV [107]. The neutrons were moderated with a 15 cm thick polyethylene block to minimize the neutron background in the BaF_2 detectors. The moderators also provided another γ ray via the reaction n(p,γ)d. This γ ray occurs at 2.224 MeV, giving a second energy calibration point. The first escape peak of the 4.4389 MeV γ ray provided a third calibration peak. Table 7 gives the characteristics of these γ rays together with those of other sources used in the calibrations of the DEMON neutron counters.

In calibrating the BaF_2 detectors, each pod was treated separately. A sample raw calibration spectrum obtained from one of the crystals is shown in Figure 9. The calibration data were taken at the same magnet settings used during the experiments to ensure that the photomultipliers of the BaF_2 crystals experienced the same magnetic fields. Pedestals acting as zero offsets were determined from data taken in-beam.

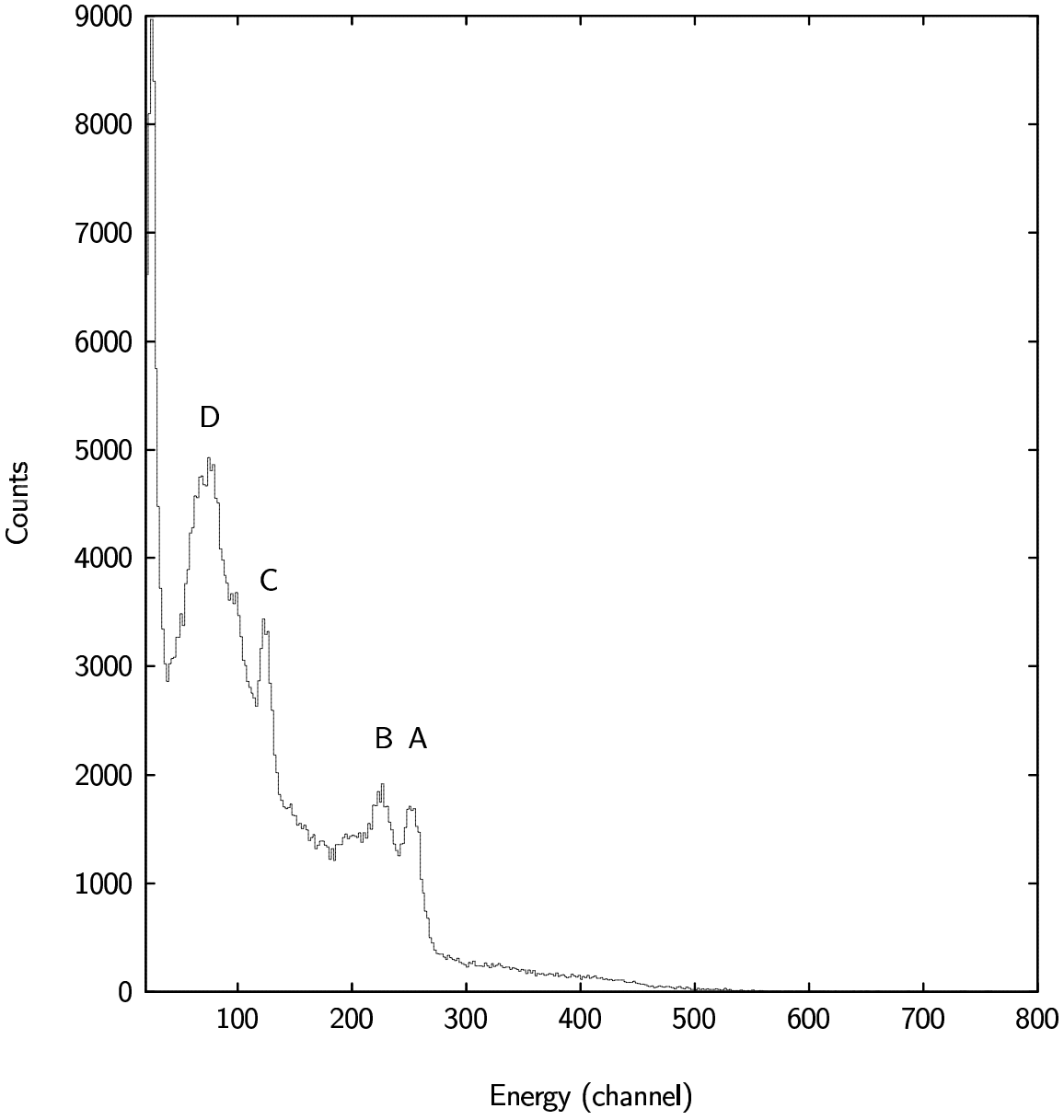

FIG. 9. Raw AmBe calibration for a typical BaF_2 crystal.

TABLE 7. Gamma calibration sources used in these experiments and their associated energy peaks. The source, type of γ ray, and corresponding energy are listed.

Source	Type	Energy (MeV)
AmBe	^{9}Be(α,nγ)^{12}C	4.4389
	1^{st} escape peak	3.9279
	n(p,γ)d	2.224
^{60}Co	*internal decay*	1.3325
	internal decay	1.1732
^{137}Cs	*internal decay*	0.6616

The positions of the pedestals were essentially constant throughout the experiment and during the calibrations. This was further verified by regression analysis of the calibration runs. A sample regression analysis for several crystals is shown in Figure 10. The energy response of the BaF_2 crystals was expected to be quite linear, which was borne out by the calibration analysis. Thus the extrapolation to the energy region of interest (10–15 MeV) seems reliable.

The timing signals from the BaF_2's were self-calibrated using the known frequency of the beam bursts. A sample TDC spectrum from a typical BaF_2 crystal is shown in Figure 11. Table 8 shows the slopes, intercepts, and correlation coefficient for each of the detectors shown in Figure 10 for the entire ^{16}O + ^{208}Pb experiment. The large bumps between 100 and 150 ns correspond to PPAC-γ coincidences. The strongest sharp peak is largely due to real PPAC-γ events and corresponds to the real start time, t_0. The other sharp peaks are due to random coincidences. The time gate used to separate the real γ rays from the neutrons and other background signals

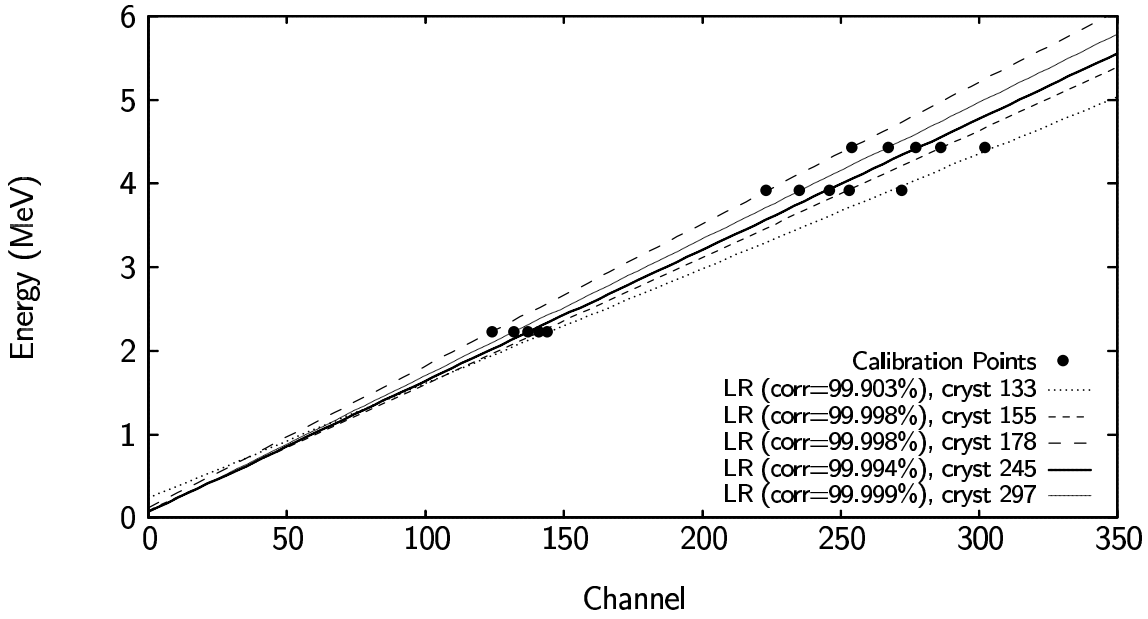

FIG. 10. Graphical results of a linear regression analysis on the AmBe calibrations of several BaF_2 detectors. Detectors from both pods are shown. A random sample of crystals was chosen. Crystal 133 provides an example of the worst linearity seen in the whole BaF_2 array.

TABLE 8. Tabulation of the calibration coefficients for several BaF_2 crystals. The detectors listed are the same as shown in Figure 10.

Crystal	Slope (MeV/channel)	Intercept (MeV)	Correlation (%)
133	1.3739×10^{-2}	23.6080×10^{-2}	99.903
155	1.5184×10^{-2}	8.2693×10^{-2}	99.998
178	1.6995×10^{-2}	11.9572×10^{-2}	99.998
245	1.5693×10^{-2}	7.1896×10^{-2}	99.994
297	1.6359×10^{-2}	6.7195×10^{-2}	99.999

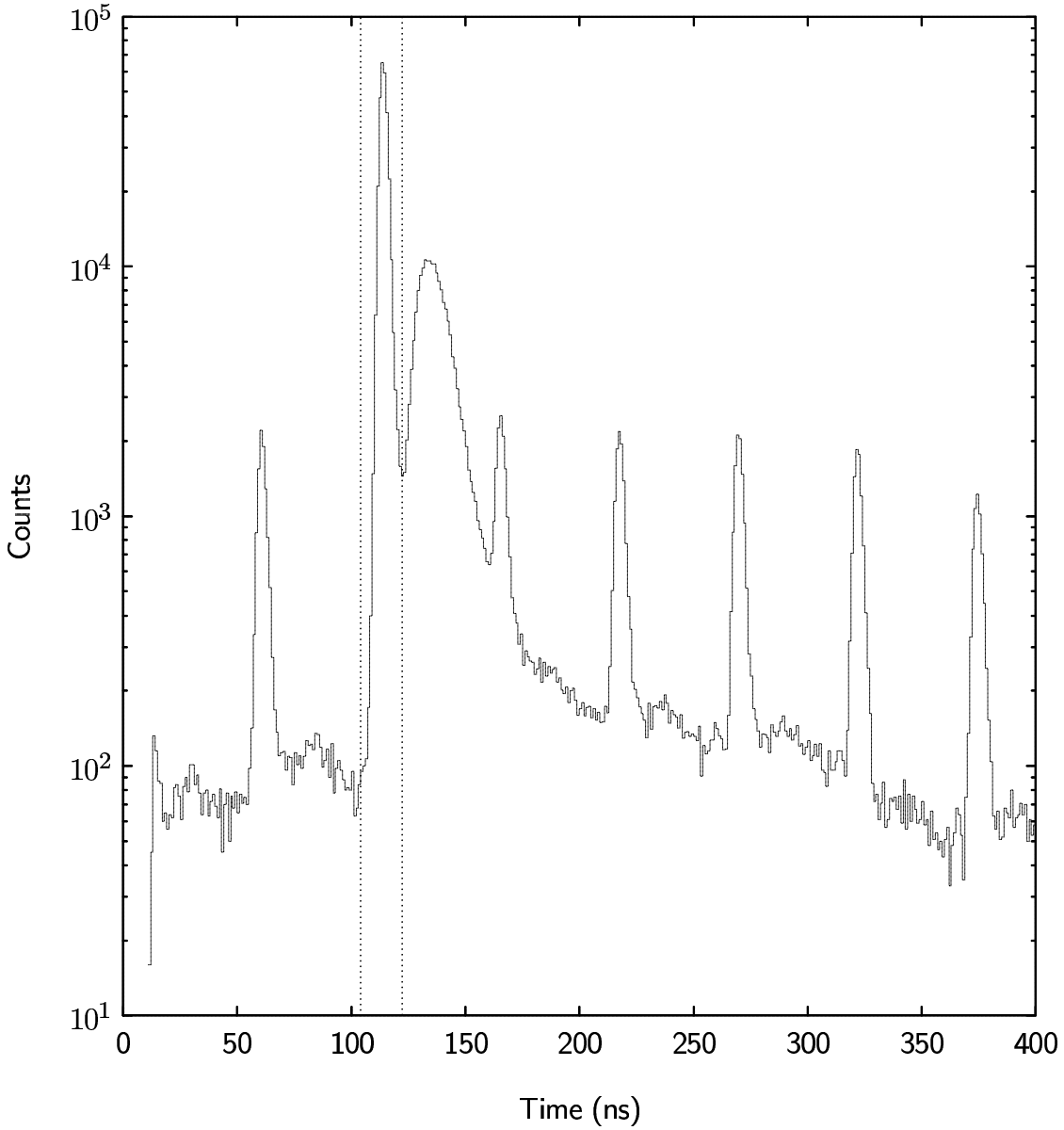

FIG. 11. Sample BaF_2 time spectrum.

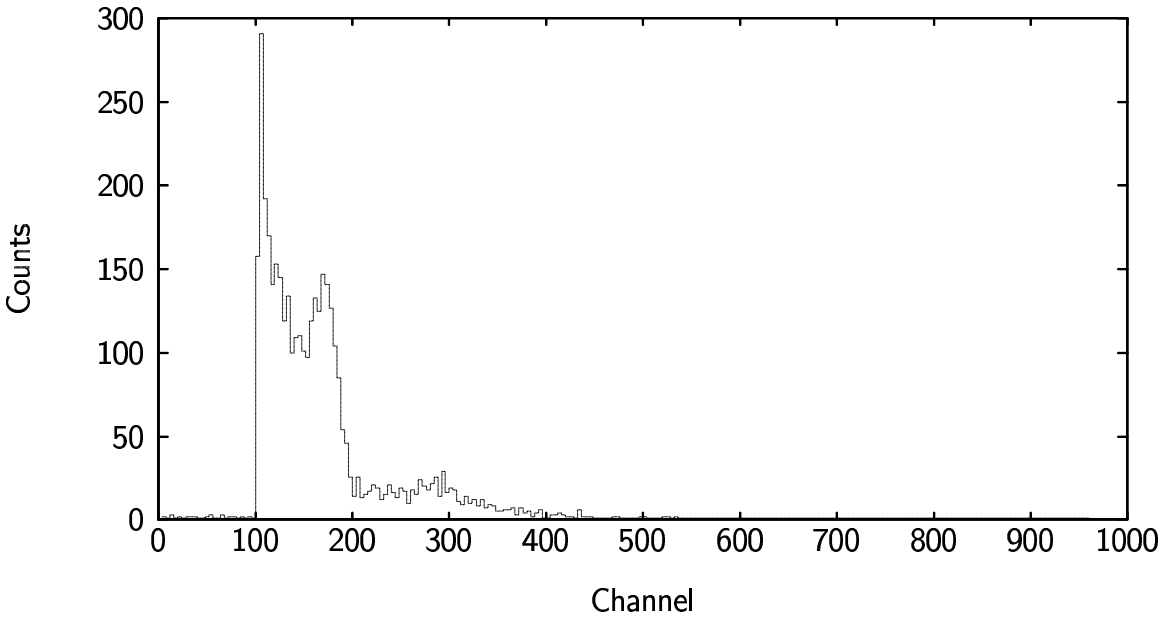

FIG. 12. Sample neutron energy calibration spectrum using ^{60}Co. Note the Compton edge below channel 200 and the pedestal above channel 100.

is indicated by the dotted lines. Absolute time calibrations were not needed in the analysis; only the relative times were required to separate neutrons and γ rays.

II.4.3 DEMON Detectors

The neutron detector energy responses were calibrated using ^{137}Cs and ^{60}Co sources. The AmBe source was also used, but did not give an adequate counting rate due to its central location and the long flight path to the detectors. As expected with this type of scintillator, there is no sharp photopeak, though the Compton edges of the photopeaks are readily visible. Figure 12 shows a sample ^{60}Co calibration spectrum for the total energy. The 1.3325 and 1.1732 MeV γ rays are unresolved. The pedestal just above channel 100 provides a convenient zero-energy calibration point. Using the methodology of Tilquin *et al.*, the energy responses of the detectors

were calibrated to keV electron equivalents (keVee) [100, 103]. A keVee corresponds to the amount of light produced when a one keV electron is detected.

Energy calibrations were performed at both the beginning and the end of the experiment. There was a small amount of drift in the detector response over time. A sample of this is shown in Figure 13. Also shown is the 60%-height of the Compton edge peaks, which gives a standard and reproducible location for dealing with γ rays in the DEMON detectors [100, 103]. Similar drifts towards greater detector response were observed in all eight DEMON detectors.

Calibration curves for the energy response were constructed for each detector, both before and after the experiments. Figure 14 shows a typical case. The slope and x-intercept both decrease by approximately 10% over the course of the experiments. In the analysis, the calibration coefficients were assumed to vary smoothly.

As in the case of the BaF_2 crystals, the time signals from the neutron counters were self-calibrated via the frequency of the beam bursts from the cyclotron. The beam structure is readily apparent in Figure 15. This is a time-calibrated "raw" spectrum from $n5$ accumulated over the whole $^{16}O + {}^{208}Pb$ experiment. Not only are the beam bursts clearly visible as the sharp peaks occurring every $\approx$50 ns, but the spectrum shows that there is good separation between γ rays and neutrons at 60 ns. The γ-ray peak is the large sharp peak just above 50 ns. The neutron peak appears as a large bump beginning above 60 ns. Note that the neutron bump extends over the next two beam bursts. This was accounted for in the analysis (see below). As in the case of the PPAC's, an Ortec Model 462 time calibrator was used with a range

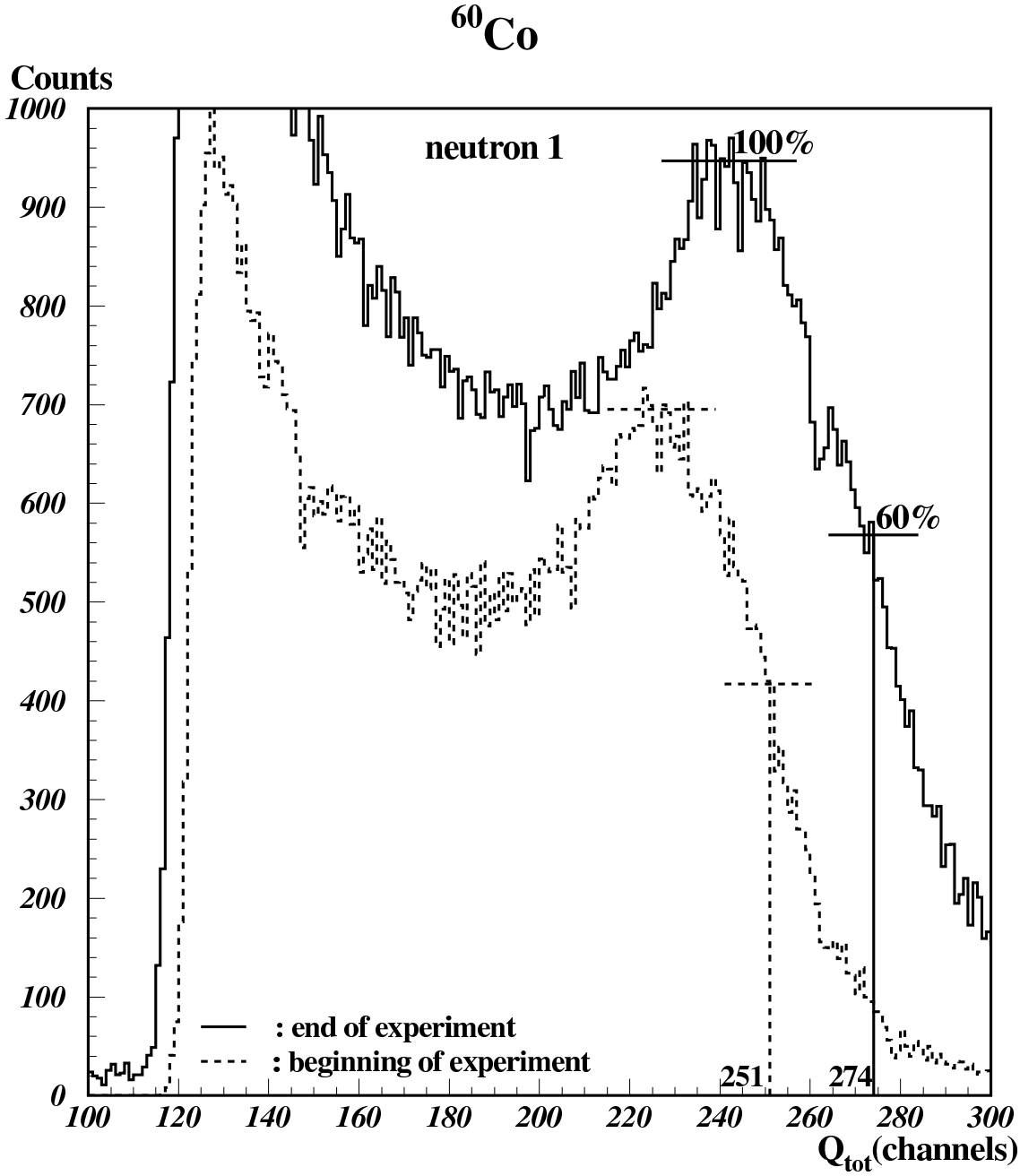

FIG. 13. ^{60}Co calibrations for $n1$. The calibration data taken before the experiment are indicated by the dashed line, while those after the experiment were complete are indicated by the solid line.

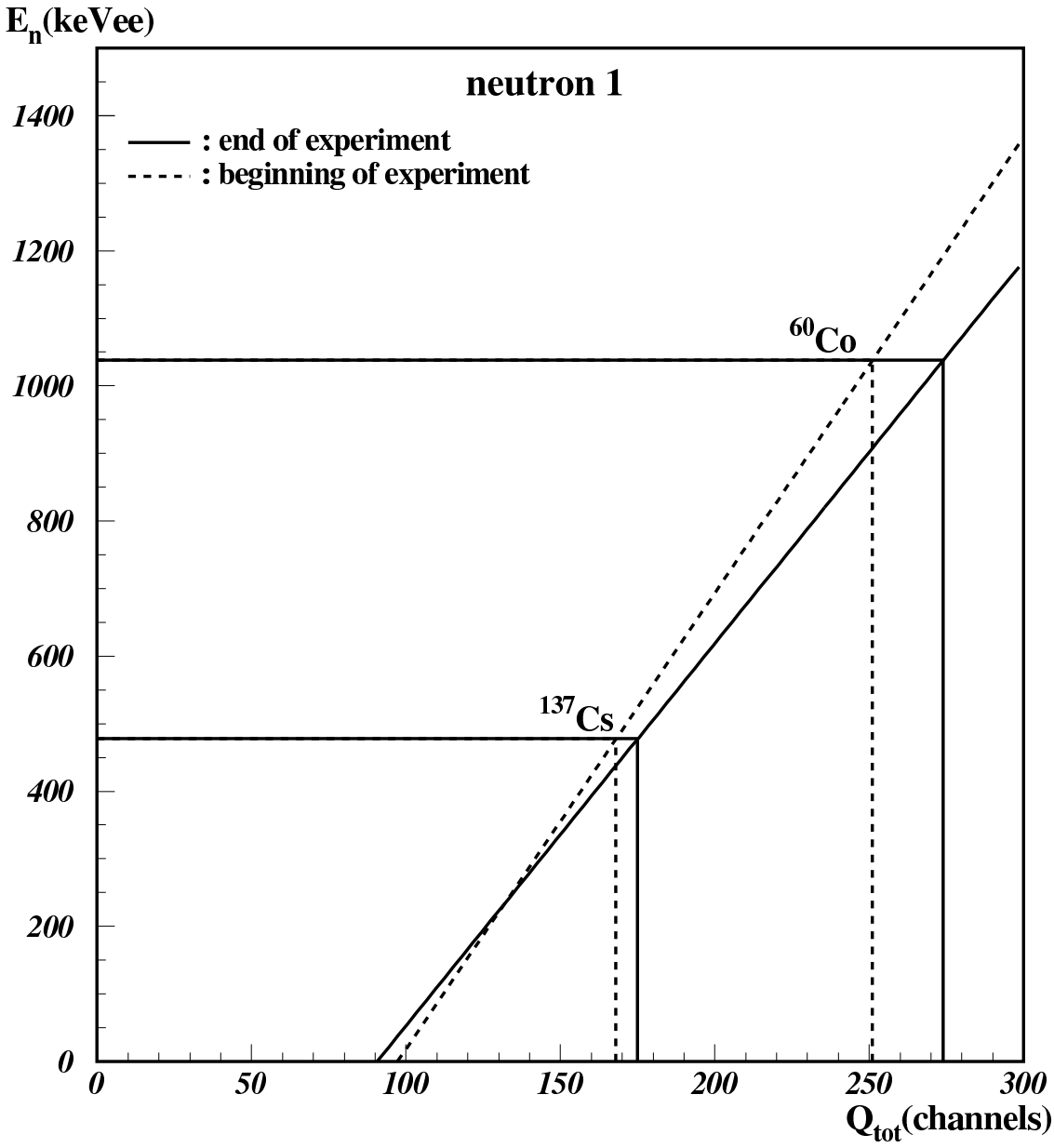

FIG. 14. Calibration curves constructed from the before and after calibration data for detector $n1$.

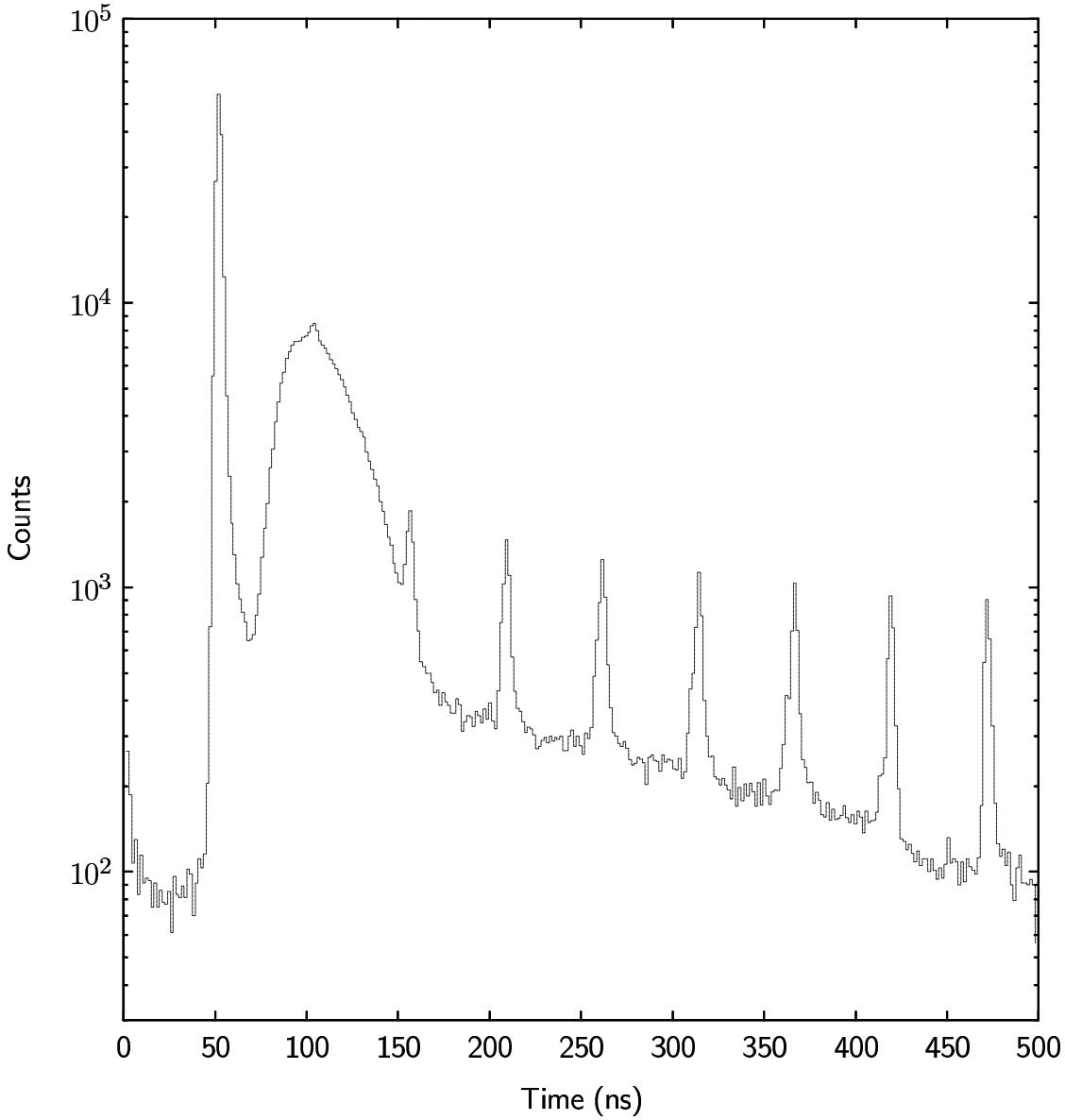

FIG. 15. Sample raw time spectrum for the DEMON detectors.

of 320 ns and a peak interval of 10 ns. Using both time calibration methods, a very good overall time calibration for the neutron counters was obtained.

II.5 Summary

Four experiments using different targets and two different beams were performed. Data were taken from one start detector, two PPAC's, eight neutron counters, and 144 BaF_2 γ-ray counters, for a total of 465 parameters. The detectors were placed about the target in such a manner as to minimize background and maximize detection efficiency (see Figure 1 and Table 6). Data were recorded using the acquisition suite ORPAS and written to 8mm tape. Energy and time calibrations were taken at the completion of the last experiment ($^{4}He + {}^{188}Os$).

CHAPTER III

DATA ANALYSIS

Data analysis was separated into three parts. Since the PPAC's provided the trigger, this information was processed first. The various signals from the PPAC's enabled one to reconstruct the fission fragment velocities, angles, masses and energies and to establish an absolute event start time (t_0). The PPAC analysis was carried out on a dual-processor Pentium Pro machine following the methodology of Chubaryan *et al.* [108]. An iterative software procedure was developed to establish the t_0 and x-y position information for the fragments, providing physically meaningful fission fragment information on an event-by-event basis (see the following Section).

The PPAC data were addressed first because both the γ-ray and the neutron data analysis required a definition of the timing. After the PPAC analysis was complete, the gamma (BaF_2) and neutron (DEMON) portions were analyzed independently. The data from the PPAC analysis were used to set gates on true fusion-fission events, fission mass asymmetry, TKE, and other parameters. The γ-ray analysis was carried out on a VAXStation 4000 Model 90 under VAX/VMS v6.2 using the analysis environment LISA [109], as is covered in detail in Section 2 of this chapter. The neutron analysis was based on the technique of Hinde *et al.* [14], modified especially for the DEMON detectors used here [110]. This is discussed in Section 3 of this chapter.

III.1 Data Reduction

As noted above, the high speed of the data acquisition permitted the use of trigger conditions that were not very restrictive. Consequently, a significant number

of bad events (i. e. noise, non-fission events, etc.) were written to tape. This approach was taken to avoid biasing the data and minimized the number of lost fission events. In fission fragment analysis, it was possible to reject essentially all of the bad events.

For the γ-ray cleanup analysis, each event was required to have all PPAC parameters present (i. e. a complete fission event) and at least one BaF_2 crystal with a γ ray above a threshold ($\approx$0.8 MeV). The data were then corrected for random coincidences. During the measurements, the value of the gamma energy threshold was chosen to be 5–10% less than that used in the γ-ray analysis to facilitate threshold matching in the subsequent analysis.

Moreover, for the purpose of a GDR γ-ray analysis, the energy region of interest begins at $\approx$5 MeV, where the γ rays are primarily statistical. The fact that the present work had thresholds much lower than that proved useful in comparisons with statistical model calculations and showed that nuclear structure effects can bias the data analysis (see below). The first pass data cleanup reduced the data by about a factor of four, aside from the inclusion of extra data words for the fission fragment velocities and angles on an event-by-event basis. The cleanup of the neutron data proceeded similarly. Neutron emission is much more probable than GDR γ rays, thus good statistics for the neutron method of fission time scale evaluation were obtained for all systems studied in the experiment.

Yet another pass through the data provided the total yield of good fission events irrespective of γ rays and neutrons. This was used to obtain the absolute fission yield of γ rays and fission neutrons and thus their multiplicities.

Calibrations of the PPAC's were essential in the analysis. This included the absolute position and the TOF information. This necessitated an analysis of the data in several hundred separate subsets. The calibrations were adjusted to account for slight changes in the gas pressure in the PPAC's and drifts in the beam optics. The latter were due to changes in the cyclotron tuning and drifts in the magnetic field of the transport system. It was extremely important to know the position of the beam on the target due to the tight geometry of the PPAC's.

The TOF and position data from the PPAC's were used to calculate the velocities and in-plane (θ) and out-of-plane (ϕ) angles for each fission event. The non-projective geometry of the detectors was taken into account.

Fission was assumed to follow complete fusion of the incident nuclei, which was later borne out by examination of the resultant spectra. Thus binary kinematics were used. Conservation of mass gives

$$M_{proj} + M_{tgt} = M_1 + M_2, \tag{22}$$

while conservation of momentum in the center of mass gives

$$M_1 v_1 \sin\theta_1 = M_2 v_2 \sin\theta_2, \tag{23}$$

$$M_1 v_1 \cos\theta_1 + M_2 v_2 \cos\theta_2 = M_0 v_0. \tag{24}$$

In the above, the subscripts 1 and 2 refer to the fragments, $M_0 v_0$ is the incident beam momentum, and M_{proj} and M_{tgt} refer to the masses of the projectile and target.

Starting values for the velocities and masses of the fission fragments were then determined using the raw data. Refined distributions were obtained iteratively after

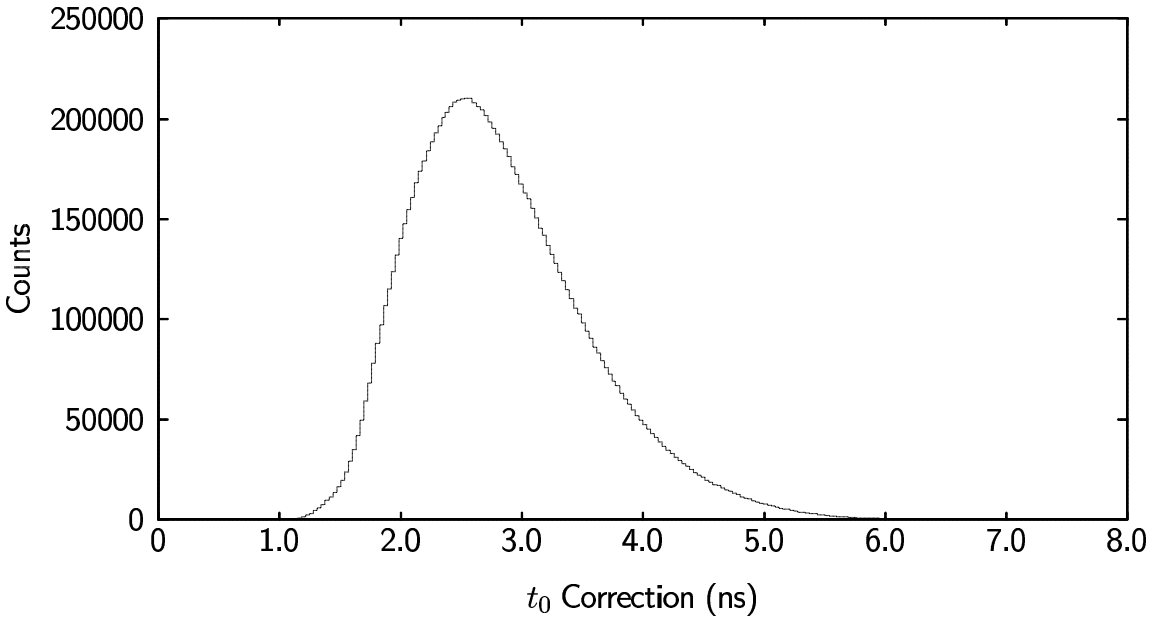

FIG. 16. Plot showing the corrections to t_0 in nanoseconds. The figure shown was accumulated over the whole $^{16}O + ^{208}Pb$ experiment.

corrections for the target, the calibrations, and energy losses in the various detectors. Convergence of the mass and TKE was used to further filter the data. The semi-empirical methods of Benton and Henke provided for the needed corrections for the rate of energy loss in various media [111]. This typically involved another two to four iterations through the data.

Resultant corrections to the start time showed differences of about 2.5 ns for the various systems. This is partially reflected in the t_0 for the $^{16}O + ^{208}Pb$ system, as shown in Figure 16. In this case, the correction to t_0 was 2.8$\pm$0.7 ns on average. The correction to the data was an extremely tedious procedure.

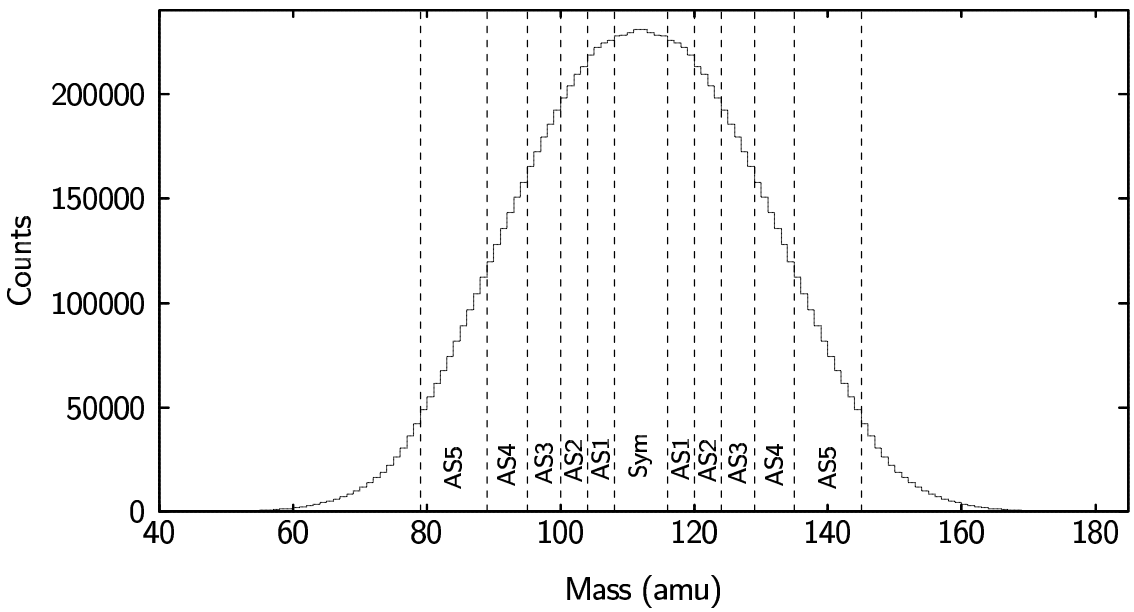

FIG. 17. Fragment mass distribution for ^{16}O + ^{208}Pb. Since binary fission was assumed, the mass distribution is necessarily centered exactly at symmetric fission. The vertical lines indicate mass cuts used in the γ-ray analysis.

The resulting mass distribution for the ^{16}O + ^{208}Pb case is shown in Figure 17. The six sets of mass cuts used in the subsequent γ-ray analysis are also shown. The gates were chosen to equalize the statistics in each bin. The values for the cuts are listed in Table 9.

The total kinetic energy of the fragments was determined using the reconstructed velocities and masses with the relationship

$$TKE = \frac{M_1 {v_1}^2}{2} + \frac{M_2 {v_2}^2}{2}. \tag{25}$$

The TKE distribution for the reaction ^{16}O + ^{208}Pb is plotted in Figure 18. The mean value was 162 MeV for the ^{16}O + ^{208}Pb data, which agrees with the Viola

TABLE 9. Mass cuts used for the $^{16}O + ^{208}Pb$ γ-ray analysis.

Cut	Range (amu)
Symmetric	$108 \leq A \leq 116$
Asym1	$104 \leq A < 107$, $117 < A \leq 120$
Asym2	$100 \leq A < 103$, $121 < A \leq 124$
Asym3	$95 \leq A < 99$, $125 < A \leq 129$
Asym4	$89 \leq A < 94$, $130 < A \leq 135$
Asym5	$79 \leq A < 88$, $136 < A \leq 145$
Asym6	$39 \leq A < 78$, $146 < A \leq 185$

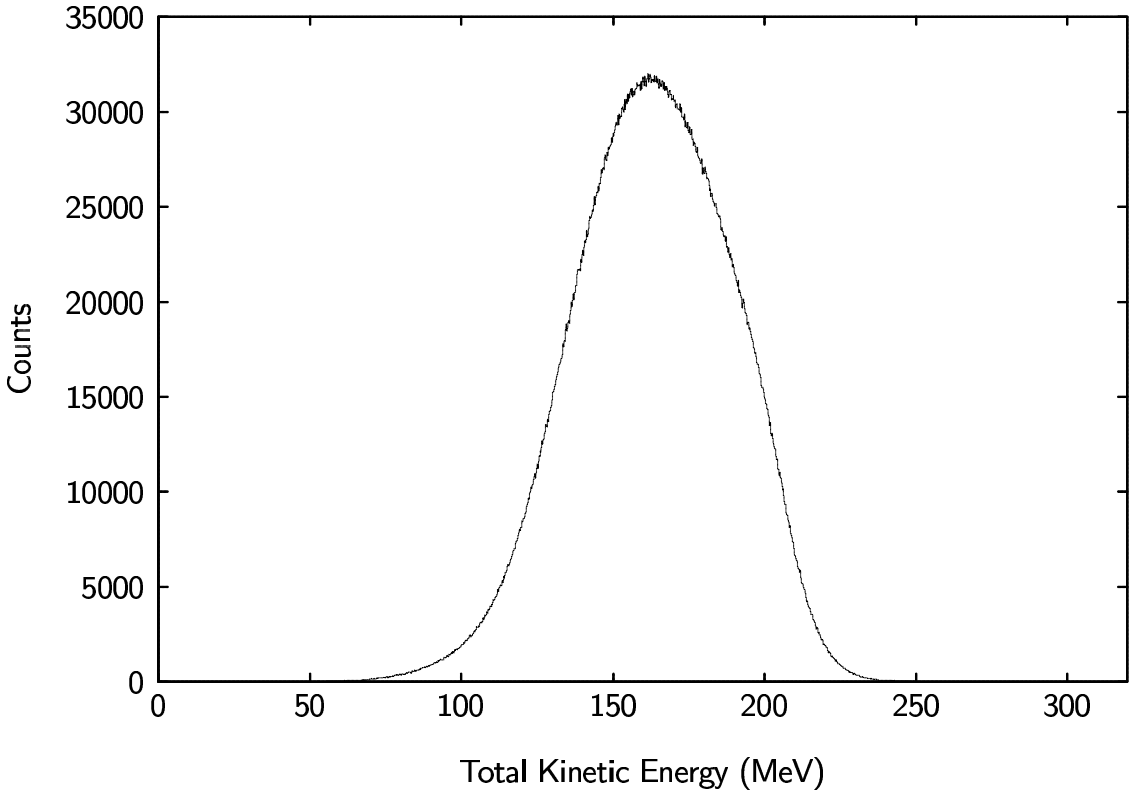

FIG. 18. Sample total kinetic energy distribution of the fission fragments. This plot was obtained for all of the $^{16}O + ^{208}Pb$ runs.

systematics [112] given by

$$\langle TKE \rangle = (0.1189 \pm 0.0011)\frac{Z^2}{A^{1/3}} + 7.3(\pm 1.5), \tag{26}$$

where $\langle TKE \rangle$ is the average total kinetic energy release in fission in MeV and $Z^2/A^{1/3}$ is the Coulomb parameter of the fissioning nucleus. The other reactions showed similar agreement. A three-dimensional plot of single fragment mass versus total kinetic energy is shown in Figure 19 to further illustrate the quality of the data.

The overall shape of this TKE spectrum is slightly skewed to higher TKE values. This is largely due to the measured quantities and the subsequent analysis using Equations (22)–(24). A similar effect would have been observed if there was a significant contribution from incomplete fusion. For the systems studied here, this is quite unlikely.

As a final check, events with meaningful fission fragment angles were accepted, i.e.

$$\theta_1 + \theta_2 = 180^\circ \pm \delta\theta. \tag{27}$$

Here $\delta\theta$ is a small deviation ($\approx 4^\circ$), which has contributions from a number of sources. Major sources of this angular dispersion are the tight geometry and neutron evaporation from the fission fragments.

The effect of the procedures used in the PPAC analysis can be seen in Figures 20 and 21, which show counts in x- and y-positions. Again the $^{16}O + ^{208}Pb$ runs are used as an example. The dashed line indicates the raw position data for only 12 runs. The dotted line represents the position data seen after completion of the PPAC

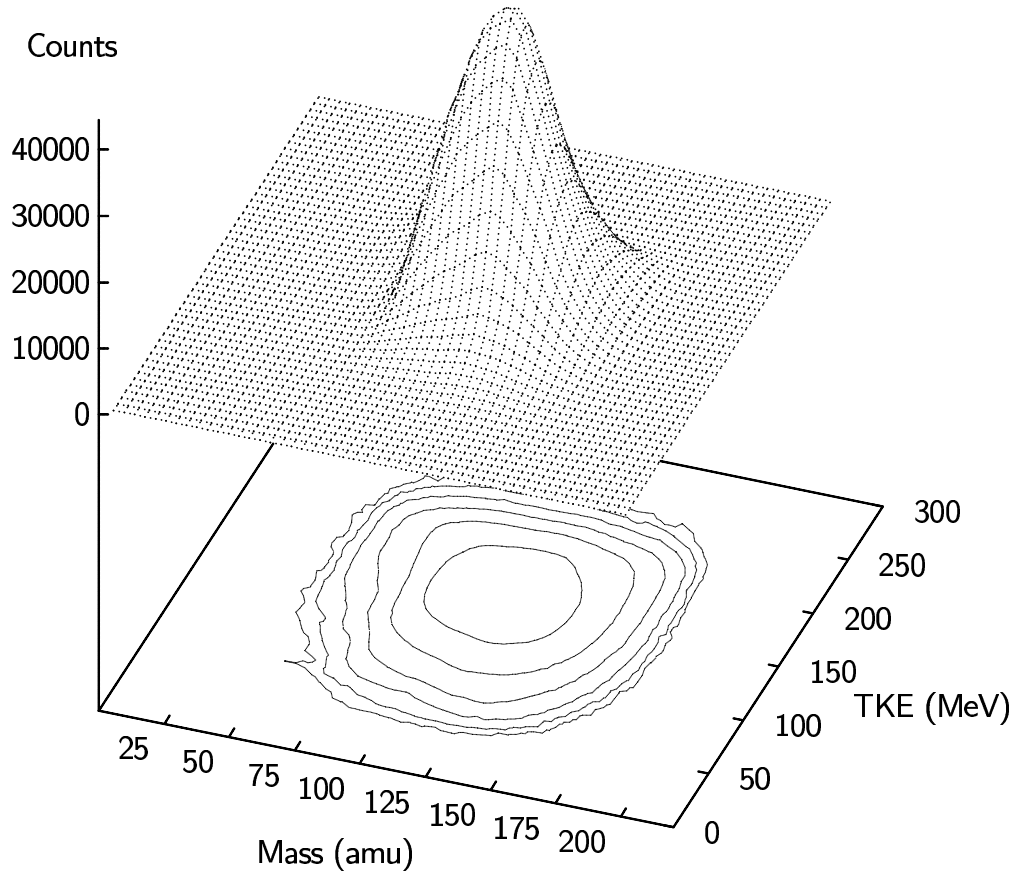

FIG. 19. Three-dimensional plot of fragment mass versus total kinetic energy. Both a mesh and a contour plot are shown. The contours are in log scale.

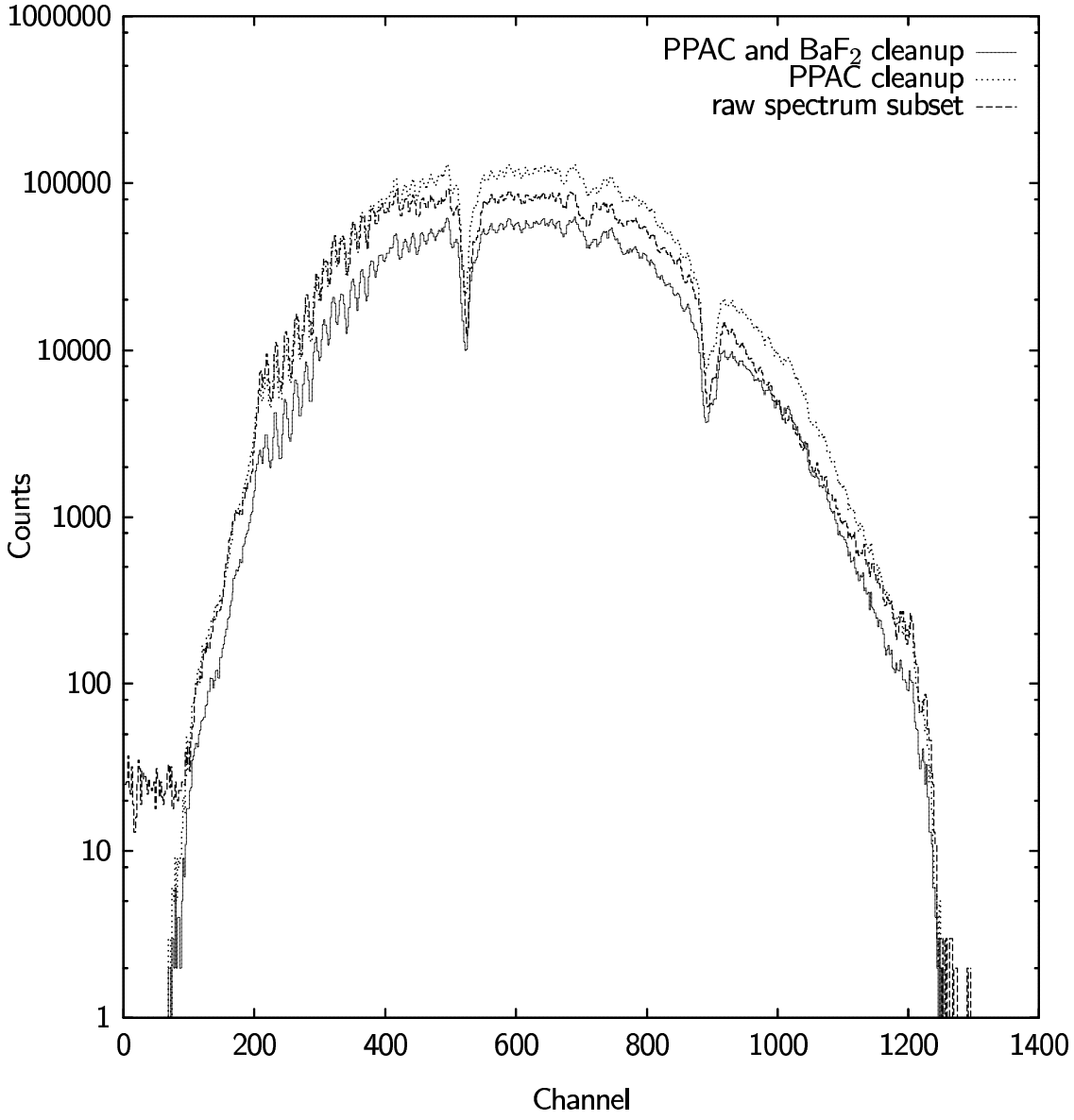

FIG. 20. X-direction position data of PPAC 2 before (dashed line, raw data) and after "cleanup" (solid line). The raw spectrum (dashed line) only includes 12 runs. The dotted line is an intermediate spectrum showing the results of the only PPAC analysis and cleanup.

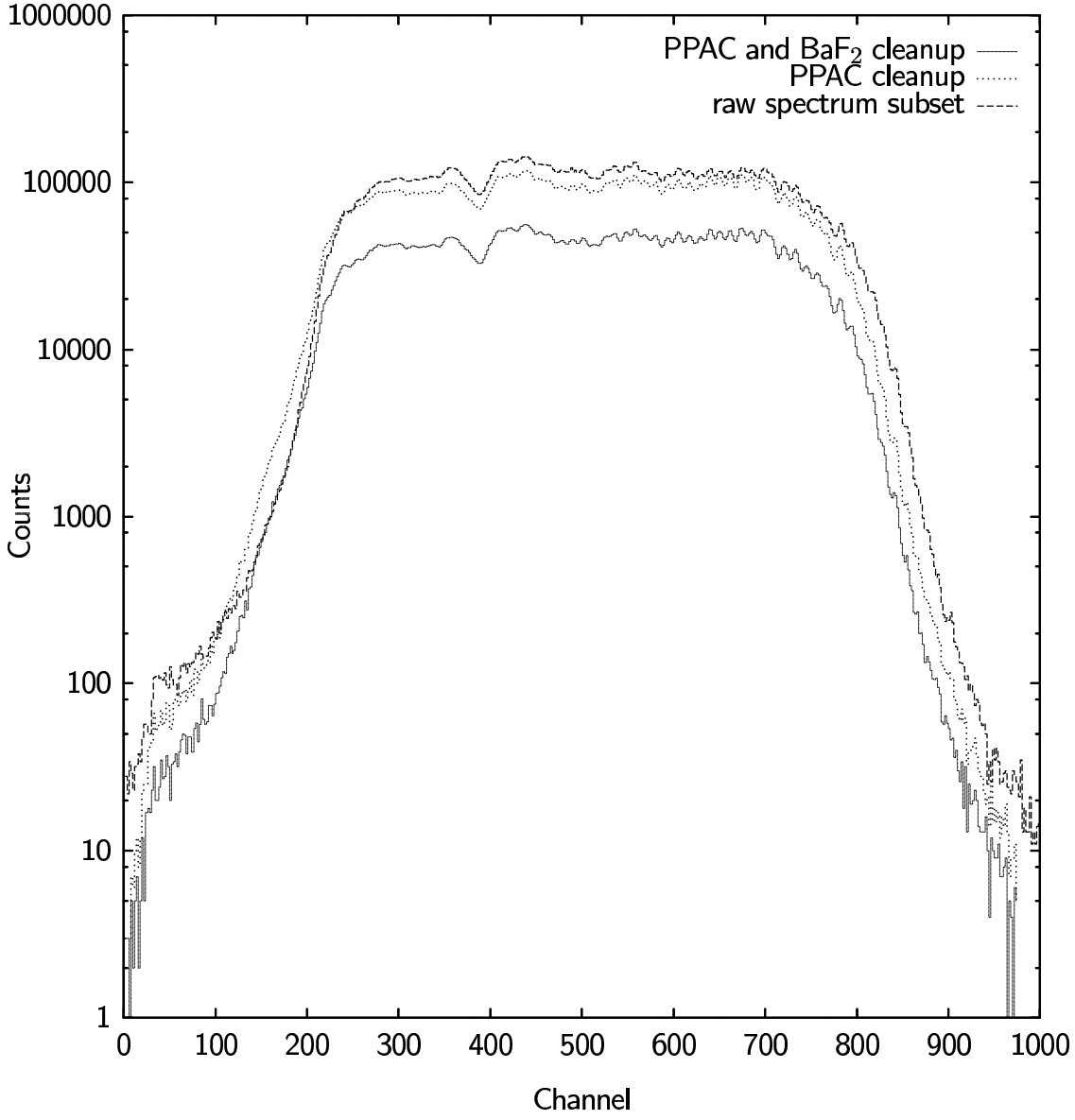

FIG. 21. Y-direction position data of PPAC 1 before (dashed line, raw data) and after "cleanup" (solid line). The raw spectrum only includes 12 runs. The dotted line indicates the results of only the PPAC analysis and cleanup

analysis. The solid line indicates the same data after additional refinements from the γ-ray analysis (see the following section for details). The thick calibration wires are clearly visible in Figure 20 as dips in the spectrum at channel numbers 500 and 875. The dip in the data in Figure 21 at channel 375 is due to two of the thin wires being accidentally electrically fused.

The values of the correction to t_0 and of the fission fragment velocities and angles are appended to the end of each accepted event, separated by a sub-header. This new event-by-event reduced data stream is rewritten to tape and becomes the input data for the γ-ray analysis.

III.2 Gamma Ray Analysis

In parallel to the fission fragment analysis, much work was carried out on the γ rays. The cross-section for GDR γ-ray emission is about three orders of magnitude smaller than that of fission. Every effort was taken to develop procedures for retaining the highest possible statistics in the GDR region. Using LISA, a custom subroutine GETORPHASDTA was implemented to read the data. Another subroutine DECODE was employed to put the data in the required format. Other custom subroutines for LISA were fashioned to perform additional manipulations of the data on an event-by-event basis.

The subroutine SETUP was fashioned to read in the energy calibration coefficients and time gates for the BaF_2 detectors. This also provided flags and values used for various types of operations, e. g. cosmic ray rejection, fission and γ-ray shower reconstruction (separate for the edge and non-edge regions), and BaF_2 time-gates.

Another subroutine (TYERECON) was used to reconstruct electromagnetic showers across multiple crystals. Here reconstruction was only applied to those crystals completely surrounded by neighboring crystals (42 out of 72, 7×6, the so-called "core" or "primary" crystals). These neighboring crystals functioned as transverse loss detectors. This algorithm identified the crystal with the greatest energy deposition in either of the two pods. The energy of this primary crystal was then summed with those of its six nearest neighbors to give the energy of the reconstructed shower:

$$E_{sh} = E_{high} + \sum_{x=1}^{6} E_x. \tag{28}$$

In the above, E_{high} is the energy in the primary crystal and E_x is the energy in the x^{th} neighboring crystal.

As suggested by Wolf [113], an algorithm was devised to salvage showers with the greatest energy deposition in the edge crystals of the pod, i. e. crystals not completely surrounded by neighbors. This is significant since 30 of the 72 detectors in each pod are edge crystals. The algorithm required that at least 10 keV was deposited in a neighboring crystal. As an illustration this, Figure 22 shows the multiplicities of reconstructed showers for both core and edge showers. The addition of the edge-reconstructed events only adds an additional ≈5% to the number of counts, even with the lowest possible threshold. Additionally, the outer crystals tend to see a much higher neutron background since they shield the core crystals from stray neutron flux to a large extent. In the final analysis, this edge-reconstruction algorithm was not used because it did not significantly improve the statistics and added uncertainty in

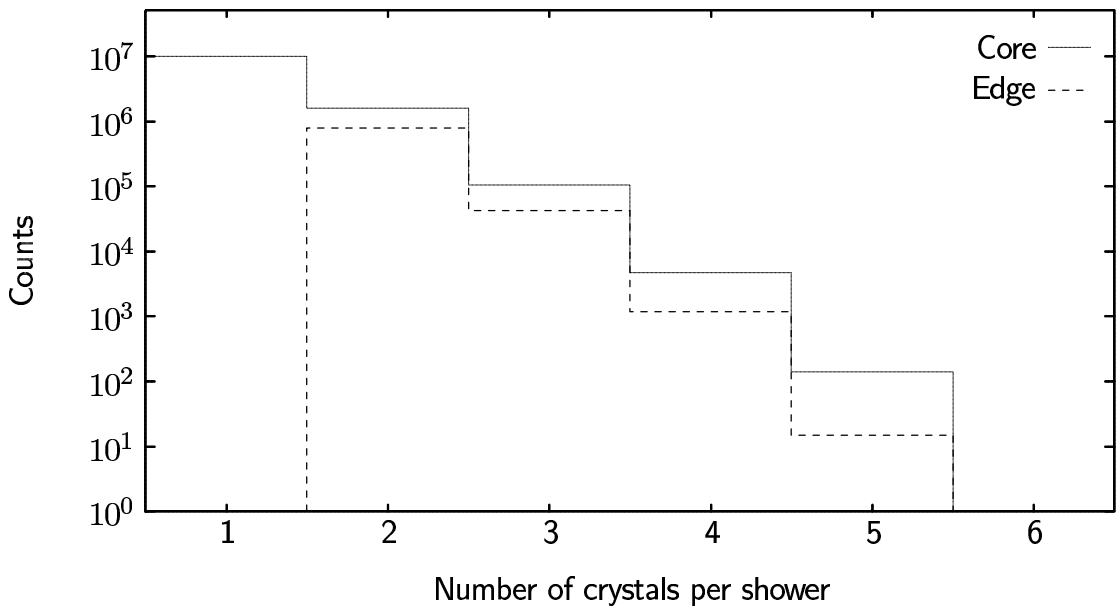

FIG. 22. Edge (dashed line) and core (solid) shower reconstruction compared for all $^{16}O + ^{208}Pb$ runs.

the total γ-ray energy deposition. While edge reconstruction is useful for much higher γ-ray energies, it was of little use in the current work.

Several algorithms were constructed in the subroutine INSERT, to include the centrality condition of Jabs [107] and to reject contamination of the γ-ray spectra by cosmic rays. This centrality condition requires that no more than a certain fraction, F, of the energy deposited in the primary crystal be present in the sum of the surrounding six, where F is given by

$$F = \frac{1}{E_{high}} \sum_{x=1}^{6} E_x. \tag{29}$$

The other variables are the same as in Equation (28). Jabs has previously shown that $F = 0.3$ is suitable for high-energy photon work [107]. For this work, $F = 1.5$ was found to be more appropriate.

The large difference in F values comes about both from the different triggers used and the different energy regimes studied. In Jabs' work, the detectors were self-triggered and running in a "singles" mode. This increased the sensitivity to the cosmic ray background, requiring an aggressively low F to remove as much of that background as possible. Additionally, when studying higher-energy γ rays cosmic rays are intrinsically more of a problem. This comes about due to the fact that the average energy deposition by cosmic rays in BaF_2 crystals used here is centered at 47 MeV. The low-energy tail of the cosmic-ray distribution can be significant even below the GDR region when running in a "singles" mode. Given that reconstruction might possibly add cosmic-ray contribution from up to 6 neighboring crystals, a lower F was utilized. The F-value employed is consistent with γ ray shower calculations.

The applicability of the centrality condition is illustrated in Figure 23, which shows an overlay of three separate events in the BaF_2 Pod 2. The different clusters around crystals 224, 276, and 272 shown by shaded or darkened hexagons represent single events. The top-most cluster would be rejected since the summed energy of the nearest neighbors of the primary crystal (224) is far more than 50% of the central crystal's energy. In fact, the value of the summed energy of the nearest neighbors was 220% of that of crystal 224. Note that crystal 244 would not be included in the sum since it is not a nearest neighbor. The cluster about crystal 276 would not be rejected since the nearest neighbors' sum energy is only 60% of that of the central crystal. A very rare event is shown in the remaining shower, centered about crystal 272. In this case the event is not rejected, but some of the shower energy

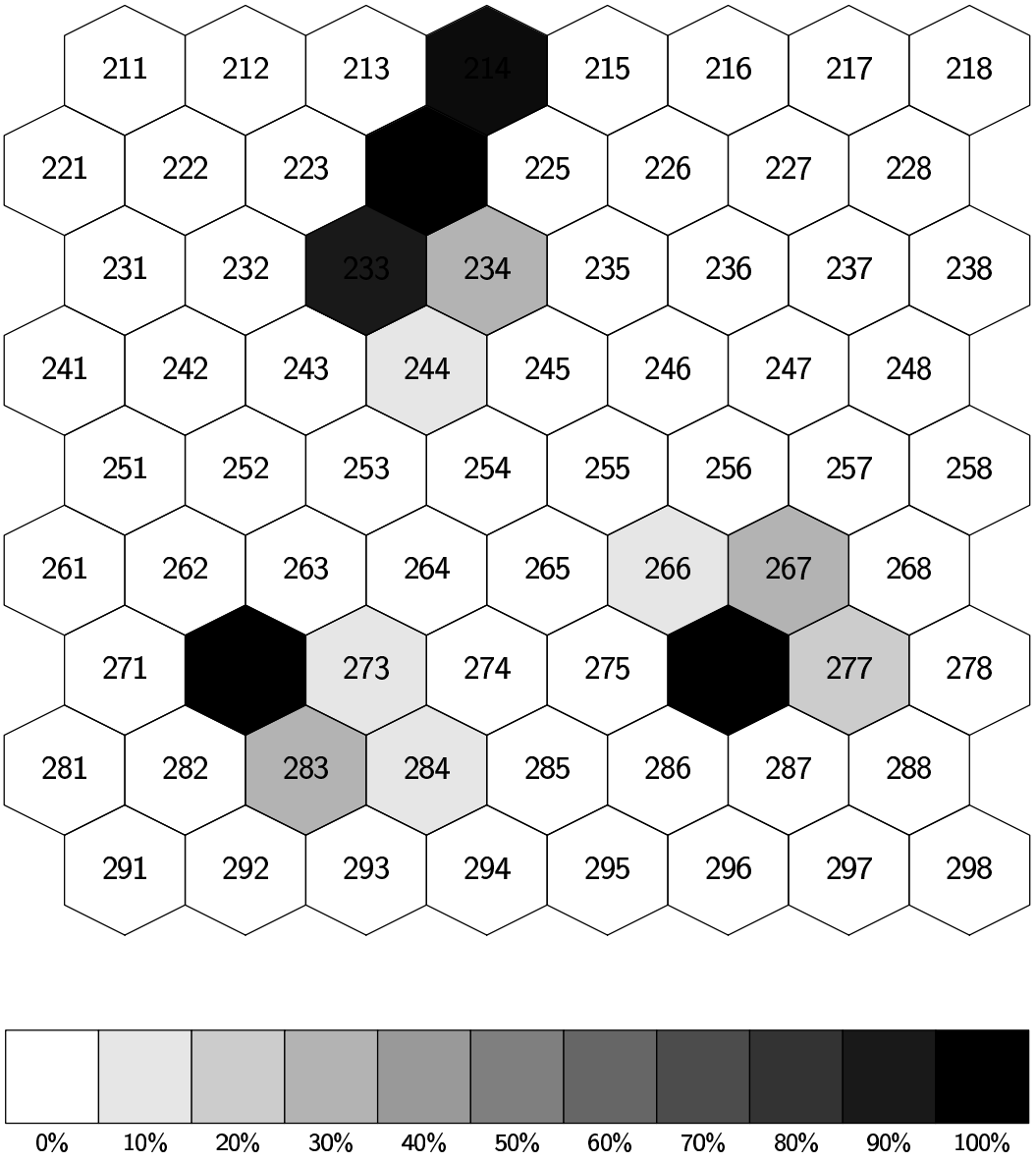

FIG. 23. Illustration of cosmic ray rejection in a BaF_2 Pod using the centrality condition. Three separate events are shown superimposed upon the pod layout. The top-most event was rejected while the other two were not (see text for explanation). The legend at the bottom indicates the percentage of energy detected relative to that seen in the primary crystal. The Pod 2 is used in this example.

would be lost since crystal 284 is not included in the sum. This loss is a very small effect, both due to the rarity of this type of event and the small amount of leakage beyond the nearest-neighbor crystals.

The subroutine INSERT also included an algorithm to correct the BaF_2 timing signals using the t_0 of the fission fragments. Each of these subroutines and algorithms was tested and verified on the raw data before the reduced data were available. Using the t_0 correction, the threshold matching, the timing gates, the shower reconstruction, and the centrality condition (with F=1.5) were employed in the final analysis. These gave the cleanest fission-correlated γ-ray spectra. Figure 24 shows reconstructed shower spectra for three phases: a calibrated-only "raw" spectrum, a spectrum after the fission fragment analysis, and a fission correlated spectrum with both threshold and time matching of the γ rays. The first two spectra show considerable γ-ray yield below 10 MeV. This is largely due to random events arising from neutron capture in the BaF_2 arrays and in the surrounding material. Once all the gates have been applied (third spectrum), those events are eliminated. These observations stress the need for excellent trigger timing in GDR γ-ray measurements.

The final step in the analysis was background subtraction of the γ-ray energy spectra. Timing gates were set on random beam bursts in the BaF_2 TDC spectra and used to produce background γ-ray spectra. Subtraction of these from the original time-gated spectra produced background-subtracted spectra which were used as the final γ-ray energy spectrum. Figure 25 shows the efficacy of this procedure for ^{16}O + ^{208}Pb. The dotted line represents the total γ-ray spectrum before background

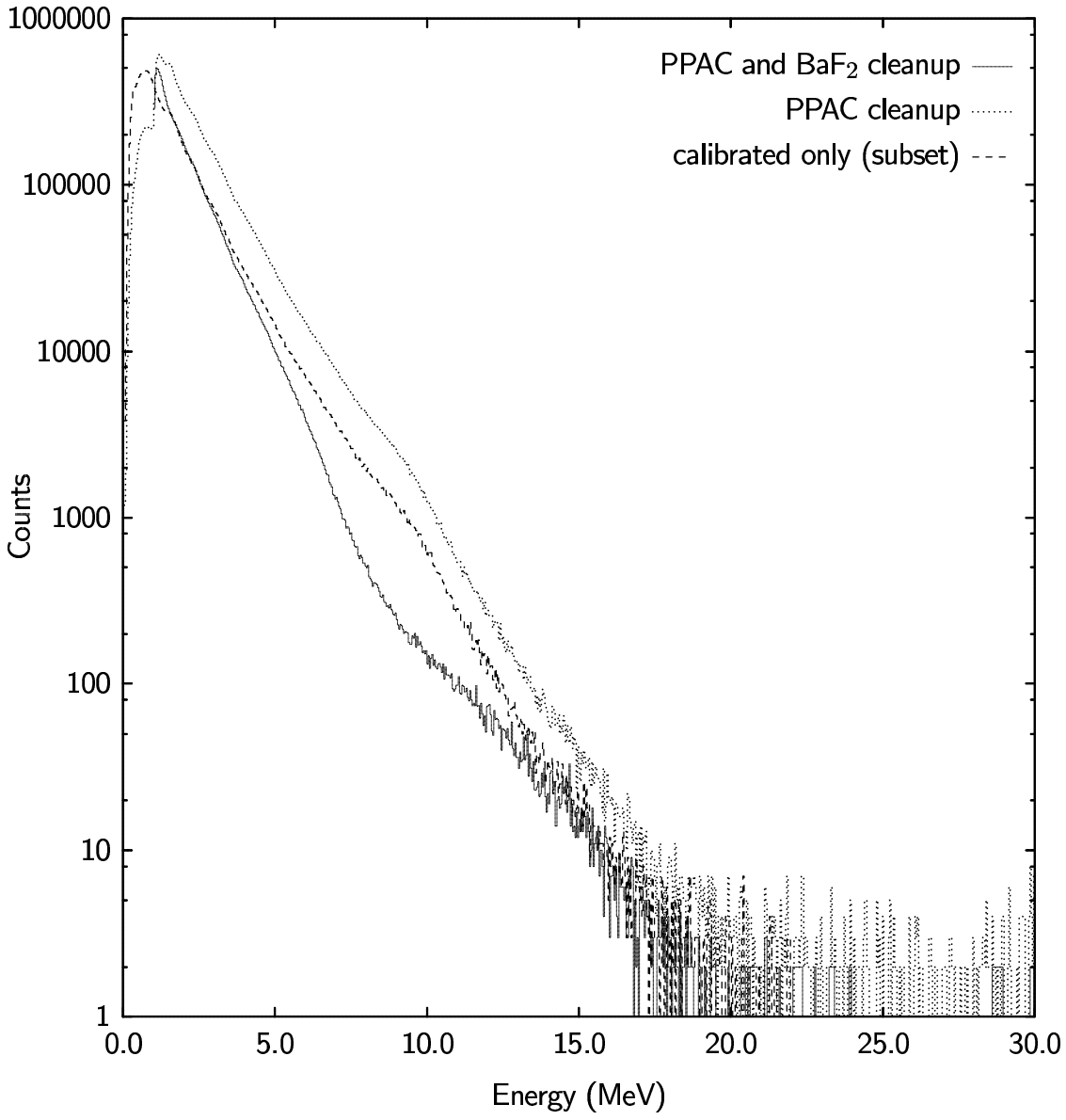

FIG. 24. BaF_2 spectra at various stages of the $^{16}O + ^{208}Pb$ analysis. The final spectrum is indicated by the solid line. The dashed line is a subset of the runs (only 12 runs) and the dotted line represents the results of the PPAC analysis and data reduction for all runs.

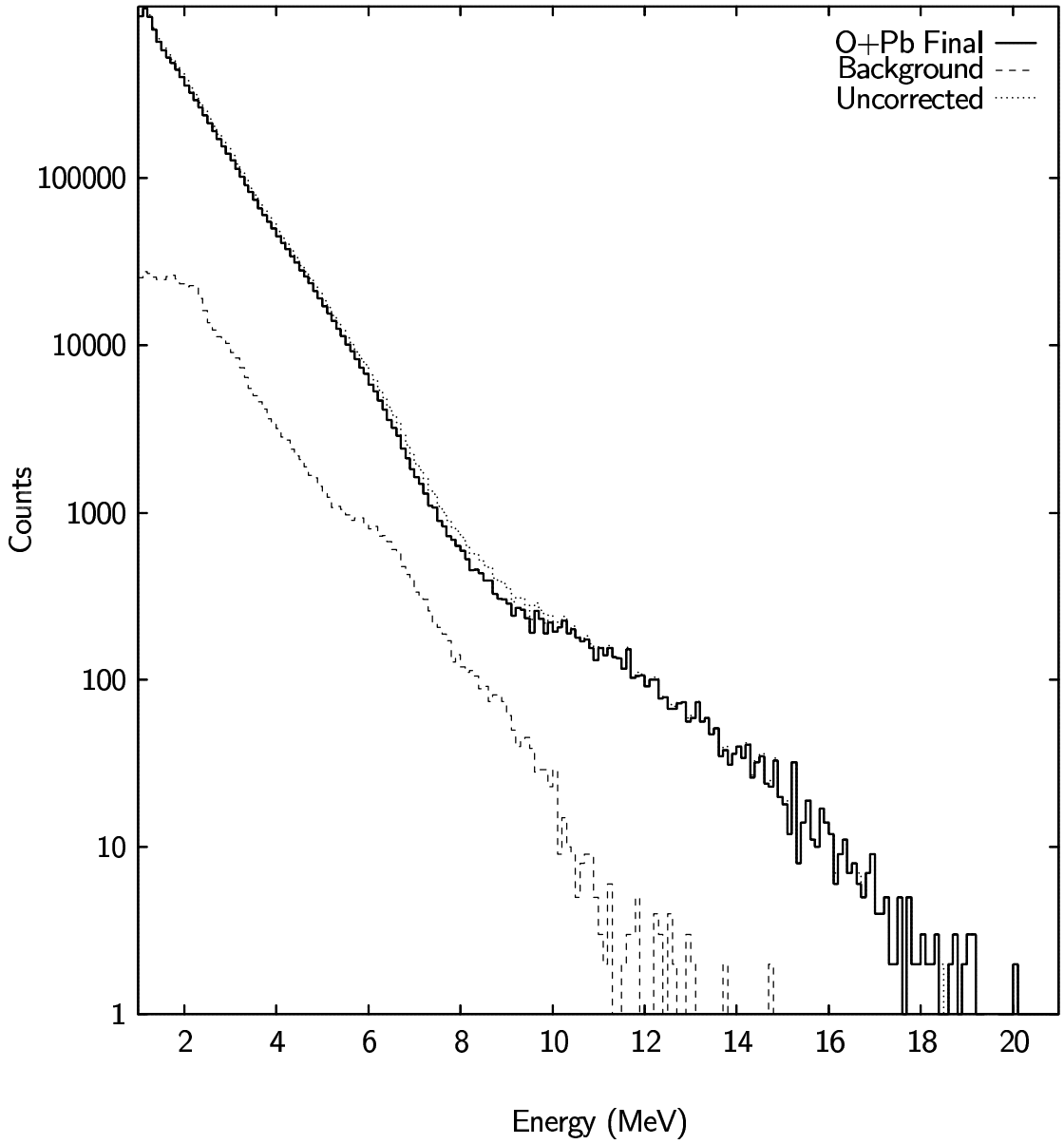

FIG. 25. The results of subtracting the background for the total $^{16}O + ^{208}Pb$ γ-ray spectrum. 100 keV bins are used.

subtraction. The dashed line below indicates the background spectrum. The total γ-ray energy spectrum resulting from the difference of the two is indicated by the darker solid line between the curves. Keeping in mind that the figure is a semi-log plot, it is apparent that background subtraction is necessary since it affects the slope in the statistical γ-ray and low-end neutron-capture regions (4–8 MeV). This correction is clearly important for statistical model comparisons. It should also be noted that the random subtraction is even more important in less fissile systems due to the larger background. Additionally, the subtraction of the background reveals the true extent of the GDR contribution.

Once all the final gates and conditions were set in place, it is possible to produce a multiplicity of γ rays (M_γ) for each reaction. This is obtained by dividing the total γ-ray spectrum by the number of fission events. Typical results are shown in Figure 26, which is not corrected for intrinsic detector response (this final correction is applied to the model calculations instead). Several features are readily apparent. The M_γ decreases approximately exponentially in the statistical region ($\approx$2–7 MeV). Above about 8 MeV a prominent GDR bump is visible. Further examination of the data reveals an additional broad bump peaked at $\approx$5 MeV. This feature has been previously seen [114] and is briefly addressed in the following chapter.

III.2.1 BaF_2 Detector Response

In order to estimate the fission time scale using GDR γ rays, the spectra were compared to statistical model calculation codes (see next chapter). These codes do not include detector responses and therefore it is necessary to simulate this separately.

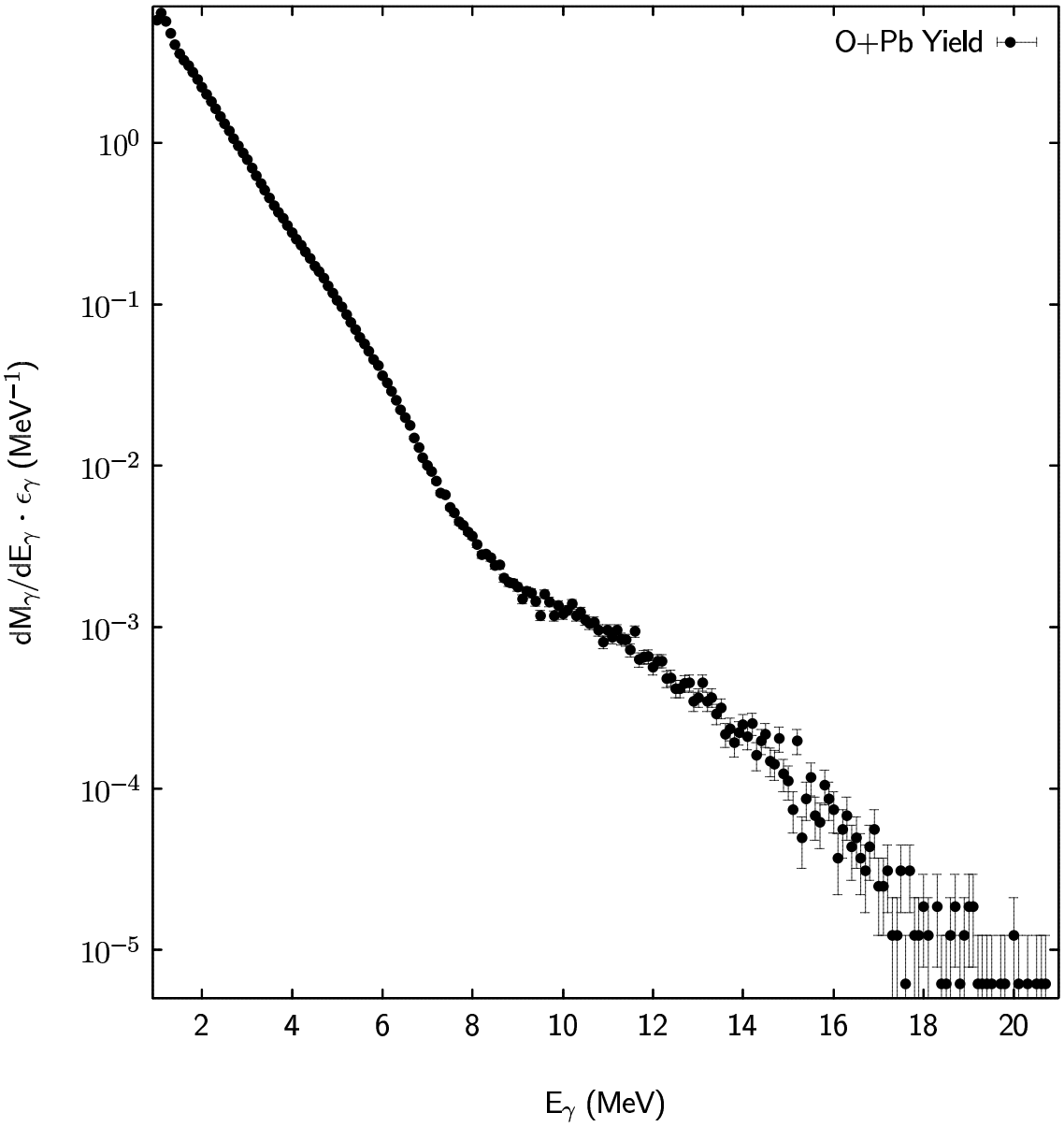

FIG. 26. Absolute fission γ-ray multiplicity for $^{16}O + ^{208}Pb$. Bin size is 100 keV.

The response functions were then folded into the results of the statistical model calculations. The response of the BaF_2 crystals was simulated using the code EGS (Electron Gamma Shower) [115], version EGSBOSS2 [113]. This software follows the energy deposited by a photon as it passes through a given medium. The cascade is continued until reaching a predefined minimum energy threshold. The user inputs include a spatial description of the experimental setup, the initial photon energy and direction, material types, and the minimum energy threshold. It is essential to include any materials the incident photon passes through before being detected. Equally important, one needs a thorough description of the detector itself.

These spatial descriptions consist of a set of any number of three-dimensional regions defined by planes. By carefully constructing these planes in user-supplied subroutines, it was possible to describe the major components of the experimental setup, including the target ladder, the reaction chamber, and the whole BaF_2 detector array, and its relative placement. All regions outside these regions were considered vacuum. As the simulation proceeds, the energy and direction of the photon is tracked at each step in the cascade. If a photon never interacts with a non-vacuum region, it is assumed to escape.

The program was run until 1.5 million events occurred in the region of each crystal. This was repeated in 1 MeV steps from 1 MeV to 32 MeV, providing energy responses for the whole range given by the statistical model code CASCADE [56]. The energy deposited in each region was written to an event-by-event file for each energy step for subsequent analysis as data using the same code (LISA) used for the actual data analysis.

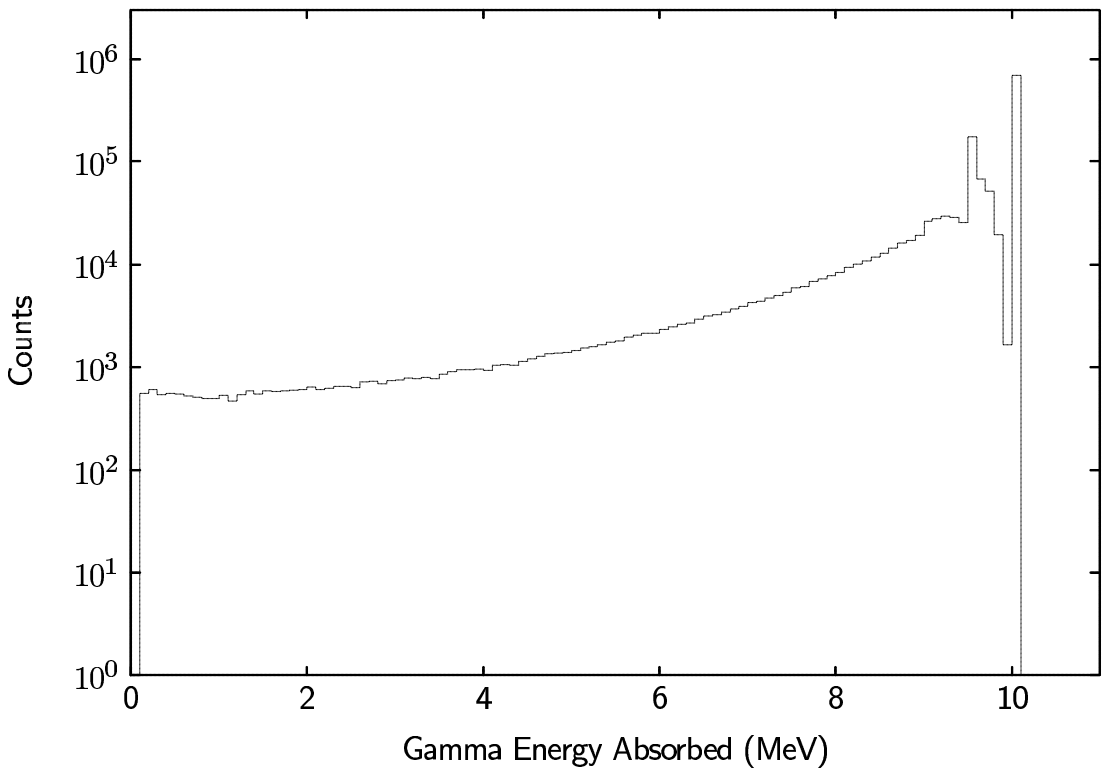

FIG. 27. Simulated BaF_2 crystal response to an incident 10 MeV γ ray.

Figure 27 shows a sample EGS simulation for a 10 MeV γ ray that has been analyzed with the shower reconstruction described above. Most of the energy (>50 %) is recovered with no leakage as is readily apparent from the largest peak at 10 MeV. Approximately ten percent is recovered in the first escape peak at 9.5 MeV, corresponding to the loss of one of the lepton-annihilation photons from pair-production. The second escape peak is barely visible as a bump around 9 MeV. At lower energies, the spectrum is a continuum. The intrinsic resolution of the detector is not taken into account. Otherwise the lines would not be so sharp. The simulated response of the BaF_2 regions were exported as 32-element arrays, using 1 MeV bins to match statistical model calculations.

Following Turmel, the model results were folded by the detector response using a fairly straightforward procedure [27]. First, the arrays were normalized by dividing the elements of a given array by the array's integrated value, generating probability distributions. These were then read into a two-dimensional array, EGS ($E_{\gamma_{out}}$, $E_{\gamma_{in}}$), where $E_{\gamma_{in}}$ is the energy of the initial photon and $E_{\gamma_{out}}$ is the contribution to the various energy bins. The predicted γ-ray cross section was then folded into the detector response as follows:

$$F(i) = \sum_{k=1}^{32} M_k \cdot EGS_{i,k} \tag{30}$$

where k is $E_{\gamma_{in}}$, i is $E_{\gamma_{out}}$, $F(i)$ is the folded statistical model prediction at energy i, M_k is the original model prediction and $EGS_{i,k}$ is the EGS array defined above.

An example of the results of this folding procedure can be seen in Figure 28 . The solid line shows a raw CASCADE prediction for the reaction 133 MeV ^{16}O + ^{208}Pb. The dashed line shows the prediction once the detector response from EGS has been factored in. While the overall shape of the spectrum does not change much over the whole range, the absolute magnitude is affected significantly (note that the plot is semi-log). The attenuated spectrum differs most at the highest photon energy, as one might expect. This trend is borne out by dividing the folded spectrum by the original to obtain the detector response as a function of energy over the range 1-32 MeV. This is shown in Figure 29. Aside from a peak centered at 9.5 MeV, there is generally less energy recovery in the BaF_2 detectors as the photon energy increases. Clearly, the procedure is quite necessary for an absolute comparison between experimental data and any model calculations.

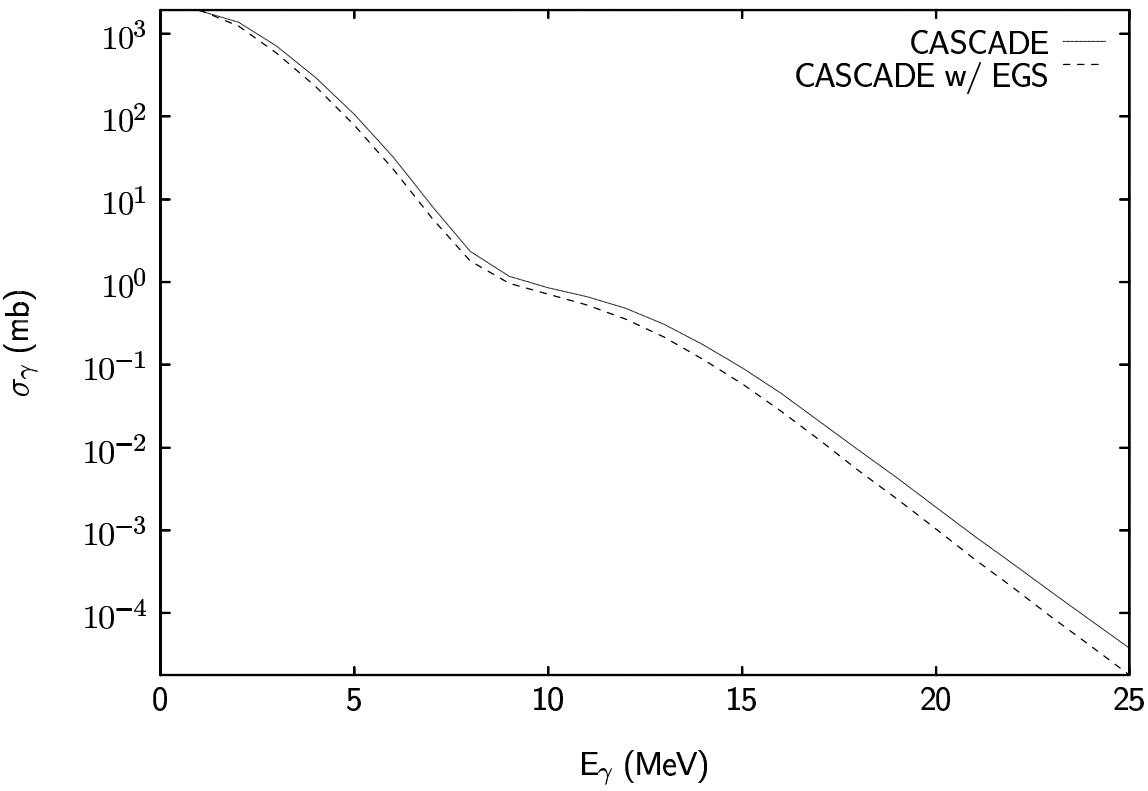

FIG. 28. The effect of folding the simulated detector response from EGS into a CASCADE prediction.

III.3 Neutron Analysis

The analyses of the fission and the γ-ray data were carried out at the Texas A&M Cyclotron Institute. In contrast, much of the neutron data was analyzed in Strasbourg. Of course, this analysis relied on an accurate definition of t_0 to give the neutron velocities and hence their energies. Thus the neutron data could not be fully analyzed until the fission analysis was complete. A rather abbreviated description of the analysis will be given here since similar procedures are very well documented in the literature (see Refs. [7–14]).

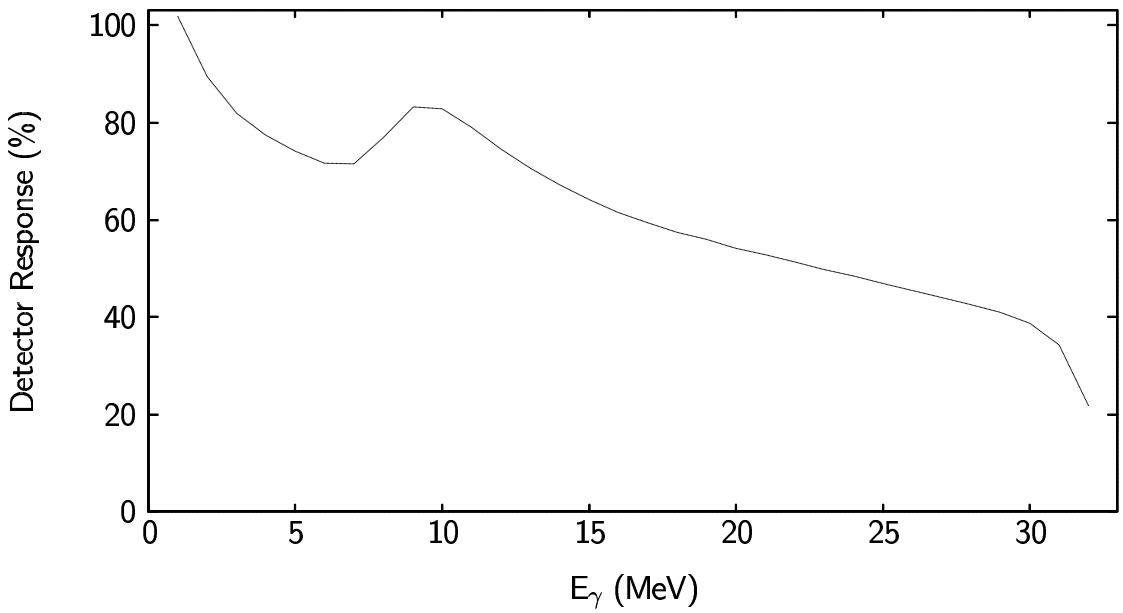

FIG. 29. Response function of the BaF_2 detectors, from the EGS simulation. Lines connecting the points are used to guide the eye.

In many respects, the DEMON detectors function like the BaF_2 counters. Both give fast and slow components to their energy response and both exhibit excellent timing characteristics. Although the fast-slow information proved to be useless in the γ-ray analysis due to long cable delays in the electronics, PSD was essential for the DEMON detectors to discriminate between neutrons and γ rays.

Figure 30 shows a log contour plot from one of the DEMON detectors during the $^{16}O + ^{208}Pb$ runs. The small islands of structure in the center of the figure are due to binning effects in the plotting routine rather than in the actual data. One can identify several components in the plot. The two intense diagonal lines toward the central portion of the figure indicate γ rays and neutrons. The lower-right ridge corresponds to γ rays while the upper ridge corresponds to neutrons. This is because

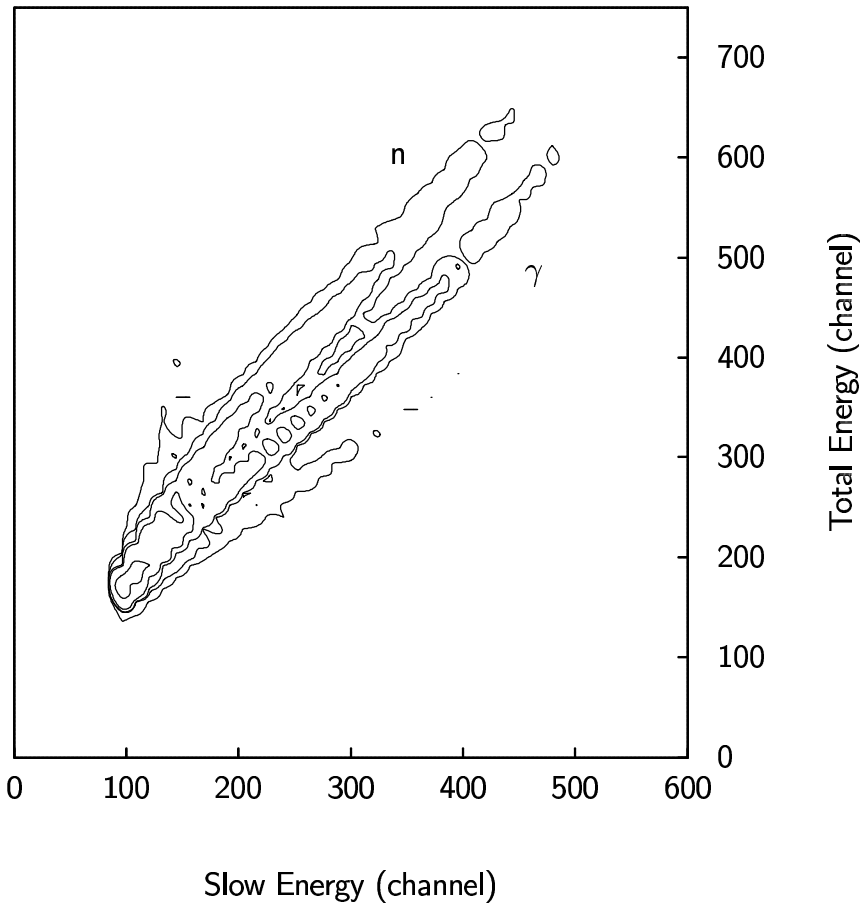

FIG. 30. Fast versus total energy plot for neutron detector $n4$.

neutrons have a larger slow component than γ rays. The weak lines in the plot are due to nuclear reactions in the scintillator [99, 100].

In Figure 31, energy and timing spectra are shown for a single detector during the $^{16}O + ^{208}Pb$ runs. The timing spectrum at the bottom includes the t_0 correction. The other two plots are uncalibrated energy spectra. All the spectra are for "good fission events." Several features are already apparent.

The timing spectrum shows the beam structure. The peaks in the spectrum occur approximately every 52.5 ns. This is expected from the beam frequency of 18.999 MHz. There is also a large prompt γ-ray peak visible at 55 ns with a very broad bump immediately after that. The latter is due to the neutrons. The latter are generally well separated from the γ rays. Energy spectra for the slow (top) and total (middle) are also illustrated in Figure 31. Both spectra have similar shapes, but the spectrum for the slow component lacks the pedestal seen in the total component.

Once the above steps have been completed, ν_{pre} and ν_{post} were determined using moving-source fits. The exact steps have been discussed many times in the literature [7-14, 41, 42, 58–60, 116, 117, 61, 118, 119]. Sample fits will be presented in the next chapter. Of course, the neutron energy spectra are derived from TOF rather than pulse height.

To generate neutron energy spectra, timing gates were set around the neutron bump seen in the lowest plot in Figure 31. Gates were also set around the neutron region in the two-dimensional slow-total plots.

Before proceeding, it is imperative to know the efficiency of the DEMON detectors so that accurate angular distributions and multiplicities can be generated.

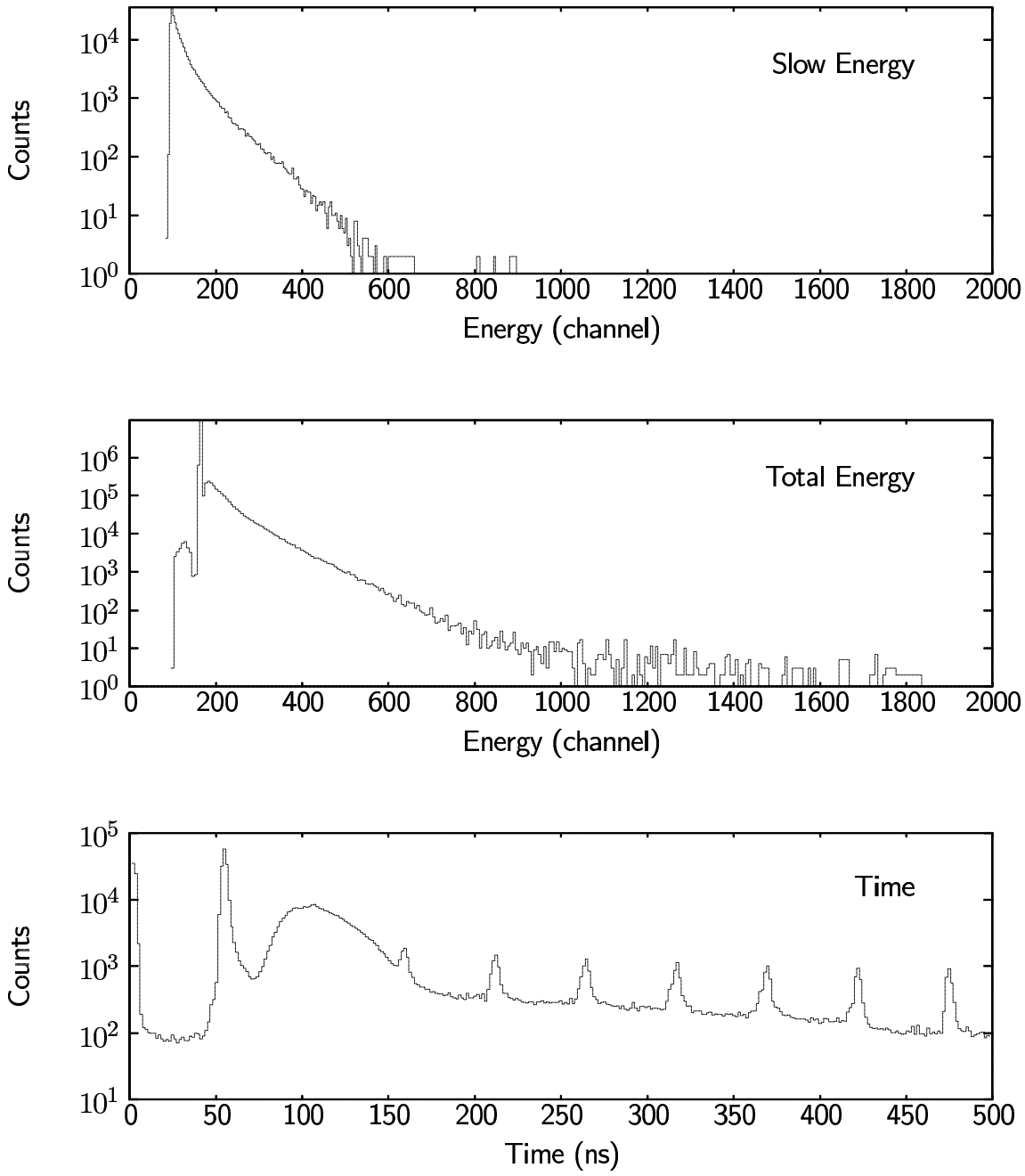

FIG. 31. Results of the analysis of detector $n5$. The top plot is the only for the slow energy response, the middle plot shows the spectrum for the total energy signal, and the bottom plot shows the timing signal from the detector.

Previously, numerous measurements have been made with the DEMON detectors with energies ranging from tens of MeV [100, 120] to hundreds of MeV [120, 121]. These data were then compared to various Monte Carlo calculations simulating neutron detection in the scintillator NE213 [122]. The results supply the needed information for detector simulations. Following the work Donadille *et al.* [103], a simulation code MENATE [104] was adapted and applied to this problem. The code MENATE is analogous to EGS. MENATE calculates the experimental response of NE213 to neutrons or γ rays with energy lower than 100 MeV in detectors of cylindrical geometry. The code includes various interactions due to the photoelectric effect, Compton scattering, and pair production. The exact geometry of the detectors is also in the code. Crosstalk between detectors is also accounted for.

The code was run for a variety of energies for incident photons and neutrons. Response functions such as those for the BaF_2 detectors were generated. These were folded into all subsequent calculations in much the same manner as described above for the BaF_2 detector response. A schematic flowchart for the overall procedure is shown in Figure 32 below.

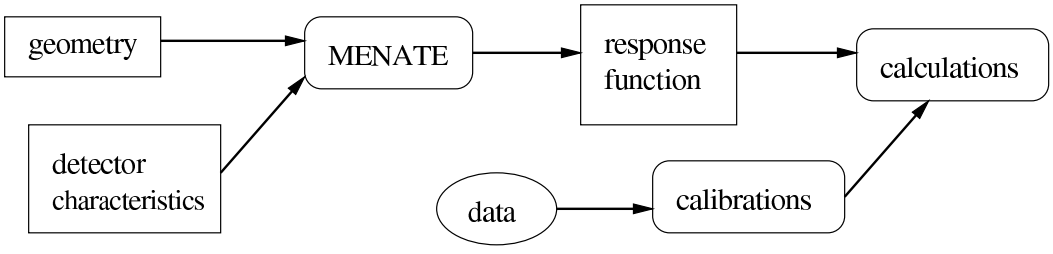

FIG. 32. Flowchart outlining the various steps taken in the neutron analysis.

CHAPTER IV

RESULTS

The previous two chapters have focussed on various aspects of the setup and the data analysis. A few results have been presented as illustrations, however the results have not yet been discussed *in toto*. This chapter will present the final results for these fission studies, using the fission fragment data, the neutron data, and the GDR γ-ray data. The qualitative aspects of the data will be stressed. The first subsection will deal with the fission data itself. The GDR γ-ray energy spectra will then be presented. Finally, the neutron energy spectra and multiplicities will be presented and discussed. In the following chapter, the data will be compared to statistical model calculations.

IV.1 Fission Results

The analysis of the system 133 MeV $^{16}O + ^{208}Pb$ was relatively straightforward due to the strong dominance of the fission exit channel relative to evaporation residue production. The reconstructed masses and their distribution widths were in reasonable agreement with systematics. The mass and the TKE spectra for this system were previously shown in Figures 17 and 18, respectively. The mass cuts are visible in the former figure. These gates were chosen so that each asymmetry cut would have comparable statistics.

The $^{16}O + ^{176}Yb$ system was similarly straightforward to analyze though there were far less statistics to work with. The fragment mass distribution is presented in

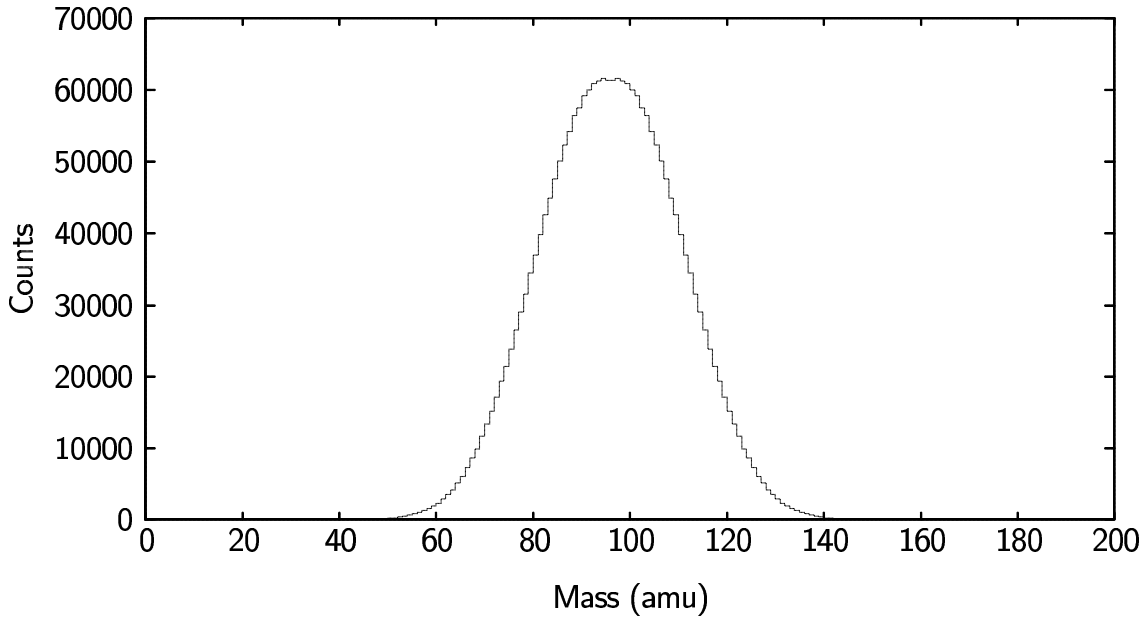

FIG. 33. Final mass distribution for the $^{16}O + ^{176}Yb$ data.

TABLE 10. Mass cuts used in the $^{16}O + ^{176}Yb$ γ-ray analysis.

Cut	Range (amu)
Symmetric	$90 \leq A \leq 102$
Asym1	$82 \leq A < 90$, $102 < A \leq 110$
Asym2	$40 \leq A < 82$, $110 < A \leq 151$

Figure 33. The mass distribution is very clean and exhibits the typical Gaussian shape centered about symmetric fission. The effect of mass asymmetry on the γ-ray energy spectrum was also investigated, but due to the poor statistics relative to the $^{16}O + ^{208}Pb$ and $^{4}He + ^{209}Bi$ cases only three mass ranges were possible. Table 10 lists the cutoffs for the three mass cuts. The TKE distribution is shown in Figure 34. Again,

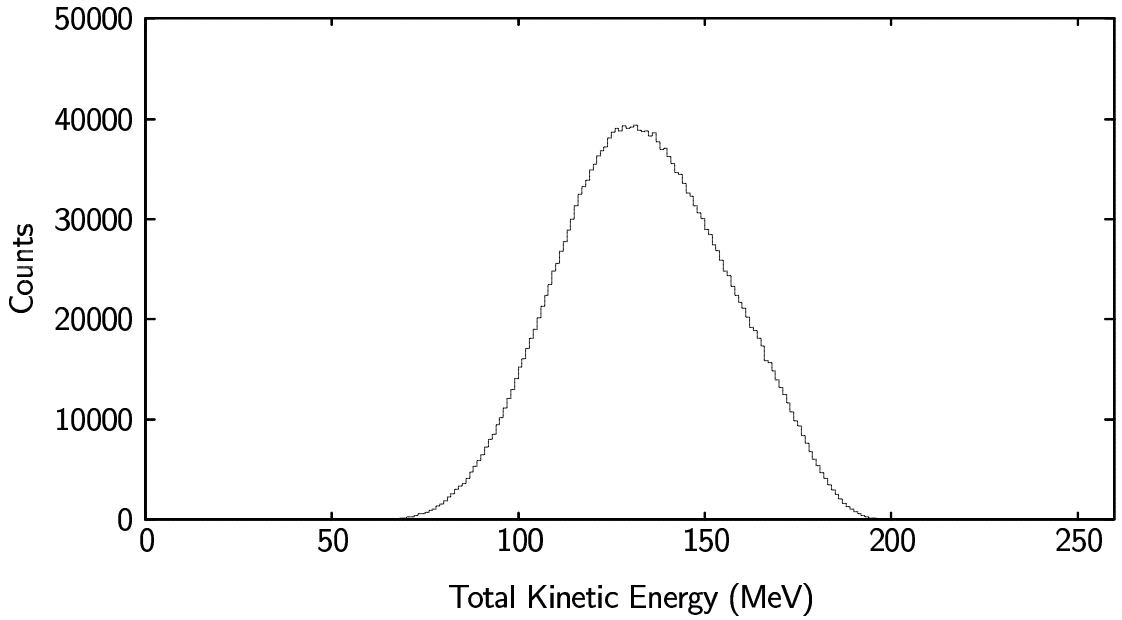

FIG. 34. Final total kinetic energy distribution for the $^{16}O + ^{176}Yb$ runs.

the distribution is largely as expected, aside from a minor high-energy deviation noted in Section III.1. This is seen for all of the TKE results.

For the 104 MeV $^{4}He + ^{209}Bi$ system, there was added difficulty due to the lower fission cross section and the lower fission fragment energies. Because of the lower TKE, this required additional iterations to generate the mass and the energy distributions. The PPAC analysis was complicated since a significant fraction of the fragment energies were lost in the various detector windows. Figure 35 shows the resultant mass distribution. The yield is relatively flat in the central portion of the distribution. This could be due to the difficulties presented by the lower TKE of the fragments and a slight wandering in the beam position. It is also possible that there is some contribution from fission following incomplete fusion [6, 112]. However, gates

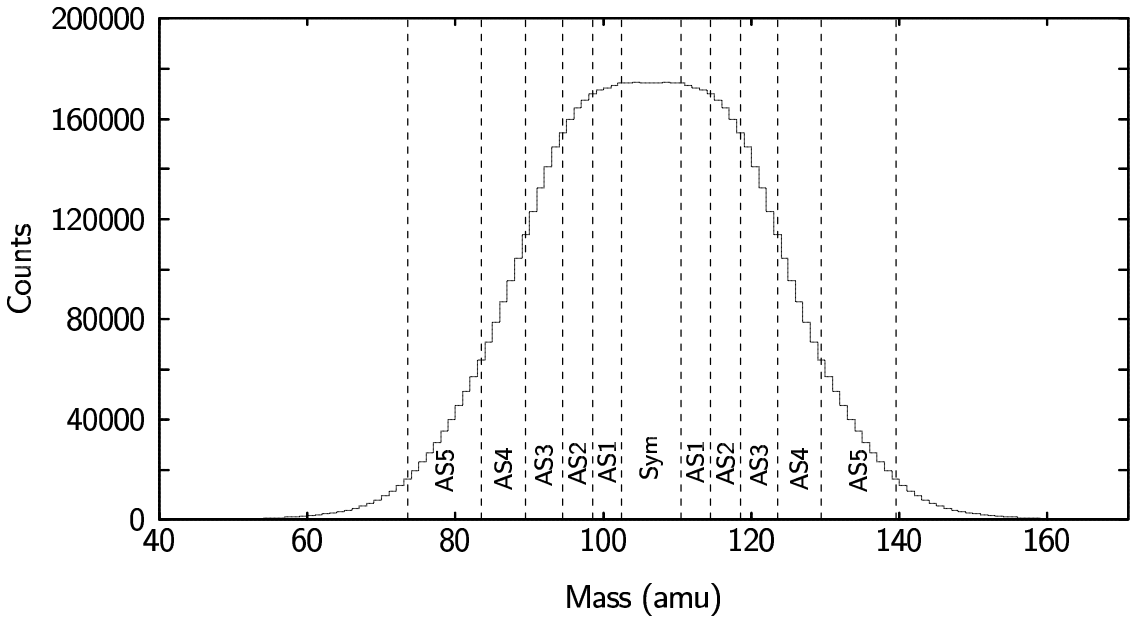

FIG. 35. Final mass distribution for the ^{4}He + ^{209}Bi runs, including mass asymmetry cuts used in the γ-ray analysis.

have been placed on the folding angle to eliminate most of the contributions from incomplete fusion. Moreover, the TKE distribution shown in Figure 36 appears quite normal. As in the case of the ^{16}O + ^{208}Pb data, adequate statistics were obtained to set several mass gates for the γ-ray analysis. The asymmetry ranges are summarized in Table 11. Note that the flat part of the mass distribution is mainly associated with the symmetric cut.

The ^{4}He + ^{188}Os system proved more difficult to analyze than the ^{4}He + ^{209}Bi system because the measurements yielded two orders of magnitude less data. Due to such low statistics, a fission analysis was possible, but analysis of the γ-ray results proved to be inadequate for any time scale determination, let alone investigation of mass asymmetry or TKE dependence. The mass and TKE distributions are presented

TABLE 11. Mass cuts used in the ^{4}He + ^{209}Bi γ-ray analysis.

Cut	Range (amu)
Symmetric	$102.5 \leq A \leq 110.5$
Asym1	$98.5 \leq A < 102.5$, $110.5 < A \leq 114.5$
Asym2	$94.5 \leq A < 98.5$, $114.5 < A \leq 118.5$
Asym3	$89.5 \leq A < 94.5$, $118.5 < A \leq 123.5$
Asym4	$83.5 \leq A < 89.5$, $123.5 < A \leq 129.5$
Asym5	$73.5 \leq A < 83.5$, $129.5 < A \leq 139.5$
Asym6	$33.5 \leq A < 73.5$, $139.5 < A \leq 179.5$

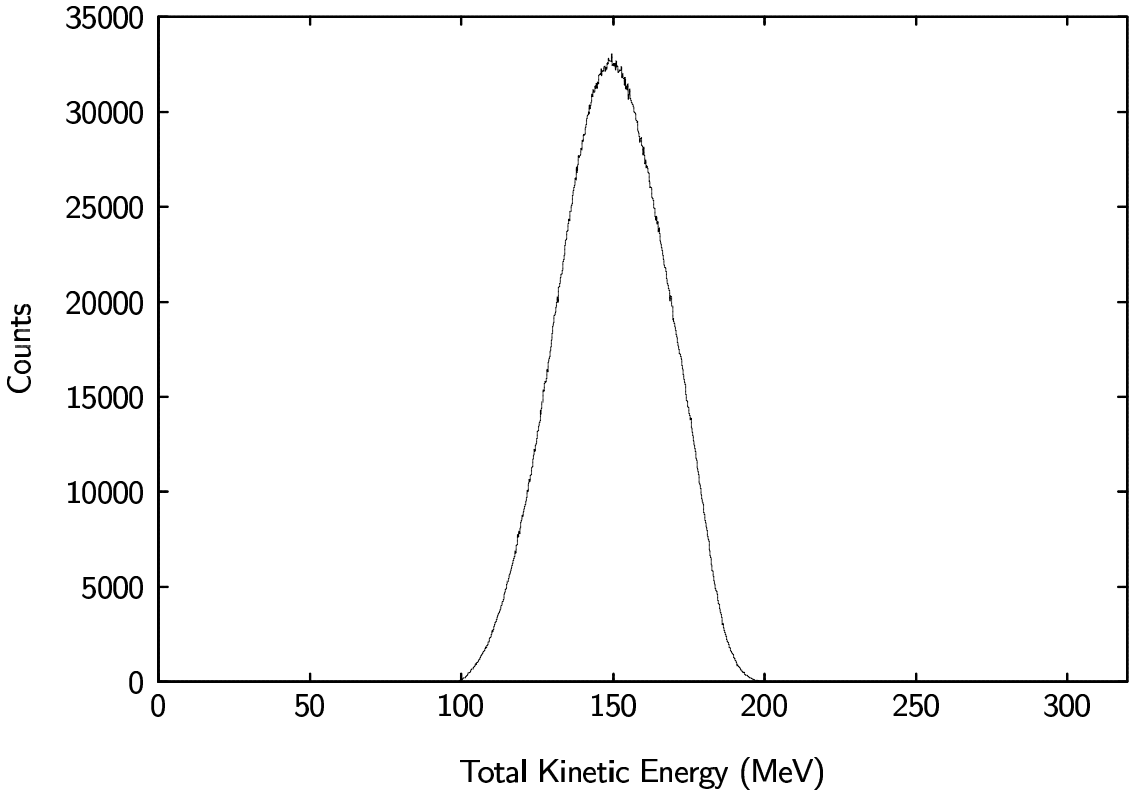

FIG. 36. Final TKE distribution for all ^{4}He + ^{209}Bi runs.

in Figure 37. There is essentially a Gaussian centered at symmetric fission. As noted above, there is a slight high-energy tail in the TKE distribution.

Table 12 summarizes the fission fragment characteristics for each reaction. Ranges are given as $\pm 1\ \sigma$. Corrections to t_0 are also listed. The systems with the lowest statistics were also run for the shortest amount of time, somewhat offsetting effects such as the instability of the beam.

IV.2 GDR γ-ray Results

In the previous chapter, the results of background (i.e. random coincidences as well as true background) subtraction on the total γ-ray energy spectrum were shown for $^{16}O + {}^{208}Pb$. Similar results are shown in Figures 38 and 39 for the $^{4}He + {}^{209}Bi$ and $^{16}O + {}^{176}Yb$ reactions, respectively. Note that the relative importance of these corrections increases with the decreasing fissility of the compound system. All of the background spectra show a bump centered about 6 MeV. This is due to capture of γ rays associated with neutron capture in the material surrounding the chamber. While this capture bump has little influence on the final spectrum above about 12 MeV, it does affect the data in the lower energy portion of the GDR region, stressing the importance of these background corrections.

For the $^{4}He + {}^{188}Os$ runs, the results of background subtraction are shown in Figure 40. The statistics in this case are more than two orders of magnitude lower than for the $^{4}He + {}^{209}Bi$ case. Therefore, only the statistical region is clearly identifiable. There appear to be a few counts in the GDR region, as well as perhaps some enhancement in the statistical region. Clearly though, such conclusions are

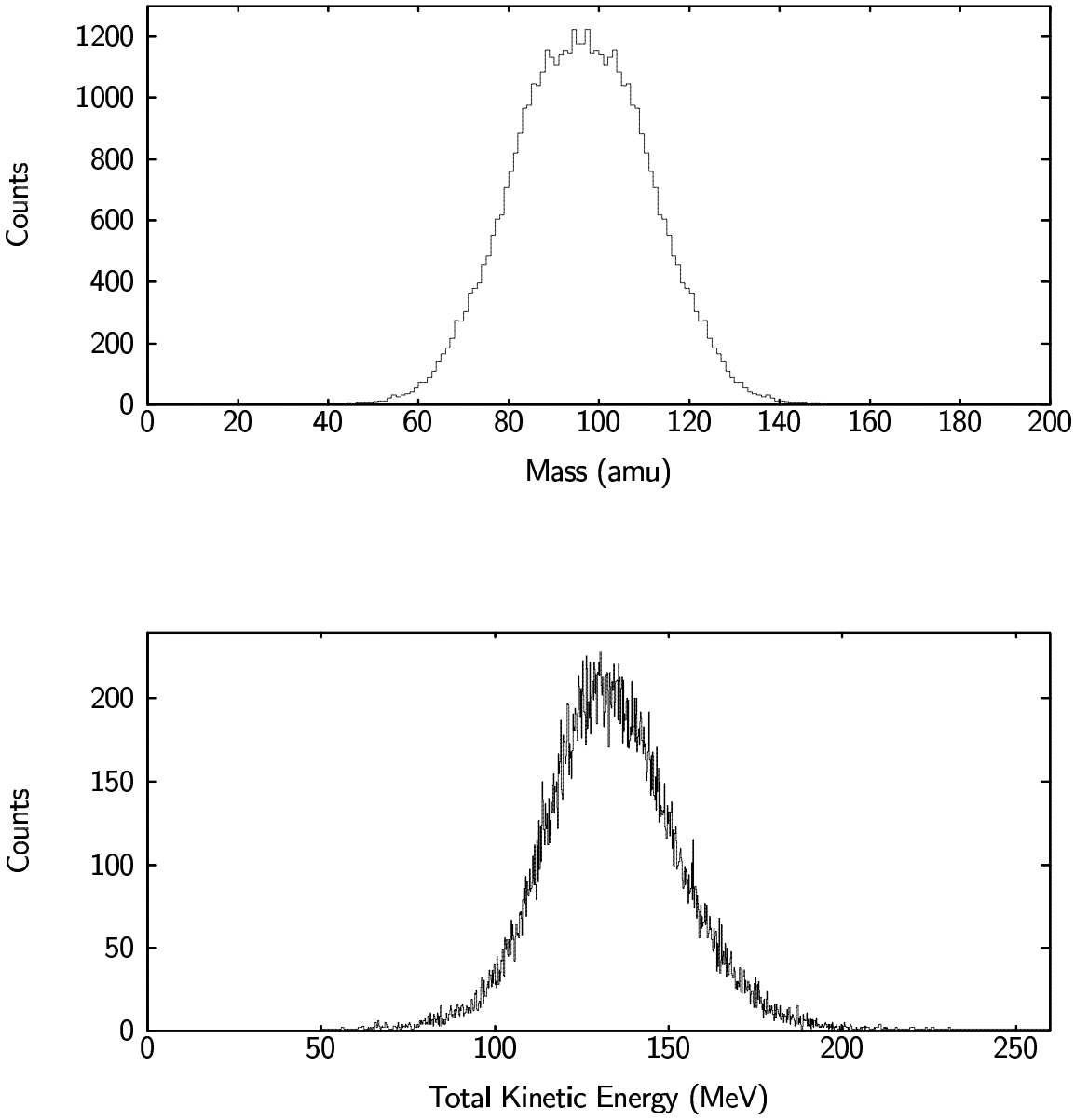

FIG. 37. Mass (top) and TKE (bottom) distributions resulting from the PPAC analysis of the ^{4}He + ^{188}Os runs.

TABLE 12. Fission fragment characteristics for each reaction studied.

Reaction	Events	$\langle$Mass$\rangle$ (amu)	$\langle$TKE$\rangle$ (MeV)	$\langle\Theta_{fold}\rangle$ (degrees)	$\langle t_0\rangle$ Offset (ns)
$^{16}O + ^{208}Pb$	10.867 M	112 $\pm$17	163.2$\pm$25.0	180.4$\pm$4.6	2.80$\pm$0.73
$^{4}He + ^{209}Bi$	7.411 M	106.5$\pm$14	149.7$\pm$16.9	180.2$\pm$3.7	2.72$\pm$0.57
$^{16}O + ^{176}Yb$	2.300 M	96 $\pm$14	133.0$\pm$22.0	180.4$\pm$4.1	2.73$\pm$0.65
$^{4}He + ^{188}Os$	0.047 M	96 $\pm$15	133.7$\pm$19.5	180.1$\pm$3.4	2.80$\pm$0.63

subjective given the statistics and the associated uncertainties. Certainly there is not enough of a GDR enhancement to fit with CASCADE calculations and extract a fission time scale.

A comparison of the final total γ-ray yield of each of the reactions with reasonable statistics (i.e. all but $^{4}He + ^{188}Os$) is given in Figure 41. Below about 7 MeV, the spectra are nearly exponential as expected from statistical γ-ray emission. A closer examination shows that the low energy component is not a pure exponential (see below).

Above the statistical region, the spectra show a marked deviation from an exponential. This is due to GDR γ-ray emission from both the compound nucleus and the fragments. The differences in GDR contributions are readily apparent in this figure. The heavier systems exhibit greater GDR γ-ray strength. This could be due to the fact that the heavier systems have lower energies for the GDR, making γ-ray emission more probable.

Because of the relatively good statistics obtained for the $^{16}O + ^{208}Pb$ and $^{4}He + ^{209}Bi$ systems, it was possible to examine the effects of the mass asymmetry and

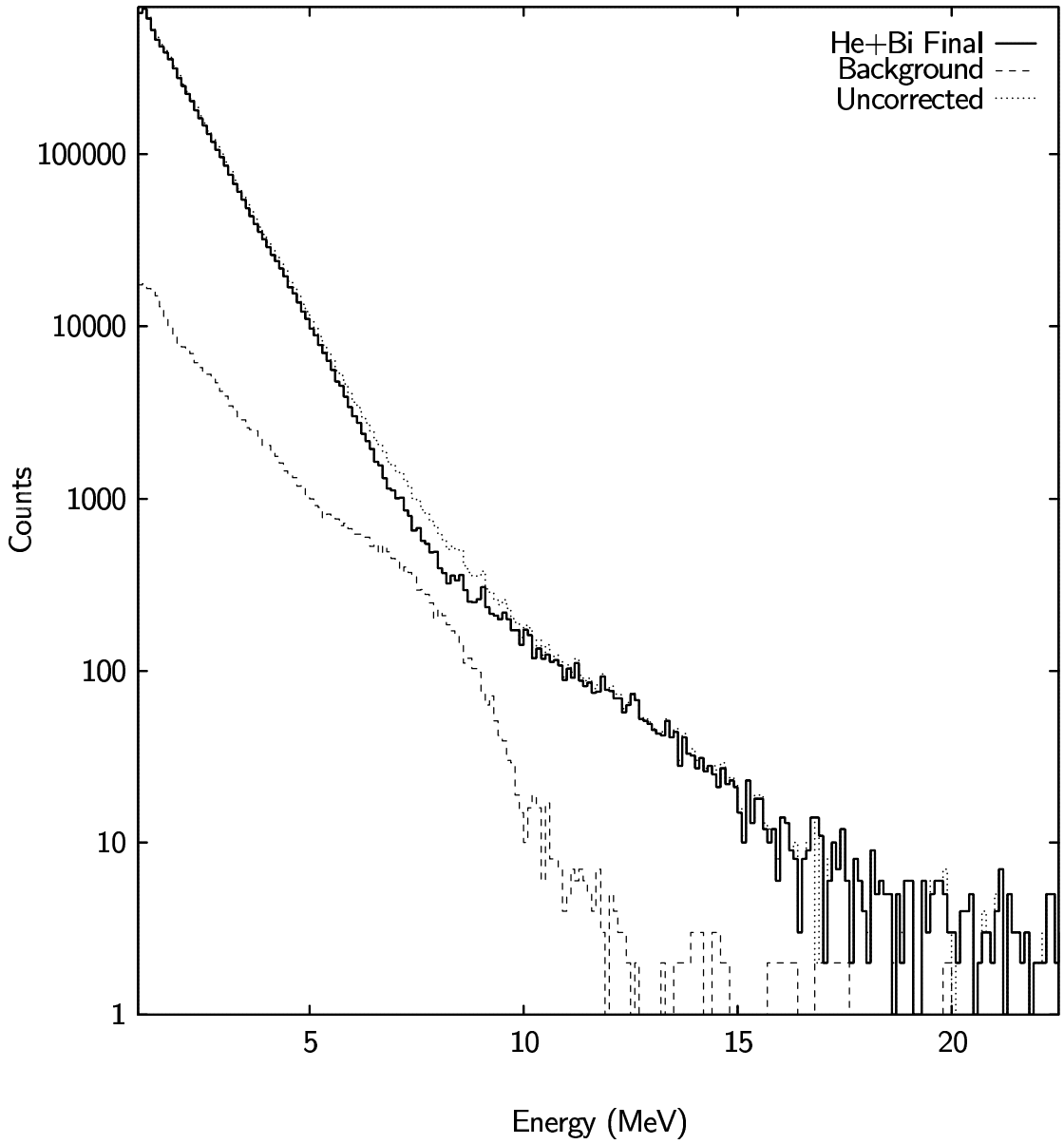

FIG. 38. Final results of all gates and background subtraction for the total γ-ray spectrum for ^{4}He + ^{209}Bi.

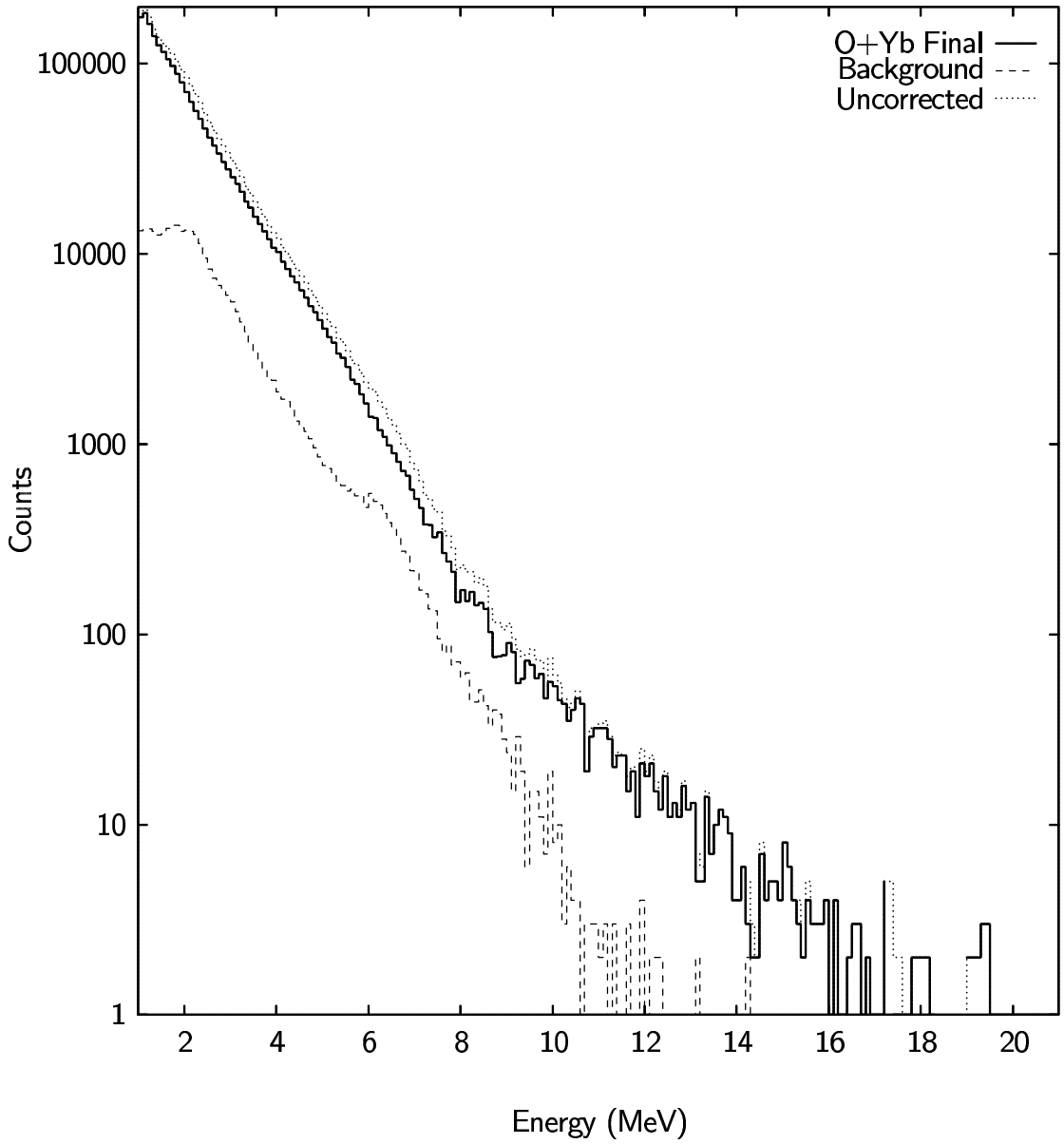

FIG. 39. Final results of all gates and background subtraction for the total γ-ray spectrum in the $^{16}O + ^{176}Yb$ runs.

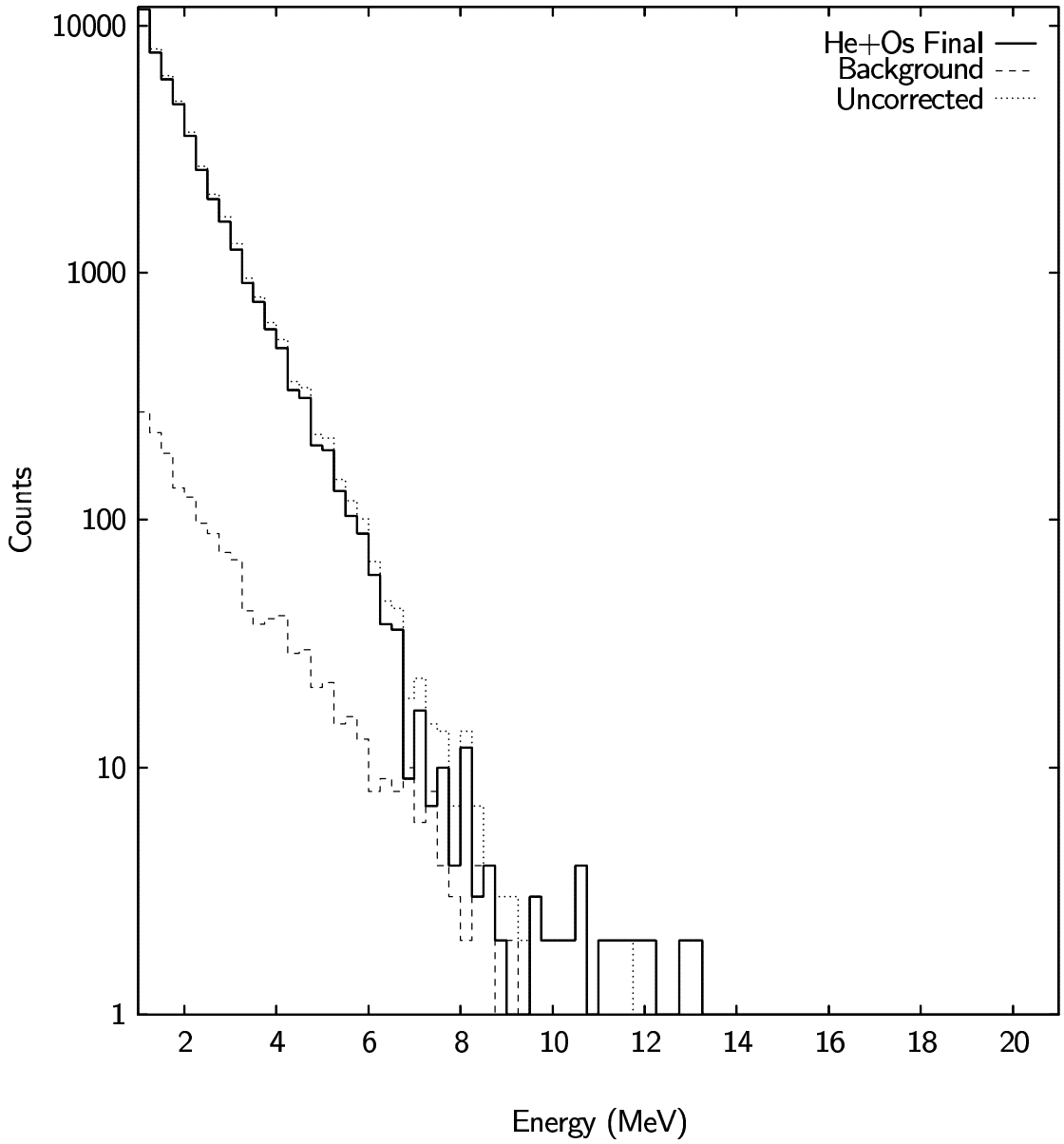

FIG. 40. Final results of all gates and background subtraction for the total γ-ray spectrum for the ^{4}He + ^{188}Os runs.

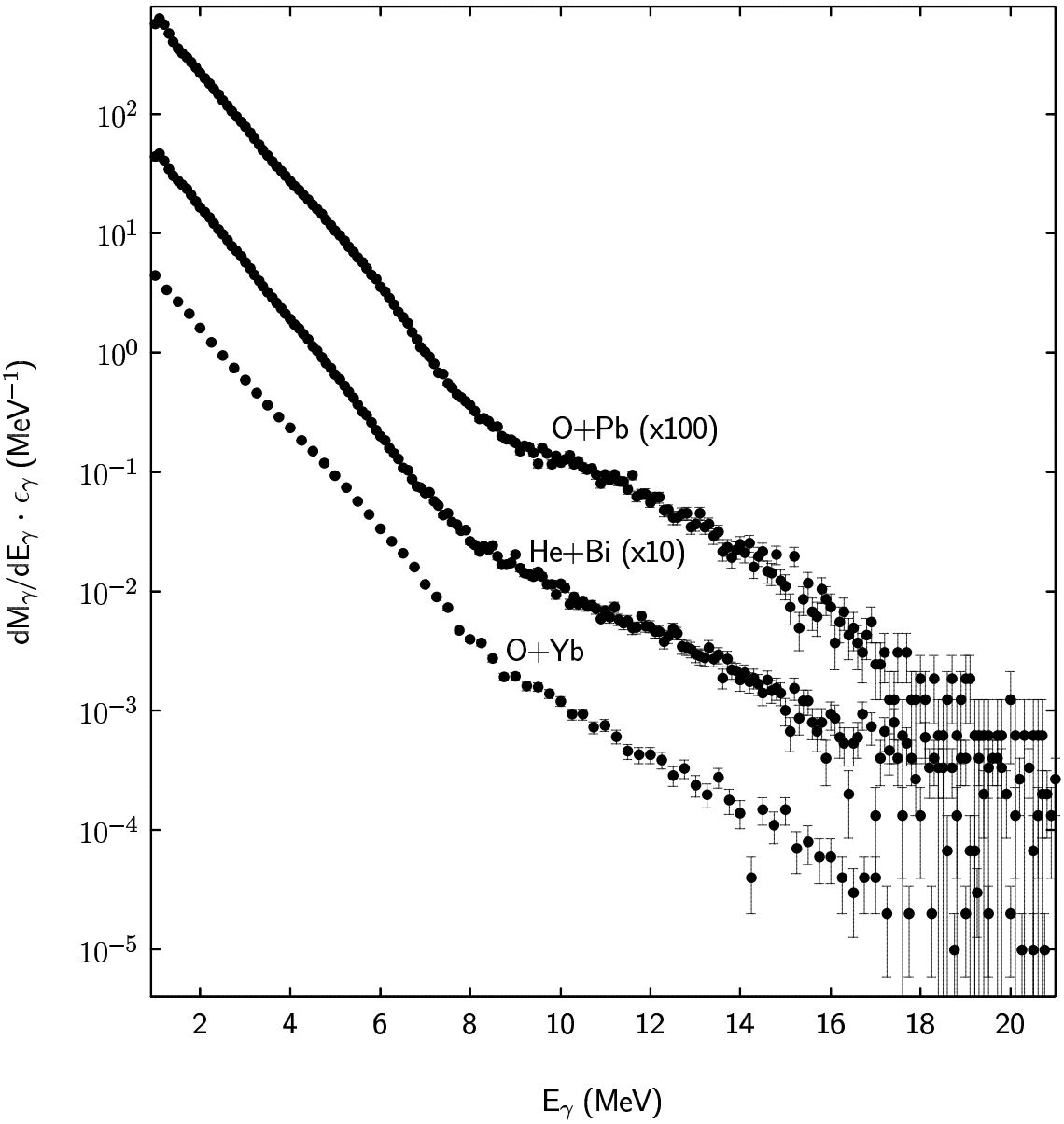

FIG. 41. Total absolute fission γ-ray multiplicity (M_γ) for each of the reactions studied. The topmost curve corresponds to $^{16}O + ^{208}Pb$, increased by a factor of 100. The central curve represents $^{4}He + ^{209}Bi$, $\times 10$. The bottom curve is the M_γ spectrum for $^{16}O + ^{176}Yb$.

the TKE on the total γ-ray energy spectrum. The mass cuts investigated for the ^{16}O + ^{208}Pb case were listed in Table 9 and shown previously in Figure 17 in Chapter III. Note that there are six major regions. The symmetric mass cut is centered about the mean value of A=112 for the fission fragments. The effects of the various mass gates to the gamma spectrum can be seen in Figure 42. The spectra are shifted on the vertical axis as indicated in the figure, with the more symmetric mass cuts towards the top. The statistics are similar in each case.

While the GDR portions of the spectra are similar, there is a noticeable enhancement in the statistical region (4–8 MeV) with increasing asymmetry. This phenomenon has been seen previously [114], and has recently been examined quite extensively in gamma decay associated with fission of heavy systems [29, 123, 124, 125]. The enhancement has been shown to exhibit a strong fragment mass dependence. In the case of spontaneous fission of ^{252}Cf, α-coincidence methods were used in association with measuring fragment masses and γ-ray energies. Singer *et al.* were able to show that the increased number of 4–8 MeV γ rays originated from fragments with A and Z near the doubly-magic proton and neutron numbers of 50 and 82, respectively [125]. For cuts well removed from magic numbers, the spectra are essentially exponential up to the GDR bump. Nevertheless, the existence of this enhancement shows that one cannot always rely on an exponential dependence of the γ-ray spectra in the statistical energy region.

For ^{16}O + ^{176}Yb, the mass asymmetry dependence of the γ-ray energy spectrum was also investigated. However, due to the relatively poorer statistics, only three mass

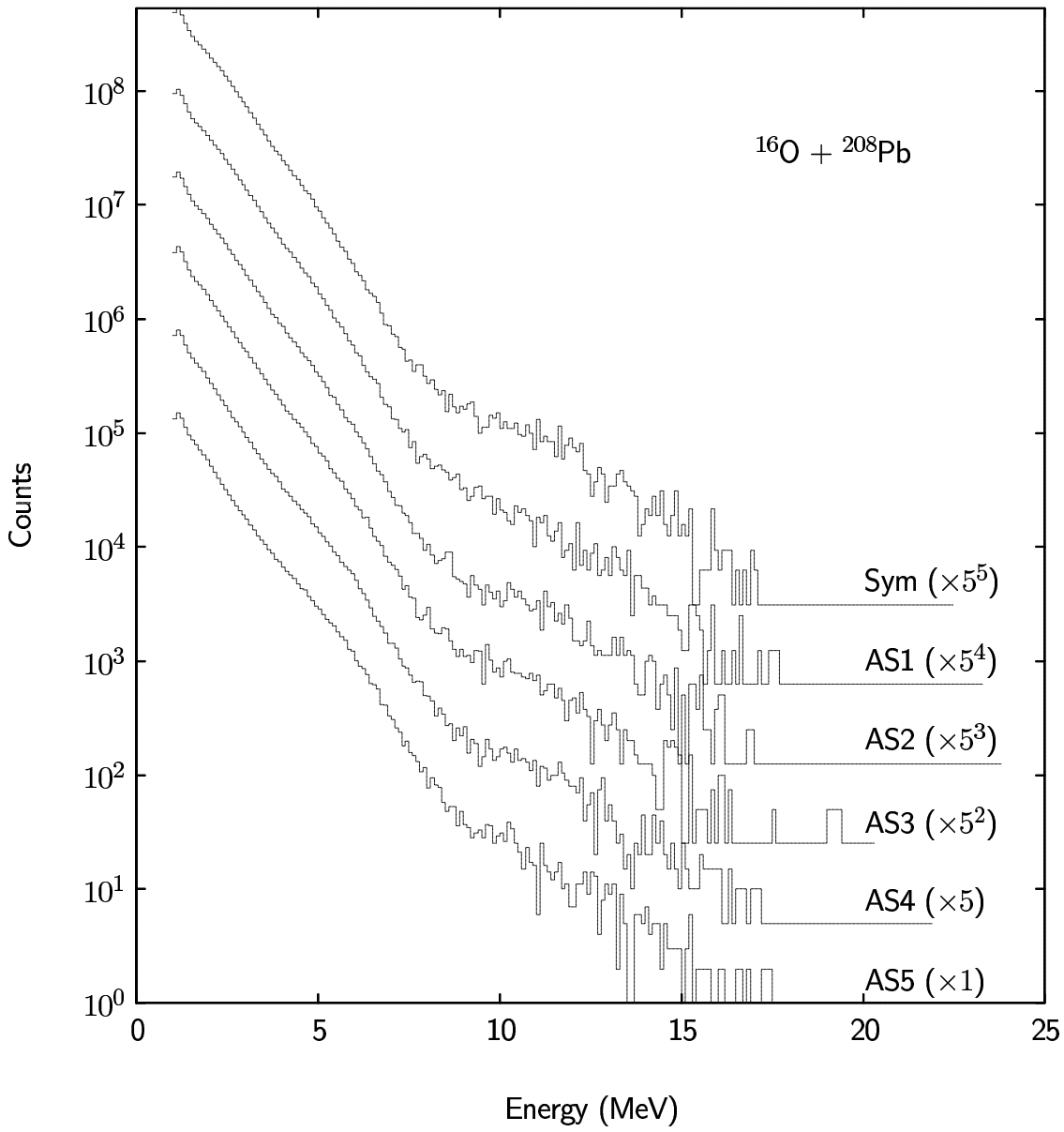

FIG. 42. Effects of different mass asymmetries on the γ-ray energy for $^{16}O + ^{208}Pb$.

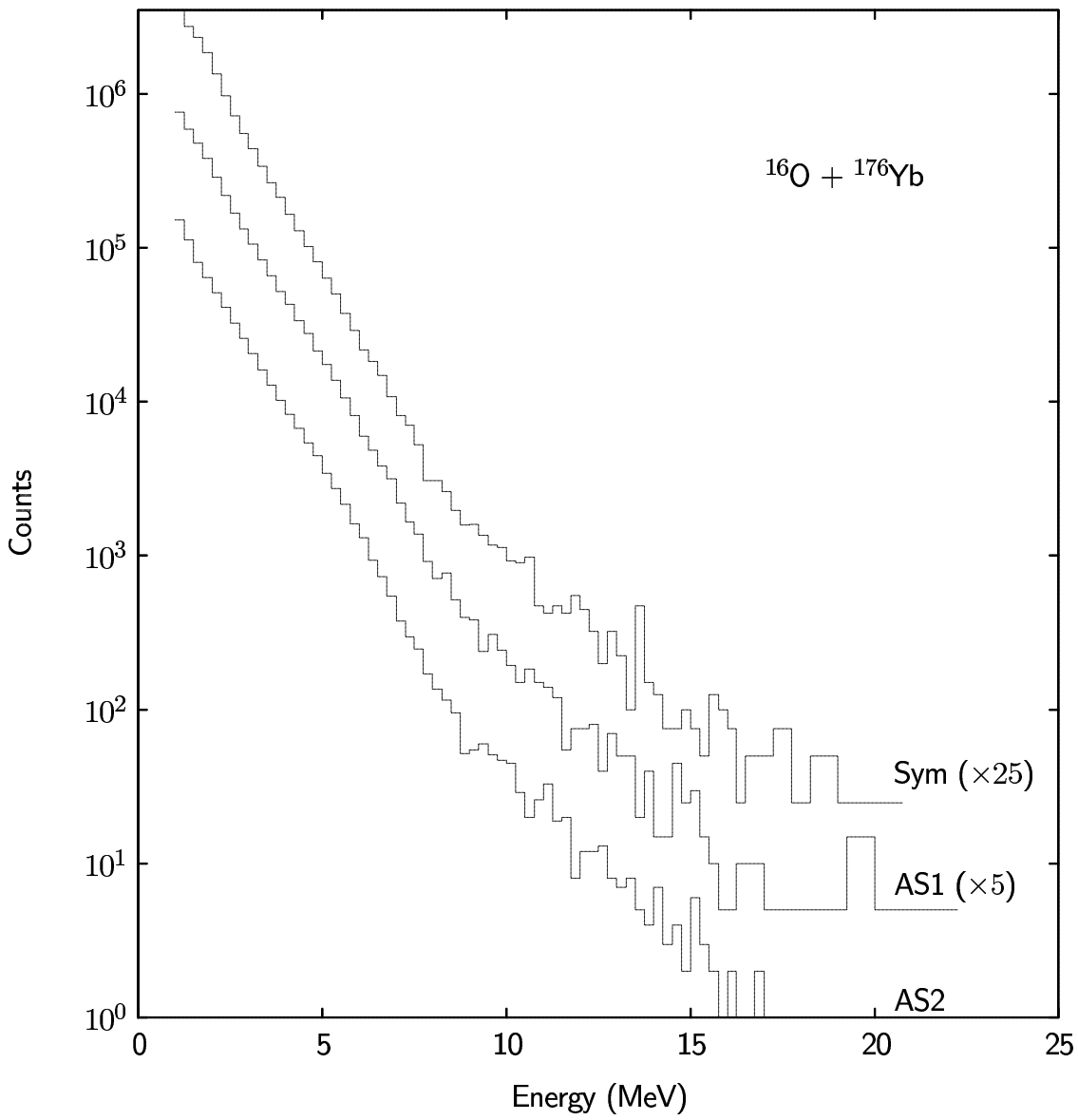

FIG. 43. Mass asymmetry dependence of the $^{16}O + ^{176}Yb$ γ-ray energy spectrum.

ranges were chosen. Larger energy bins (250 keV, instead of 100keV) were also used. The results of these cuts are presented in Figure 43. As before, the most symmetric fissions are represented by the uppermost spectrum, with increasing asymmetry in the lower spectra. Again, more asymmetric mass cuts exhibit an enhancement in the

statistical region. The most asymmetric cut also includes the Z=50 and N=82 shell closures, and is in agreement with the observations for the ^{16}O + ^{208}Pb and ^{4}He + ^{209}Bi systems. Again, there is no statistically significant difference in the GDR region. The lowest-statistics run, ^{4}He + ^{188}Os was the only one which did not provide enough data to allow investigation of mass asymmetry effects.

In nearly all previous GDR-based fission time scale studies involving systems heavy enough to produce fragments with mass ≈132, the statistical enhancement was not taken into account [23–26, 28, 30–32, 34, 79, 126, 127]. The γ-ray data in these studies simply did not extend to energies low enough to reveal the enhancement in the high-energy statistical region. Typically, the γ-ray data were only used above 5–6 MeV, masking the high-energy statistical γ-ray enhancement. In those cases where γ-ray energies are investigated using a lower threshold, the enhancement was ignored or not recognized [26, 30, 32]. This simple oversight effectively makes previous time scale measurements somewhat suspect for systems with significant production of magic or doubly-magic fragments. In previous works that relied on fitting the γ-ray spectra, the statistical region for such systems would change the GDR γ-ray contribution.

The extent of the enhancement is more clearly visualized via exponential fits to the statistical region. Figure 44 shows the final γ-ray spectrum for the ^{16}O + ^{208}Pb runs with two exponential fits to the statistical background. The fit indicated by the solid line is fitted at 2.5 and 7.5 MeV, while the dashed line is fit at 4.5 and 7.5 MeV. The enhancement at the high end, just below the GDR region, is clearly visible. This

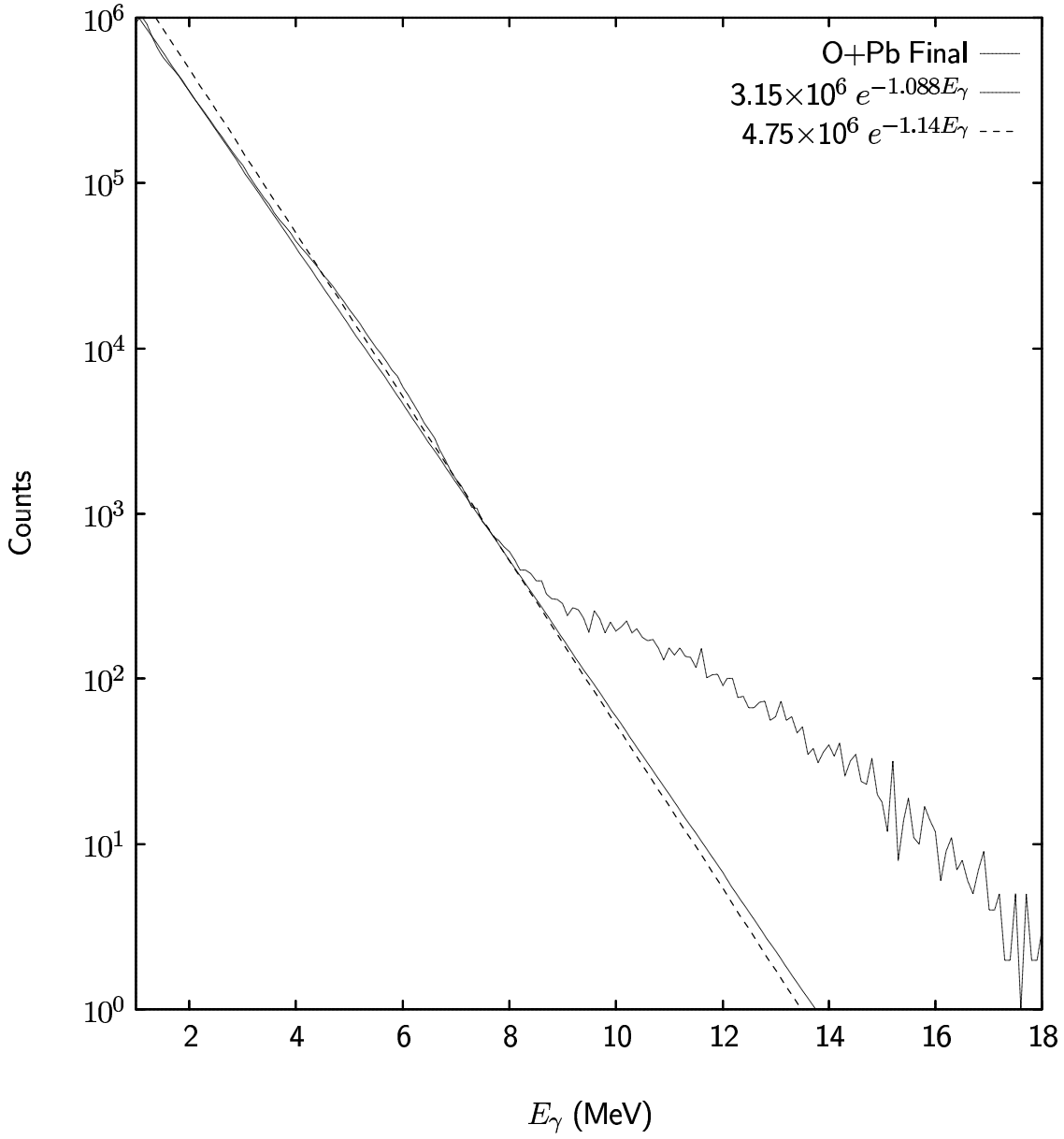

FIG. 44. Effect of fitting an exponential to the statistical γ-ray region for ^{16}O + ^{208}Pb.

TABLE 13. Four TKE ranges investigated for $^{16}O + ^{208}Pb$.

Cut	Range (MeV)
TK1	$80.0 \leq E < 141.9$
TK2	$141.9 \leq E < 161.9$
TK3	$161.9 \leq E < 181.9$
TK4	$181.9 \leq E < 240.0$

enhancement is present for all four systems studied, though it is less apparent with decreasing mass of the compound nucleus. In the lower-mass systems, doubly-magic fragments are less likely to be produced.

The statistical enhancement is broad and carries over somewhat into the GDR region, producing an optical illusion suggesting that there might be some differences in the GDR region with different mass asymmetries. However, upon overlaying the gated spectra, there is no apparent difference for these mass cuts within statistical uncertainty. With higher statistics there may well be a mass-asymmetry effect in this region, though this is unsupported by the current data.

The effect of gating on different portions of the TKE distribution was also examined. Four cuts on TKE were set on two-dimensional plots of mass and TKE. For the $^{16}O + ^{208}Pb$ case, these simple cuts are given in Table 13. Application of these gates to the overall γ-ray spectrum yields the results in Figure 45. The spectra are shown with highest TKE cuts uppermost in the figure. There is no clear effect upon the γ-ray spectra, either in the GDR region or elsewhere. In fact, upon overlay of these spectra, there is no discernible difference at all within statistical uncertainty.

This is in keeping with previous observations of a relatively flat TKE dependence upon the γ-ray spectrum of fissioning systems [128]. The lack of a TKE dependence seems surprising at first since the yield of GDR γ rays may be expected to be related to the excitation energy. One might expect that

$$Y_{GDR} \propto \rho(E^*_{CN} - TKE), \tag{31}$$

where the argument of ρ represents the energy available around the saddle. The lack of a TKE dependence suggests that the yield of GDR γ rays is determined at earlier stages in the evolution of the system with deformation.

Possible mass and TKE dependences were also investigated for the ^{4}He + ^{209}Bi runs. The asymmetry cuts used were previously shown in Figure 35 and listed in Table 11. Application of these cuts to the total ^{4}He + ^{209}Bi γ-ray spectrum yielded the results presented in Figure 46. As before, γ-ray spectra corresponding to the more symmetric mass cuts are shown at the top of this figure.

Again, one observes an enhancement in the statistical region with increasing mass asymmetry, though not as much as in the ^{16}O + ^{208}Pb case. This is easily understood. The shell closures at Z=50 and N=82 are further away from symmetric fission for this lighter system. Thus, the relative abundance of fragments near those shell closures is far less than for the ^{16}O + ^{208}Pb system.

Investigation of possible TKE dependence of the fragments upon the total γ-ray spectrum yielded similar null results as for ^{16}O + ^{208}Pb. Again, four simple cuts were utilized. These are listed in Table 14. Applying these cuts gave the spectra shown in Figure 47. As before, the spectra are shown with the higher TKE cuts uppermost in

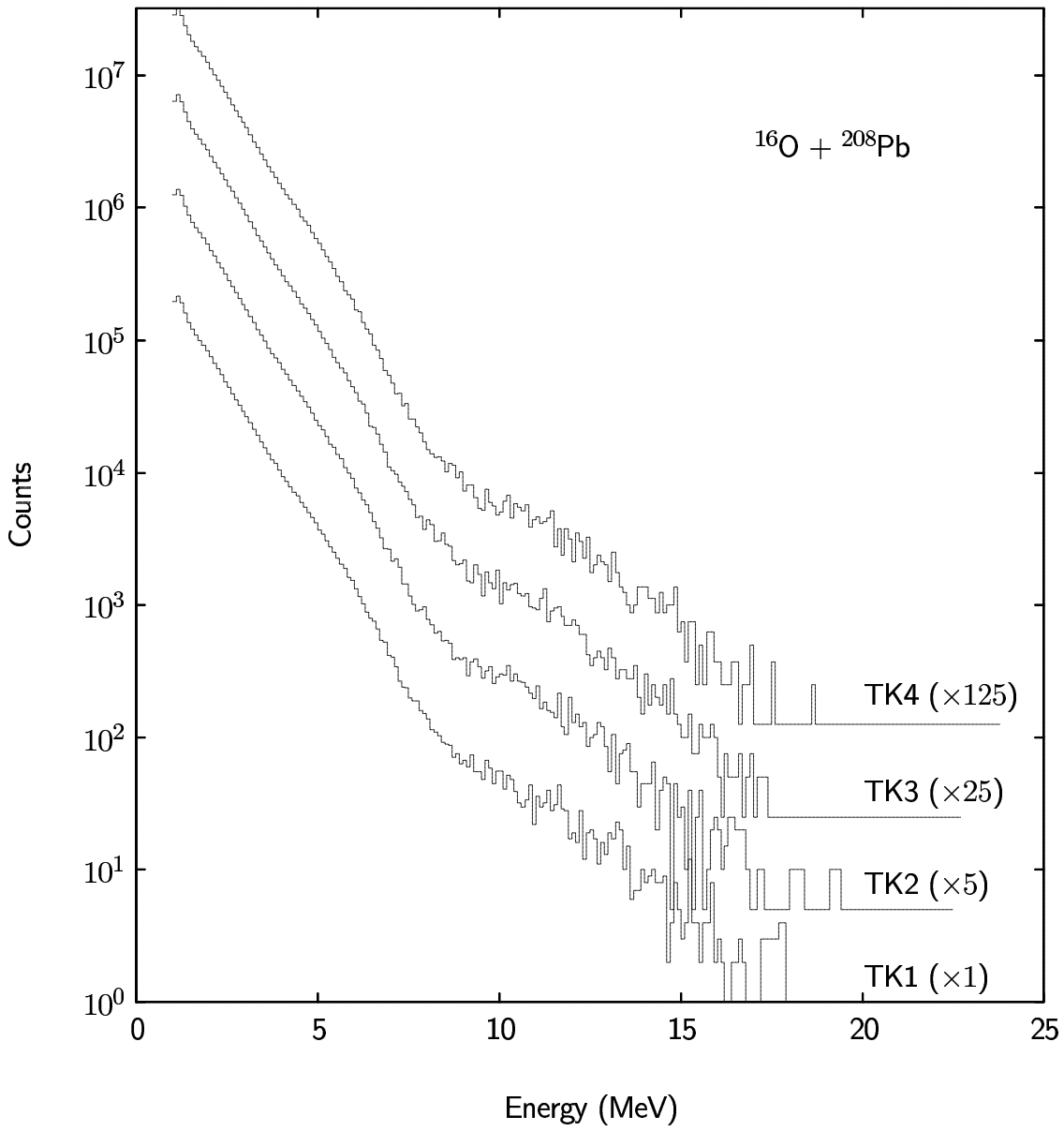

FIG. 45. Results of application of TKE cuts on the γ-ray energy for $^{16}O + ^{208}Pb$.

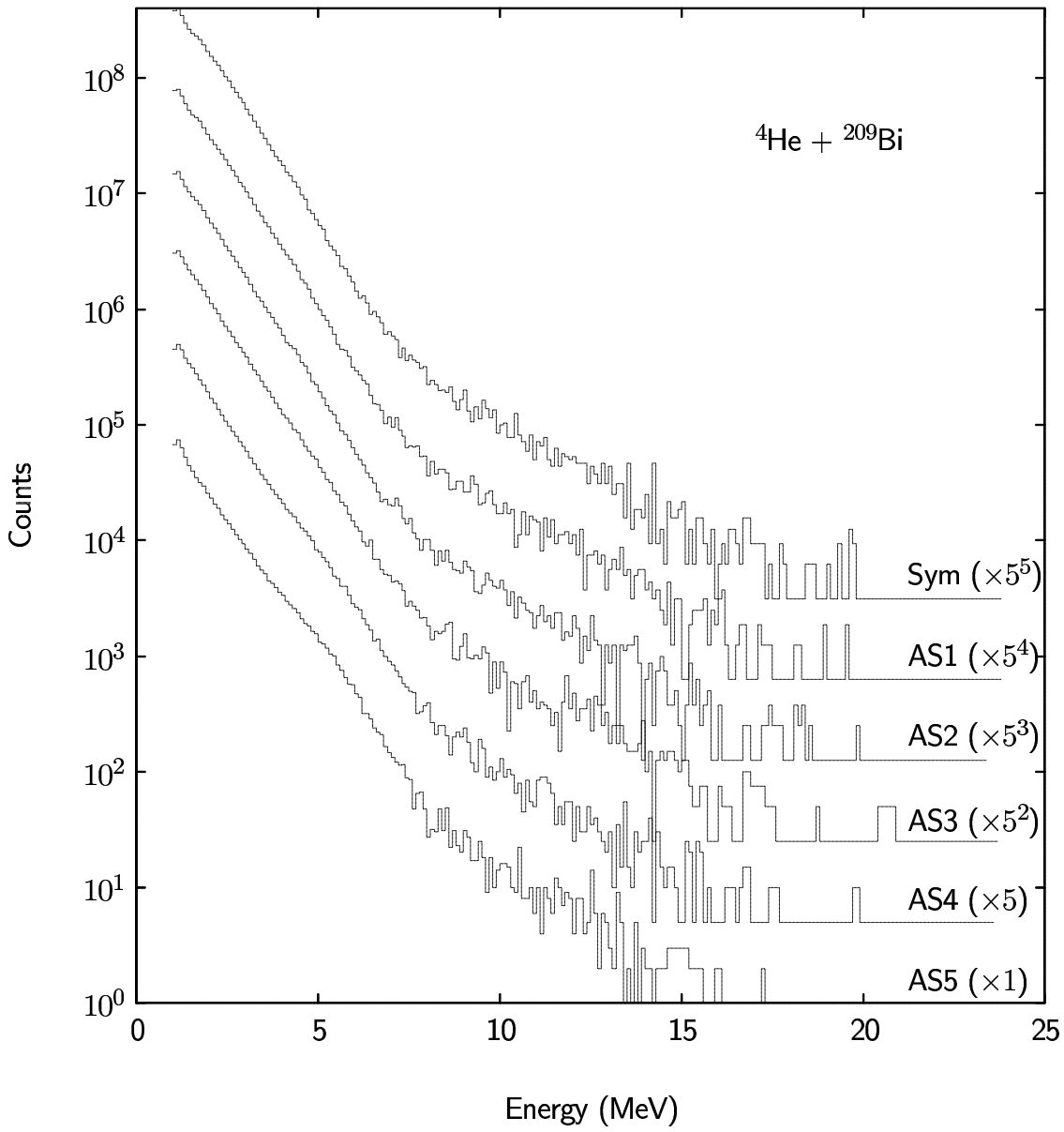

FIG. 46. Effects of different mass asymmetries on the γ-ray energy for ^{4}He + ^{209}Bi.

TABLE 14. Four TKE ranges investigated for ^{4}He + ^{209}Bi γ-ray – TKE dependence.

Cut	Range (MeV)
TK1	$90.0 \leq E < 127.4$
TK2	$127.4 \leq E < 149.7$
TK3	$149.7 \leq E < 162.0$
TK4	$162.0 \leq E < 210.0$

the figure. Again, there is no clear dependence of the total γ-ray energy on the TKE of the fission fragments.

These techniques were also applied to the data from the ^{16}O + ^{176}Yb runs, with similarly negative results. The TKE cuts used are listed in Table 15 while the TKE dependent γ-ray spectra for ^{16}O + ^{176}Yb are shown in Figure 48. Again, the highest TKE events are represented by the uppermost spectrum. There is no discernible difference between the spectra, once normalized, in either the GDR or the statistical regions, just as in the previous two cases. As noted above, the ^{4}He + ^{188}Os system yielded insufficient statistics to investigate the TKE dependence of the GDR γ rays. Now let us turn to the neutron results.

IV.3 Neutron Results

In the neutron analysis, each of the spectra from the eight DEMON detectors' locations were subjected to moving-source fits to determine the number of pre- and post-fission neutrons in fission. Fits such as these have been widely used in a great number of prior neutron time scale experiments [7–14, 60, 116, 117, 61, 118, 119, 129]. The basic technique revolves around the kinematic velocity boosts along the

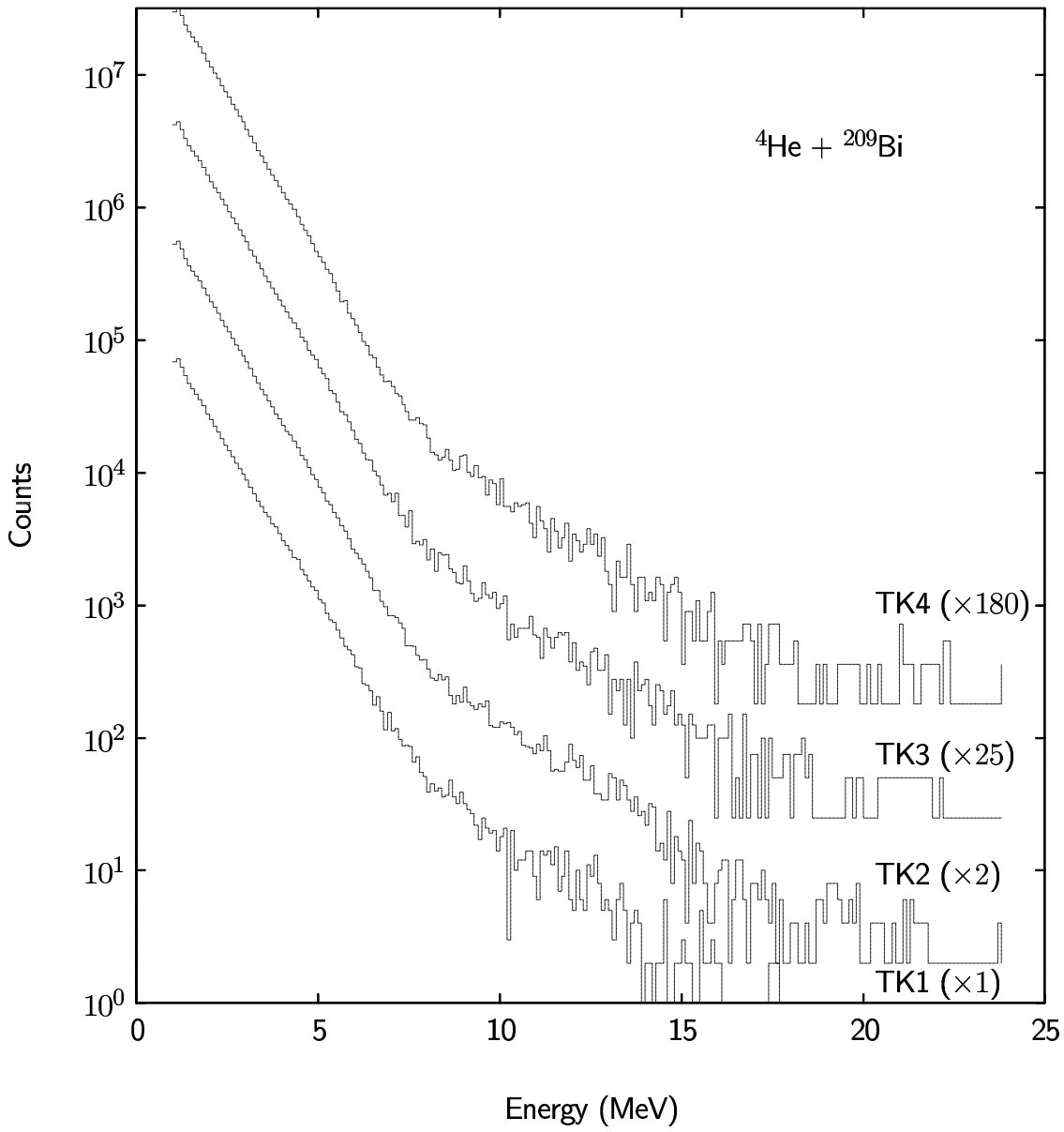

FIG. 47. Results of application of TKE cuts on the γ-ray energy for ^{4}He + ^{209}Bi.

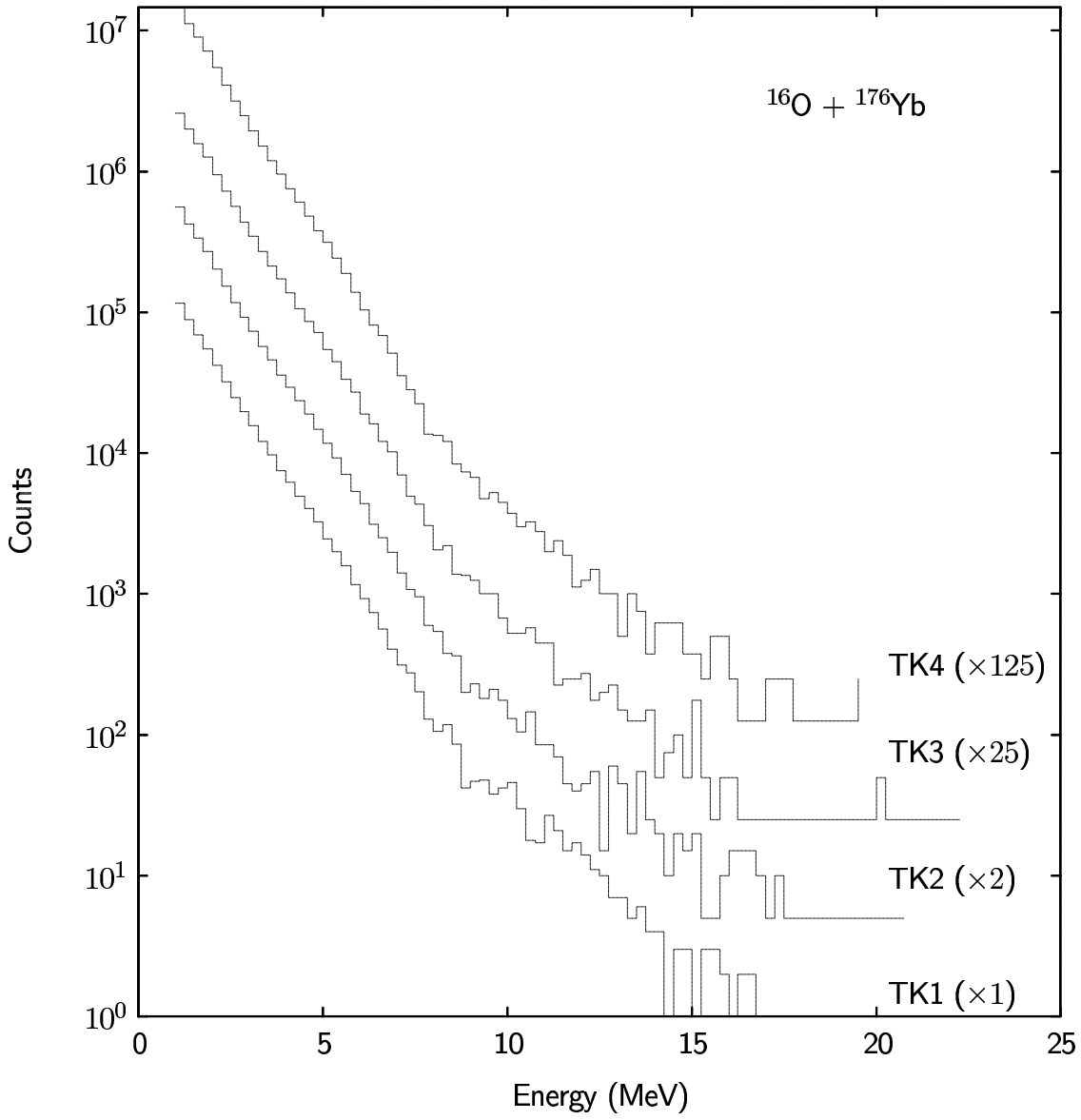

FIG. 48. Results of application of TKE cuts on the $^{16}O + ^{176}Yb$ γ-ray energy spectra.

TABLE 15. Four TKE ranges used for $^{16}O + ^{176}Yb$.

Cut	Range (MeV)
TK1	$62.0 \leq E < 118.0$
TK2	$118.0 \leq E < 133.0$
TK3	$133.0 \leq E < 148.0$
TK4	$148.0 \leq E < 202.0$

fission fragment directions. Of course, the deconvolution of the actual neutron energy spectra was complicated due to the large angular acceptance of the PPAC's and the exact position of the neutron counters. Given the accepted use of such fitting procedures and the fact that most of the analysis was carried out in Strasbourg, only an overview of this procedure will be presented here.

As mentioned in the previous chapter, the neutron energy spectra were corrected for total efficiency and the detection thresholds. From these, neutron energy spectra from each of the eight different positions were obtained. Five of the detectors corresponded to neutrons seen in the plane of the reactions. The remaining three were perpendicular to at least one of these five, establishing the "out-of-plane" view.

A sample energy spectrum for in-plane neutrons is shown in Figure 49. The corresponding out-of-plane spectrum is given in Figure 50. As expected, the spectra along the decay axis show considerably more yield than those perpendicular to the fission fragment emission angle. This is simply due to the kinematic enhancement of post-scission neutrons in the fission plane. Note that there is a cut-off at about

2 MeV. This is due to the efficiency and the ability to discriminate neutrons and γ rays in the pulse shape plots.

The in- and out-of-plane spectra were decomposed using a moving-source, least-squares fit. Three different sources were employed: the compound nucleus and either of the two daughter nuclei. Neutrons emitted before the nascent daughter nuclei have reached the majority of their acceleration are assumed to be isotropic in the center-of-mass frame of the system. It was further assumed that the neutron energy spectra followed a simple Maxwellian shape in the emitters' rest frames; i. e.,

$$Y(E_n) \propto E_n e^{-E_n/T}. \tag{32}$$

Here, $Y(E_n)$ is the yield of neutrons with a given energy, E_n.

With these assumptions, the iterative method described by Bishop *et al.* [130] and Ward *et al.* [131] was used to deduce the pre- and post-fission neutron spectra. Multiplicities were extracted from the best fits in the same manner as for the γ rays, i. e. by dividing neutrons detected by fissions detected and correcting for efficiency. Sample fits to the data are shown in Figure 49. One observes rather good agreement between the experiment and the fitted energy spectra.

The results of the best fits for all reactions are given in Table 16, for both the total energy spectra and for the same mass cuts used in the γ-ray analysis (see Tables 9, 10, and 11). The labeling "none" means that no mass cut was applied to the data. The mass cuts used in the ^{4}He + ^{188}Os analysis for the neutrons were the same as for the ^{16}O + ^{176}Yb system since these reactions produced the same compound nucleus. Estimated uncertainties are indicated in the table caption. Note

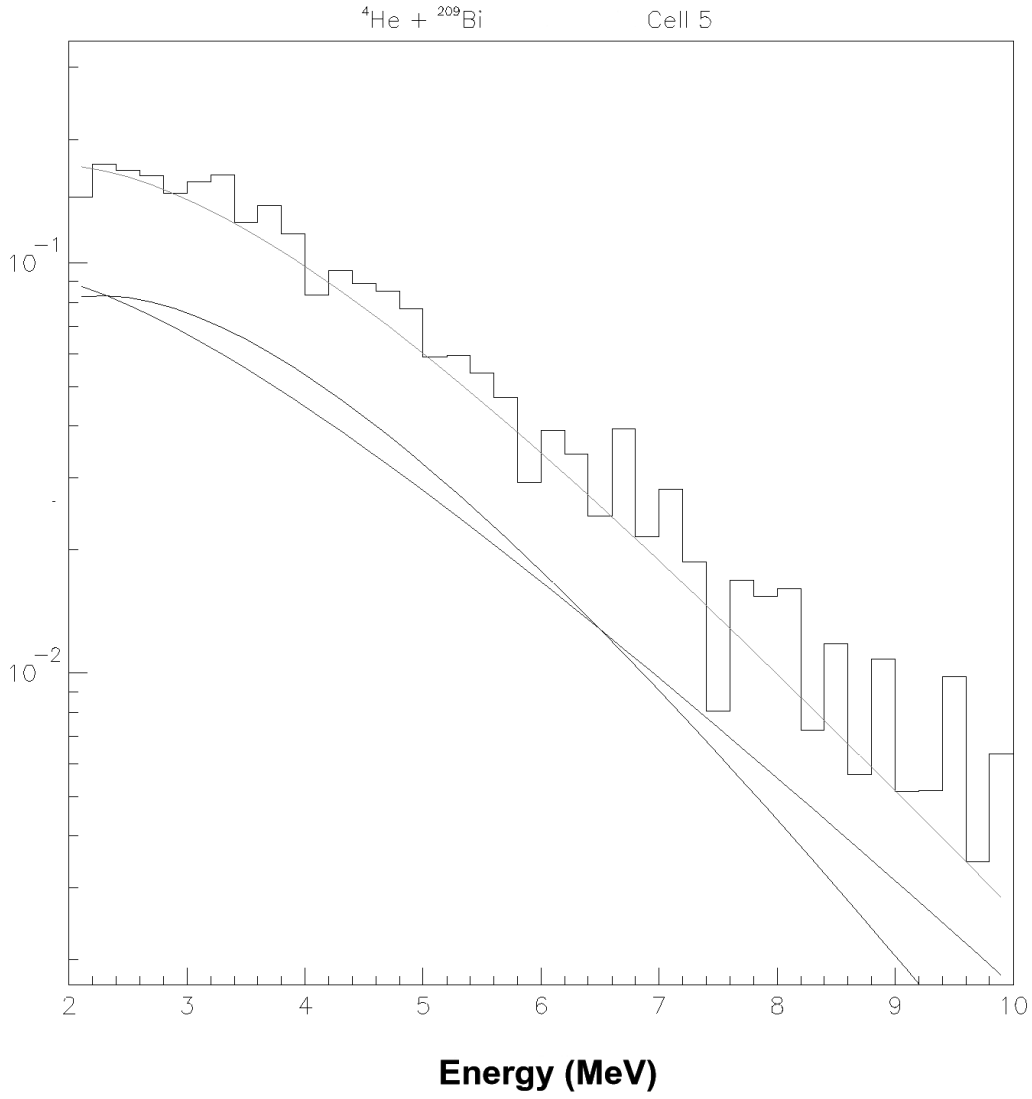

FIG. 49. Sample in-plane neutron energy spectrum for ^{4}He + ^{209}Bi. The lighter grey curve running through the histogram points represents the sum of all fitted contributions. The lower two curves represent fits to the pre-fission and the post-fission components, the darker one being the post-fission component.

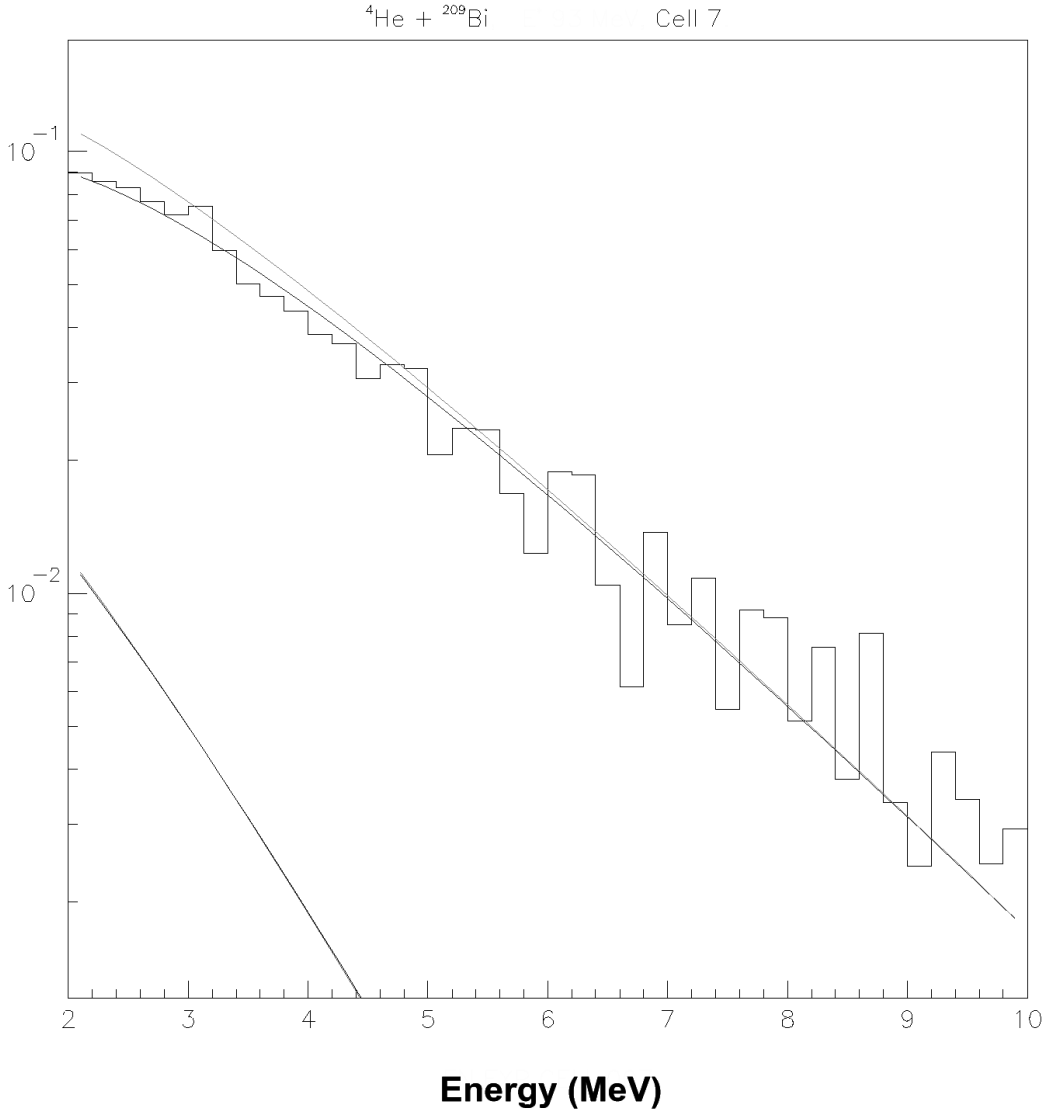

FIG. 50. Sample out-of-plane neutron energy spectrum for ^{4}He + ^{209}Bi. The lighter grey curve running through the histogram points represents the sum of all fitted contributions. The lowest curve represents the post-fission component, while the other dark curve represents the pre-fission component.

TABLE 16. Neutron multiplicities as determined from moving-source fits of the energy spectra for each reaction. The errors are estimated at 0.5 neutrons for ν_{pre}, 0.2 neutrons for ν_{post}, and 0.54 neutrons for ν_{tot}.

Reaction	Mass Cut	ν_{pre}	ν_{post}	ν_{tot}
$^{16}O + ^{208}Pb$	*none*	4.2	2.5	6.7
	Sym	4.3	2.5	6.8
	Asym1	4.0	2.7	6.7
	Asym2	4.0	2.6	6.6
	Asym3	4.0	3.0	7.0
	Asym4	4.4	2.5	6.9
	Asym5	4.4	2.4	6.8
	Asym6	4.3	2.0	6.3
$^{4}He + ^{209}Bi$	*none*	4.8	2.4	7.2
	Sym	4.6	2.6	7.2
	Asym1	4.7	2.6	7.1
	Asym2	5.0	2.5	7.5
	Asym3	4.7	2.6	7.1
	Asym4	4.9	2.7	7.6
	Asym5	4.8	2.4	7.2
	Asym6	4.8	2.0	6.8
$^{16}O + ^{176}Yb$	*none*	4.8	2.2	7.0
	Sym	4.8	2.2	7.0
	Asym1	4.7	2.2	6.9
	Asym2	4.7	2.0	6.7
$^{4}He + ^{188}Os$	*none*	4.4	2.6	7.0
	Sym	3.9	3.0	6.9
	Asym1	4.1	2.6	6.7
	Asym2	3.9	2.6	6.5

that ν_{tot} is simply the sum of ν_{pre} and ν_{post}, and does not include contributions from pre-equilibrium neutrons, which was assumed to be small. As expected from previous work, ν_{post} is essentially the same for all the systems. However, ν_{pre} is also nearly constant as well. This is likely due to the fact that the excitation energies are similar for the various reactions.

Systematic errors in the extracted values for ν_{pre} could result from deviations from isotropic emission in the center of mass of the sources. Such an anisotropy is expected to be small, and has been neglected in studies similar to the current work [7–14, 60, 116–119, 129]. While there is some support for this isotropic emission [7], it nevertheless remains a source of uncertainty. However, given the relatively low number of detectors and the uncertainties in the energy thresholds and efficiencies, the uncertainties for the neutron multiplicities make it impossible to see deviations from isotropy [132].

It is somewhat surprising that ν_{tot} is insensitive to mass asymmetry. From Q-values, one expects a decrease in ν_{tot} with increasing asymmetry. Presumably, this variation is masked by the significant error bars.

Reconstruction of the fission time scale using ν_{pre} is accomplished by estimation of the average lifetime for each emitted neutron in a stepwise fashion. Model calculations are needed to provide this. Statistical model calculations and some extensions will be discussed in the following chapter.

CHAPTER V

MODEL ANALYSIS

This chapter presents the quantitative details of the current work. The first section presents an overview of considerations important in the model analyses, particularly the fission mode. The section following discusses statistical model calculations in general. Additional details of the workings of various codes are also given. In the next section, some calculations are presented in detail. Quantitative comparisons between calculation and each of the reactions are then addressed.

V.1 Overview

The statistical model was introduced in Section I.3 in regards to neutron evaporation. This treatment was rather schematic. A more general treatment requires further exploration of some fundamental considerations behind the model. Chief among these is the idea that a fully equilibrated compound nucleus is formed through the complete fusion of a projectile and target. Subsequent decay of this system is assumed to be independent of the details of the formation process within the constraints of conservation laws. Aside from these constraints, the results are not sensitive to the initial conditions in which the system was produced.

It must be emphasized that statistical models are only a zeroth-order approximation for actual decays. Fission is definitely a dynamical process. In a statistical model there is basically no physical picture of how the system evolves in phase space. Still, statistical models provide some reasonably self-consistent guidelines. This is not

always the case for dynamical models. Dynamical models depend on the underlying potential energy, the associated inertias, and the viscosity (see below). In contrast, statistical models only rely on the behavior of the system at some critical point in phase space. In principle, the addition of various levels of sophistication in statistical models is generally straightforward. Given these considerations, statistical models have become a *de facto* standard of comparison. Deviations from statistical model predictions can highlight possible dynamical considerations.

In the earlier discussion of decay widths and branching ratios, there was inherent inclusion of aspects of both evaporative decay (for neutrons, light particles, and γ rays), but neglected the details of the transition state theory of fission, which is discussed in the following section.

V.2 Transition State Theory of Fission

The transition state theory (TST) was originally described by Eyring for chemical reactions [133]. It was later expanded to address fission by Bohr and Wheeler [5]. Although not explicitly mentioned in Chapter I, light particle evaporation models generally assume the detailed balance principle. This implies that emission follows the same path as fusion. This is certainly not the case in fission as shown by a comparison of fission fragment and fusion barriers. The former are much lower than the latter implying different paths for fission and fusion.

In TST, one again uses the expression

$$\tau_{fiss} = \frac{\hbar}{\Gamma_{fiss}}, \tag{33}$$

however, Γ_{fiss} is calculated quite differently. In particular, it is assumed that the system reaches a point of no return usually (but not necessarily) taken as the saddle point. All systems reaching this configuration, N^*, are assumed to decay. Thus the decay rate is assumed to reflect the quasi-static population of the critical configuration.

A potential energy surface for fission is given in Figure 51 (adapted from Ref. [5]). In this figure, V is the potential energy, ξ is the deformation, B_f is the fission barrier, K_f is the kinetic energy in the fission mode, E_f^* is the excitation energy at the saddle, and $\mathrm{d}E_f^*$ is an increment in E_f^*. For simple radioactive decay,

$$\frac{-dN}{dt} = N\lambda, \tag{34}$$

where λ is the decay constant. Since

$$\Gamma_f = \lambda\hbar = \frac{\hbar}{\tau_f}, \tag{35}$$

one has

$$N\lambda = \frac{N}{\tau_f} = \frac{N\Gamma_f}{\hbar}. \tag{36}$$

At the saddle point, the phase space is

$$\frac{dp_\xi d\xi}{h}\rho_f(E_f^*)dE_f^*, \tag{37}$$

where p_ξ is the momentum conjugate to ξ. Thus,

$$K_f = \frac{p_\xi^2}{2m_\xi}, \tag{38}$$

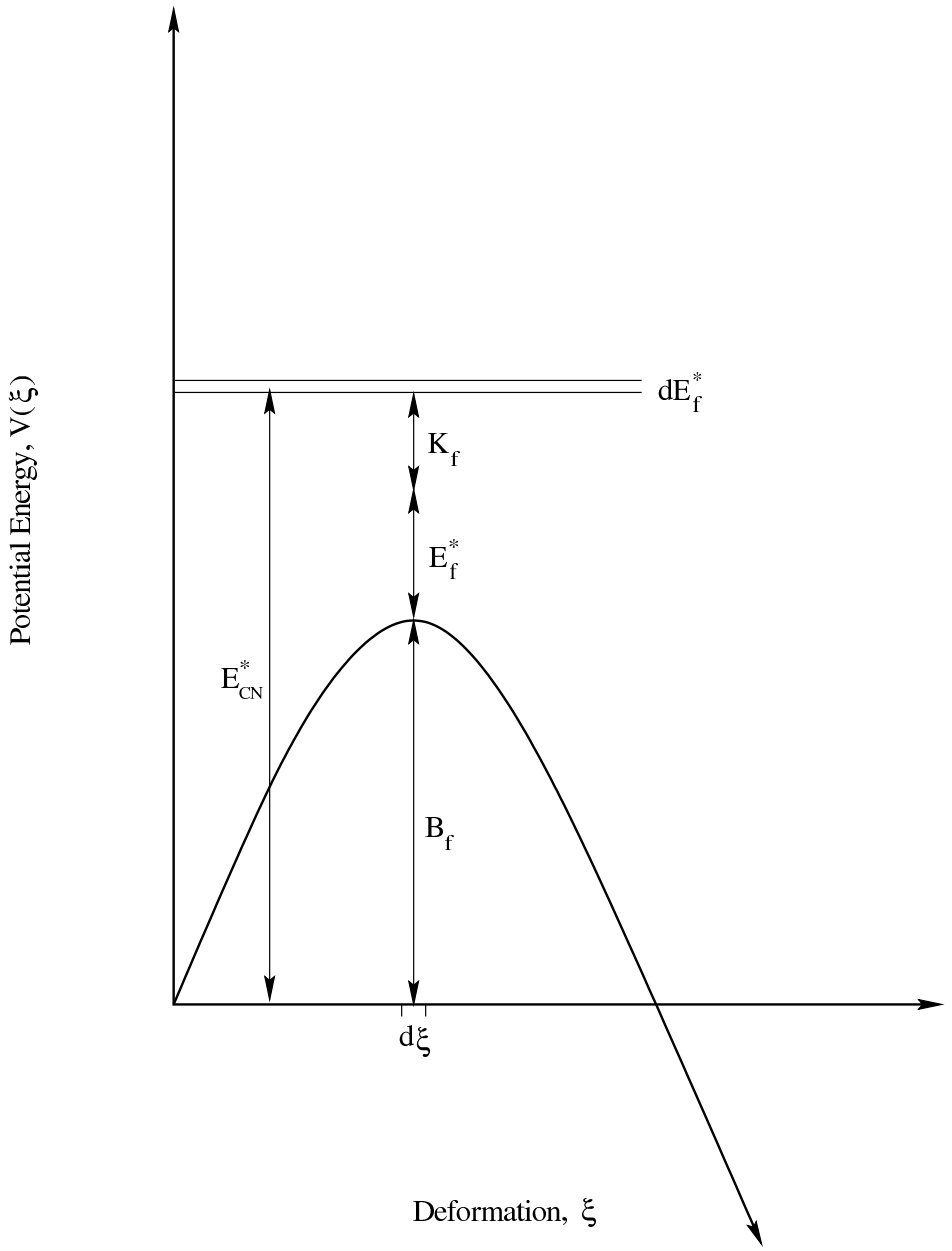

FIG. 51. Schematic representation of the total potential energy during the fission process. This illustrates the quantities discussed in Equations (38)–(46) (see text).

where m_ξ is the associated inertia. From the above,

$$dK_f = \frac{dp_\xi}{m_\xi} p_\xi = v_\xi dp_\xi. \tag{39}$$

In TST, the number of nuclei in the transition state is the initial number of decays. To proceed, one needs to integrate over all K_f's or, equivalently, all p_ξ's. So

$$\begin{aligned} N^* &= \frac{dN}{d\tau d\xi} = dE^* \int \frac{dp_\xi}{h} \rho(E^*) \\ &= dE^* \int \frac{v_\xi dp_\xi}{h} \rho(E^* - B_f - K_f) \\ &= \frac{dE^*}{h} \int \rho(E^* - B_f - K_f) dK_f. \end{aligned} \tag{40}$$

Comparing Equation (40) with Equation (36),

$$\frac{N^* dE^*}{h} = \frac{N\Gamma_f dE^*}{\hbar} = \rho(E*) \frac{\Gamma_f dE^*}{\hbar}, \tag{41}$$

so

$$\Gamma_f = \frac{N^*}{2\pi\rho(E^*)}. \tag{42}$$

If $\rho(E^*) = 1/D$, where D is the level spacing at the saddle, then one has

$$\Gamma_f = \frac{D}{2\pi} N^*. \tag{43}$$

For a given dK_f, one can write

$$\Gamma_f(E_f^*) dK_f = \frac{\rho_f(E^* - B_f - K_f) dK_f}{2\pi\rho(E^*)}. \tag{44}$$

Equations (43) and (44) are the Bohr-Wheeler expressions for Γ_f. An elegant but quite different derivation of these equations has been given by Mahan [134].

If $E_f^* \gg B_f$, one can perform a canonical expansion of Equations (43) and (44):

$$\Gamma_{f,total} = \frac{\int \rho(E_f^* - B_f - K_f) dK_f}{2\pi\rho(E^*)}$$

$$\approx \frac{T\rho(E^*)e^{-B_f/T}\int_0^\infty e^{-K_f/T}dK_f}{2\pi\rho(E^*)}$$

$$= \frac{T}{2\pi}e^{-B_f/T}, \tag{45}$$

where T is the effective temperature at the critical point.

V.3 Modifications to Transition State Theory

Equations (43), (44) and (45) neglect several effects as pointed out by Strutinsky [135] and Kramers. First, the above equations assume the K mode is a simple vibration. This together with the canonical approximation makes Γ_f sensitive to both the curvatures of $V(\xi)$ around the potential energy minimum at the equilibrium shape of the compound system and the shape of the fission barrier. These are characterized by $\hbar\omega_{eq}$ and $\hbar\omega_{sp}$, respectively. Second, these equations neglect the fact that it takes time to build up a quasi-static flux at the saddle point. Combining these effects, on obtains

$$\Gamma_f = \frac{\hbar\omega_{eq}}{2\pi}e^{-B_f/T}(\sqrt{1+\gamma^2} - \gamma), \tag{46}$$

where γ is the so-called nuclear viscosity coefficient and $\gamma = \beta/(2\omega_{sp})$, β being the reduced nuclear viscosity coefficient. The quantity γ reflects the transient time [37] or

fission time delay. Third, the above equations neglect the fact that B_f is a function of the angular momentum of the compound system [136].

Actually, γ is a somewhat artificial concept. It is a macroscopic quantity which reflects the fact that not all the systems which reach the saddle point actually decay. This is schematically illustrated in Fig. 52. In this figure, trajectories 1 and 3 lead to fission. In contrast, trajectories 2 and 4–6 do not (though 5 corresponds to a near fusion before breaking up). This depletion of decays implies that TST overestimates the decay width, Γ_f. This is better illustrated by the chemical exchange reaction

$$A + BC \rightarrow AB + C.$$

This is shown by the dynamical calculations in Fig. 53. Clearly, some trajectories are reflected from the barrier due to vibrational excitations. Obviously, fission is more complex, but Fig. 53 reflects the general idea. The existence of recrossing effects strongly suggests that points other than the saddle give a better approximation to Γ_f.

Recently, Lestone has added yet another limitation to TST [137]. In his approach, the fission decay width is limited by the distribution of K states during the fission decay process. It is very important to realize that here K is not the same as the kinetic energy along the fission axis. Rather, in accord with conventional notation, K here is the projection of the total angular momentum, I, along the fission axis. While the basis for the idea behind Lestone's theory is perhaps a good one, it may be flawed for at least two reasons. The K state distributions are generally assumed to

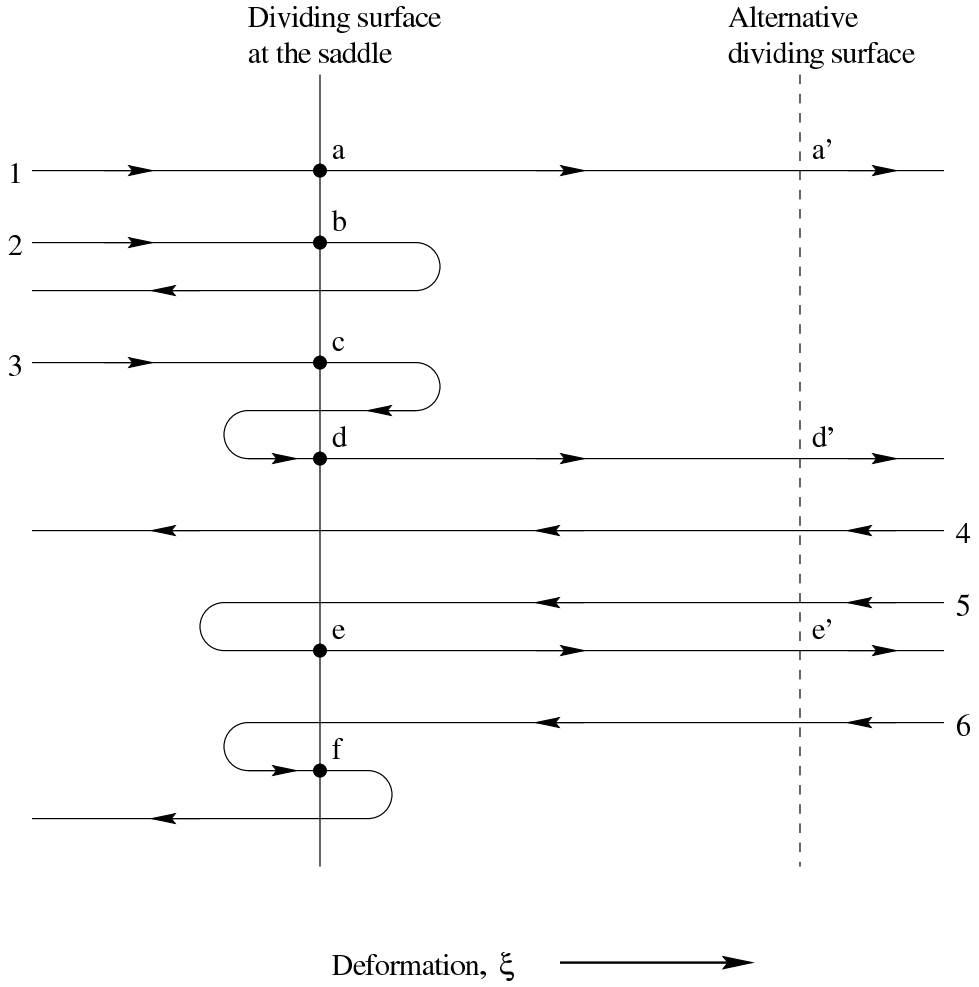

FIG. 52. Possible outcomes of nuclear shape evolution for a fissioning nucleus. Conventional fission (path 1), returning from over the saddle point configuration without fission (path 2), and double level-crossing leading to fission (path 3) are all illustrated. Paths 4, 5, and 6 indicate opposite cases to fission, i. e. fusion, in much the same manner.

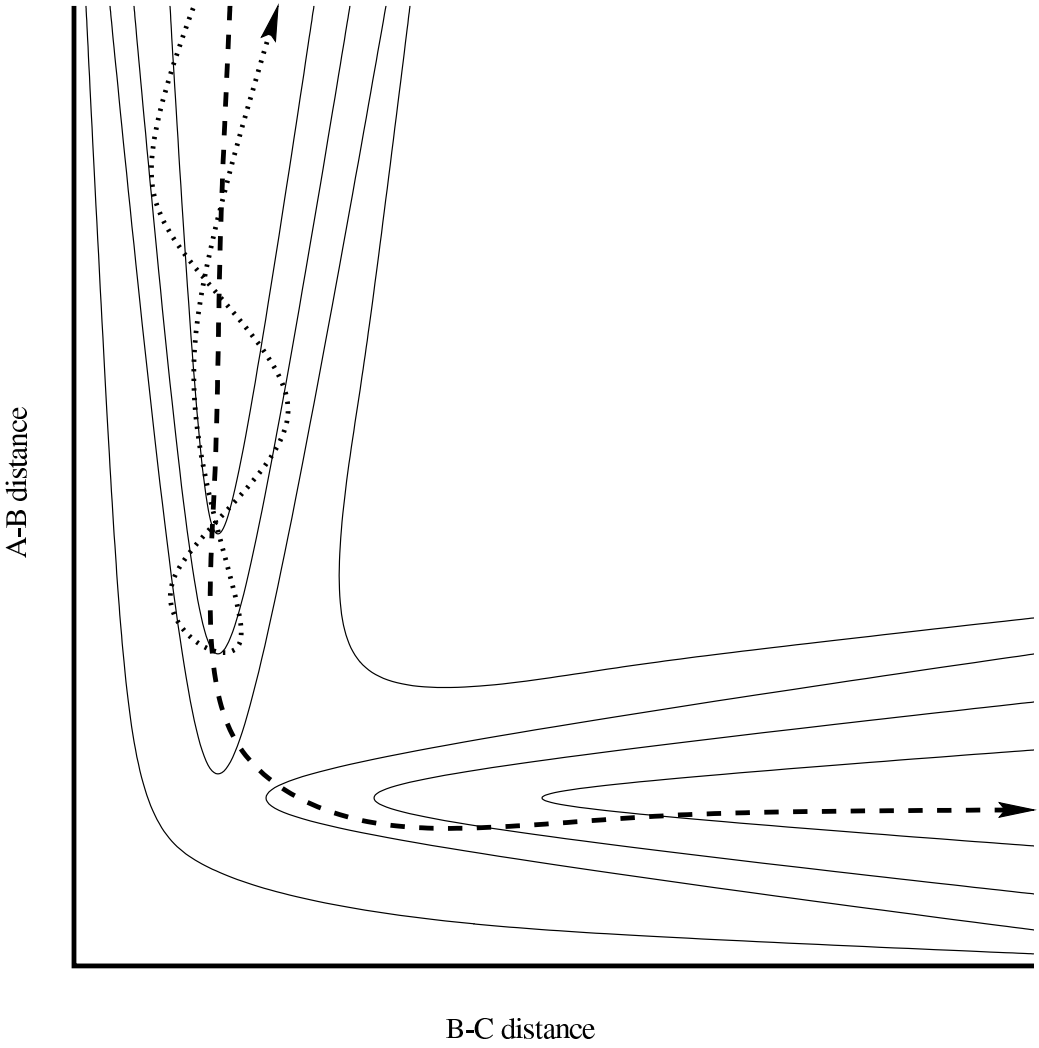

FIG. 53. Two possible trajectories for the reaction $A + BC \rightarrow AB + C$. The shaded line indicates a nucleus which is reflected from the saddle point whereas the dotted line shows successful fission. The distance A-B represents the distance (in deformation space) from the scission point configuration, while the distance B-C is the distance between the two products.

follow statistical equilibrium. To be more quantitative, the probabilities for a given total spin, I, and a given K are assumed to follow

$$P(I,K) \propto e^{-K^2/K_0^2}, \tag{47}$$

where K_0 characterizes the shape of the saddle.

Measurements of fission angular distributions for high spin systems have shown that the fluctuations in I are smaller than predicted by the liquid drop model saddle point shapes. This suggests that either K is not preserved during the descent from saddle to scission or that a truly equilibrated compound nucleus is not really formed. Lestone's work makes the former assumption. To some extent this will be addressed later. Before that however, the details of the model calculations are discussed below.

V.4 Statistical Model Calculations

In order to extract a fission time scale from the data, it is necessary to compare with quantitative models. As mentioned previously, statistical model codes such as CASCADE [56] and various modifications have been applied to time scales [24, 32, 126], with varying degrees of success. The result of such calculations is that the fission process is slower than predicted by standard statistical models. As mentioned above, there are good reasons for this apparent breakdown. Nonetheless it is useful to explore the workings of standard statistical model calculations.

Generally, these codes begin with the statistical assumption that a completely equilibrated compound nucleus is formed. The excitation energy and spin distributions are calculated from the various entrance channel parameters (projectile, target,

E_{lab}). Decay probabilities are calculated statistically from the level densities and barrier heights of the various decay modes. Most often, the only decay products considered are neutrons, protons, α-particles, fission, and γ rays. Relative decay widths for the various channels are calculated and used to generate a so-called "S-matrix" of population cross sections of the daughter nuclei. These calculations are performed as a function of excitation energy and angular momentum. The procedure is followed for the daughter nuclei, in a cascade through all possible decay sequences. For example, the γ-ray spectrum for decay of a particular state with excitation energy E_1 and angular momentum J_1 is given by

$$\sigma_\gamma(E_1, J_1, E_\gamma) = \sigma_p(E_1, J_1) \sum_L P_\gamma(E_1, J_1, E_\gamma, L), \tag{48}$$

where $P_\gamma(E_1, J_1, E_\gamma, L)$ is the probability of emission of a γ ray with energy E_γ and multipolarity L. The cross section for populating the particular state with energy E_1 and spin J_1 is given by $\sigma_p(E_1, J_1)$. In standard CASCADE calculations only the multipolarities M1 (magnetic dipole), E1 (GDR), and E2 (giant quadrupole) are usually treated. Some extensions to CASCADE also follow the fission mode [24, 32, 126]. Once the excitation energy has fallen below the particle threshold, the decay cascade deals only with γ emissions. Such model calculations have been extensively explored by many authors. Hurst *et al.* have also explored the assumption of equilibrated systems in incomplete fusion reactions [138].

While the various neutron studies have used a number of different codes, the GDR studies have all used some version of CASCADE [23–32]. Thus, it seemed prudent to use variations of CASCADE for the current work. CASCADE allows

direct comparisons with prior GDR results without creating additional complications due to new variables and differing assumptions. This is important because of the major new constraint in the current work that simultaneous measurements of both neutrons and γ rays were made. Many versions of CASCADE exist. The version used here was van't Hof's TIMCASC [32].

This choice was necessitated by a variety of factors. The standard CASCADE codes do not distinguish between decays from a nucleus that will end up as an evaporation residue and a nucleus that fissions. This is clearly insufficient for the experiments under discussion, as γ rays were only measured in coincidence with fission. Additionally, most CASCADE codes do not follow the decay of the fission fragments, even though the probability for fission is calculated. While one other code does incorporate this (CASMASS [24, 126]), it does so less efficiently and somewhat schematically. It is obviously necessary to follow decay of the fragments, since systems like ^{16}O + ^{176}Yb and ^{4}He + ^{188}Os have relatively small fission cross sections. Furthermore, no other version of CASCADE has a self-consistent implementation of the concept of time. It also has provision for a fission hindrance factor, in the form of a friction constant (the term "γ" in Equation (4)) similar to the latest version of CASMASS. The modifications made in producing TIMCASC were extensively tested and debugged by the authors to show that results from the code were in accord with prior versions. These modifications are discussed in detail in van't Hof's recent work [32] and will only briefly be described here.

In order to restrict decay of compound nuclei to those destined to fission, the decay cascade in TIMCASC is performed in time-reversed fashion. Since the code is

not of the Monte Carlo type, the various matrices involved can be actually calculated in any arbitrary order. The calculation is begun at the bottom of the decay cascade for the element with the lowest excitation energy E_{low} (not necessarily zero). It then proceeds to higher excitation energies and higher masses until the initial compound system is reached. Working through the cascade in reverse fashion allows for a simple determination of paths leading to fission. Thus, a modified S-matrix is calculated to obtain (as in the example above) the γ-ray spectrum for a particular state that will fission at a later step in the cascade; i. e.,

$$\sigma_\gamma(E_1, J_1, E_\gamma) = \sigma_p(E_1, J_1) \sum_L \sum_{J_2} P_\gamma(E_1, J_1, E_\gamma, L) Q_N(E_2, J_2). \tag{49}$$

Here, $E_2 = E_1$ - E_γ and $J_2 = J_1 \pm L$ are the energy and the angular momentum of the nucleus after emitting the γ ray, respectively. N is number of the current decay step. The probability $Q_N(E_2, J_2)$ that fission will occur at a later stage N in the decay cascade is given by

$$Q_N(E_2, J_2) = P_f(E_2, J_2) + \sum_i \sum_{E_3} \sum_{J_3} P_i(E_2, J_2) Q_{N+1}(E_3, J_3), \tag{50}$$

where P_f is the probability that fission will occur immediately after emission of the γ ray. For any other subsequent decay mode with probability P_i, a new state is formed with excitation energy E_3 and angular momentum J_3. Again the probability for fission in a later step, $Q_{N+1}(E_3, J_3)$, has to be calculated. The index i runs over all decay modes other than fission. At the last step in the cascade $Q_N(E_{low}, J) = P_f(E_{low}, J)$, thus allowing previous Q_N's to be calculated from this quantity and the various decay probabilities in a reverse manner.

In addition to the modified S-matrix calculations, a corresponding "T-matrix" (lifetime matrix) is also calculated. The lifetime depends upon the same variables as the state and is constructed from the decay width of each state, as per Equation (17). Analogous to Equation (6), the total decay width Γ_{tot} for a state with a particular excitation energy and angular momentum is taken to be a sum of that state's various decay widths followed in the cascade,

$$\Gamma_{tot} = \Gamma_n + \Gamma_p + \Gamma_\alpha + \Gamma_\gamma + \Gamma_f(t) \tag{51}$$

for neutron, proton, α particle, γ ray, and time-dependent fission decay widths, respectively. The time-dependence of the fission decay width comes about from the use of the Kramers fission width (Equation (4)) and is of the form

$$\Gamma_f(t) = \Gamma_f^{KR}(1 - e^{-2.3t/\tau}). \tag{52}$$

Here, t is the time and τ is the time required to reach 90% of the quasi-stationary fission flux across the saddle point. The term τ is expressed in terms of the friction constant γ and nuclear temperature T

$$\tau(\gamma, T) = \frac{1}{2\gamma} ln(\frac{10E_f}{T}) + \frac{0.0112\gamma A}{T} \tag{53}$$

based on the work of Weidenmüller and Zhang [37], and is calculated in the code in units of 10^{-21} seconds (zs). This is evaluated for every state (E,J).

The time t that enters into Equation (52) is the sum of the time with which a certain state (E,J) is populated. The time step belonging to the decay of the state (E,J) is defined by combining Equation (17) with Equation (51) to yield

$$\Delta t = \frac{\hbar}{\sum_i \Gamma_i + \Gamma_f^{KR}(1 - e^{-2.3(t+\Delta t)/\tau})}, \tag{54}$$

which must be solved iteratively, since the fission width is time dependent. These are calculated for each state in the cascade. If a state is populated via different decay paths, the lifetime is averaged with the calculated cross sections as weighting factors.

The decay of the fragments is followed by using the calculated fission cross sections for every nucleus in the decay process. Fragment mass distributions are assumed to be Gaussian using the width determined from the fission fragment analyses in the previous chapters. The charge distribution is calculated assuming equal fragment charge-to-mass ratios. Viola systematics are assumed, since they match well with the aforementioned fragment analyses. The fragments are assumed to have equal temperatures. The angular momenta of the fragments is determined by a simplified parameterization by Thoennessen *et al.* [23] based on a calculation by Schmitt *et al.* [139]. The GDR centroids for the fragments are calculated as per Equation (19). The resulting γ-ray spectrum of each fragment of given mass, charge, excitation energy, and angular momentum is then taken from a database of pre-calculated fragment spectra and weighted according to its relative probability. This is done for each fragment produced in the decay cascade. The spectra are accumulated into a total post-fission γ-ray spectrum for all fragments. This is efficient when performing many calculations for a given compound nucleus, such as in the fitting procedures described in the following sections. This entire fragment decay procedure is implemented as a post-processor to TIMCASC. The program FFPOP is used to read the matrices of fission cross sections produced by TIMCASC to produce the final post-fission spectrum.

V.5 TIMCASC Overview and γ-ray Considerations

Before going on to discuss the results of using these parameters, it is useful to review the importance and implications of each parameter in turn. For the reactions studied here, a level density parameter of $a = A/8$ MeV^{-1} was used, as in previous GDR studies [27]. The default values for the diffuseness of the angular-momentum distribution of the compound nucleus and the ratio of the level density parameter at the saddle point to the level density parameter at equilibrium were used; i.e., $2\hbar$ and 1.0, respectively. Other standard values are available from systematics for the other parameters, so only the remaining non-standard values will be discussed here.

A very important input parameter to any version of CASCADE is the fusion cross section. Since some of the reactions studied here do not have experimentally determined fusion cross sections, the parameterization of Wilke *et al.* [81] has been used to calculate the cross sections. Checking the validity of these cross sections against systems with similar beam energy, target, and projectiles yields reasonable agreement. The actual values used for the fusion cross sections are listed in Table 3. These fusion cross sections limit the absolute yield of the various decay modes in TIMCASC and are thus important when comparing to experimentally observed γ-ray multiplicities.

As explained in the previous section, a fission hindrance factor in the form of the Kramers friction constant γ was introduced. This is another important input

TABLE 17. Fraction of the fission barriers used in TIMCASC for all systems as a function of γ.

γ	$^{16}O + ^{208}Pb$	$^{16}O + ^{176}Yb$	$^{4}He + ^{209}Bi$
0.01	1.00	0.966	1.023
0.04	1.00	0.975	1.041
0.10	1.00	0.975	1.040
0.40	1.00	0.960	1.013
1.00	1.00	0.933	0.965
2.00	0.97	0.905	0.915
4.00	0.95	0.875	0.860
7.00	0.93	0.850	0.815
10.00	0.91	0.835	0.788
20.00	0.88	0.810	0.740
40.00	0.85	0.785	0.710

parameter for TIMCASC and also affects the yields from the various decay modes. Values ranging from as low as γ=0.01 to as high as γ=40 were used.

The initial fission barrier heights used were in general 100% of the Sierk values [140] already in the code. For each value of γ, the barrier height was then adjusted by a factor FFB to match the fission cross section used in Table 3. Numerous calculations were performed to determine the correct FFB for each γ for each system to within 2 mb of the expected values. For overdamped cases, this required an appreciable lowering of the barrier. For underdamped cases, a slightly higher barrier was required. The factor FFB is listed for all systems at various values of the friction constant γ in Table 17.

The GDR in TIMCASC is treated as having two Lorentzian components $E_\perp$ and $E_{||}$, which serve to describe spherical, prolate, and oblate configurations. The input parameters for these are the only parameters allowed to vary in the fitting process. The two centroids, their widths ($\Gamma_\perp$ and $\Gamma_{||}$) and their fractional strengths ($S_\perp$ and $S_{||}$) are subject to a chi-square fitting procedure against the experimental yield. The initial constraints were that the relative strengths add up to 1; i. e. that 100% of the TRK sum rule was observed. This proved to be inadequate for the less fissile systems, and the sum rule strength was also allowed to vary as a fitting parameter, which will be discussed in more detail in later sections of this chapter. The overall centroid energy E_{cen} is related to the two components

$$E_{cen} = \frac{\sum_i S_i E_i}{\sum_i S_i}, \tag{55}$$

where S_i is the strength of the i^{th} component.

Taking the widths to be some constant fraction c of the centroid energies of both components, the equation

$$\Gamma_i = cE_i^2 \tag{56}$$

is used in the calculation of the width Γ_i from c and E_i. Additionally, the shape of the system can be expressed as the nuclear deformation β, which is given by [32]

$$\beta = \sqrt{\frac{4\pi}{5}} \frac{(E_\perp/E_{||}) - 1}{(E_\perp/(2E_{||})) + 0.8665}. \tag{57}$$

The values of the various fitting parameters were determined by a chi-square fitting using the code MINUIT [141] which used TIMCASC as a subroutine. Thus, by taking advantage of the relationship between deformation and relative strength and

TABLE 18. Input parameters used in TIMCASC for each reaction.

Reaction	E_{cen} (MeV)	$S_\perp$	c	β
$^{16}O + {}^{208}Pb$	12.0	0.0 to 1.0	0.03	-1.5 to 1.5
$^{4}He + {}^{209}Bi$	12.1	0.0 to 1.0	0.03	-0.5 to 0.5
$^{16}O + {}^{176}Yb$	12.7	0.0 to 1.0	0.03	-0.5 to 0.5

of the constraints, the six parameters can be reduced to four fitting parameters (E_{cen}, $S_\perp$, c, β). Only two of these were used, since it was determined early in the analysis that E_{cen} and c converged to constant values. Eliminating these two free parameters speeded up the fitting process. Also, the fits were particularly insensitive to variations in c in the range of 0.01 to 0.09, which are reasonable limits given the form of Equation (56). The quantity $S_\perp$ must necessarily be limited to the range between 0 and 1, since it and $S_{||}$ are assumed to sum to the full strength (i. e., 1) of the TRK sum rule, given that no other fractional strengths are considered. Beta was initially chosen to have a very large range of possible values (i. e., $-1.5 < \beta < 1.5$) to avoid biasing the fit and to understand the fitting routine's initial behavior at large deformation for the $^{16}O + {}^{208}Pb$ reaction. This range was subsequently shortened to $-0.5 < \beta < 0.5$ for the other two systems. The ranges and values of the parameters used are summarized in Table 18. In the final analysis, the values for E_{cen} and c were held constant. The value for c was taken to be 0.03 for all reactions, while E_{cen} was 12.0, 12.1, and 12.7 for the reactions $^{16}O + {}^{208}Pb$, $^{4}He + {}^{209}Bi$, and $^{16}O + {}^{176}Yb$, respectively. This was done to reduce the number of fitting parameters, both for its own sake and so that the calculations would run faster. Several earlier

runs of the fitting procedure had indicated that E_{cen} and c consistently converged to approximately those values. Furthermore, small changes in those two parameters did not significantly affect the fits, according to the χ^2/N results. Note that the preferred values for E_{cen} for these fits were consistently 1 MeV below that predicted by the empirical relationship given in Equation (1), matching the observations of Chakrabarty *et al.* [142]. This is understandable since that relation was taken for GDR's built on the ground state rather than a variety of excited states as in these systems.

V.6 Reproducing the Neutron Data with TIMCASC

While the above discussion has focussed on the γ-ray analysis, the neutron pre-fission multiplicity results were treated by varying the friction coefficient γ until the experimentally observed number of pre-scission neutrons was obtained. Because the neutron multiplicities varied only very slightly with deformation and other parameters used in the GDR fits, each system was simply taken to form a spherical compound nucleus with ground-state GDR behavior.

The effects on ν_{pre} of varying the friction coefficients are presented in Figure 54. The curves indicate the calculated values, while the points with error bars indicate the experimentally determined values. A number of interesting features are readily apparent. First, one notices that the calculated shapes for each are quite dissimilar. The most fissile system (^{16}O + ^{208}Pb) exhibits an increasing (though tailing off) number of pre-scission neutrons with increasing nuclear friction, whereas the extremely

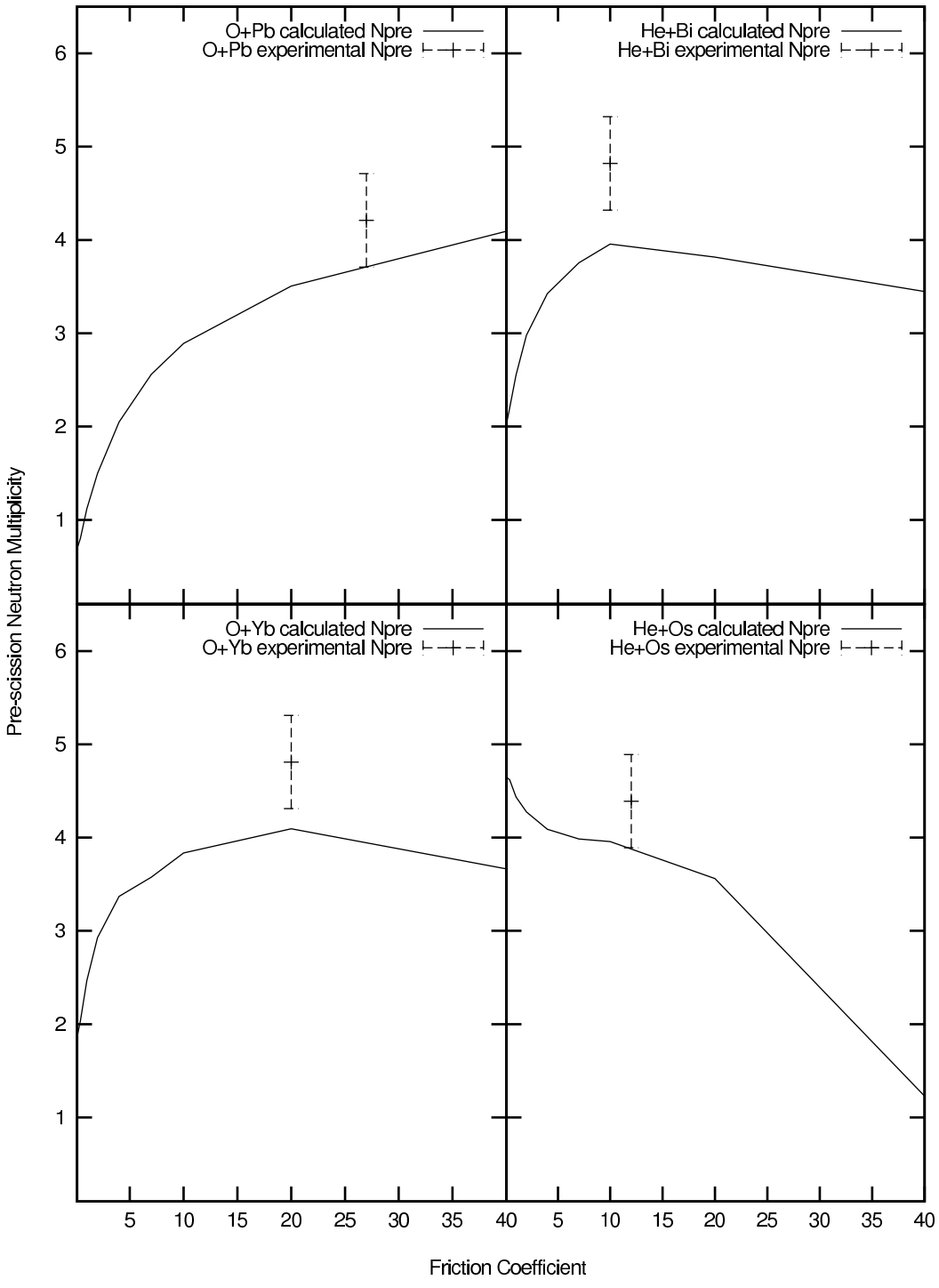

FIG. 54. Calculated ν_{pre} values as a function of friction coefficient for all systems.

non-fissile system (^{4}He + ^{188}Os) has the opposite behavior. The two remaining systems seem to fall between these two extremes, both starting off at low values of ν_{pre}, then rising to some maximum before falling off again. The experimentally observed ν_{pre}'s are plotted either where the calculations come closest to them or where they first fall within the experimental error. This serves to effectively set ranges on the friction coefficient γ for each system. Table 19 presents these limiting values.

TABLE 19. Limits on friction coefficients determined from neutron analysis.

Reaction	Experimental ν_{pre}	Friction Coefficient γ
^{16}O + ^{208}Pb	4.2 ± 0.5	≥ 25
^{4}He + ^{209}Bi	4.8 ± 0.5	$7 - 25$
^{16}O + ^{176}Yb	4.8 ± 0.5	$10 - 30$
^{4}He + ^{188}Os	4.4 ± 0.5	$5 - 20$

Another interesting feature is the apparent leveling out of ν_{pre} at moderately high values of γ. This makes an absolute determination of the optimal friction coefficients problematic. While smaller errors in the experimentally determined values of ν_{pre} would help, it is apparent that this is only a small part of the problem. Other workers have also noted large ranges in friction coefficients using the neutron method [13, 59]. Other methods of determining friction coefficients are necessary to more fully understand the implications of including an inherently dynamical concept such as nuclear friction in statistical codes.

V.7 Fit Results for GDR γ rays

The user input parameters for this reaction were previously listed in Table 18. The spectra produced from the fits for $^{16}O + ^{208}Pb$ are compared visually to the experimental results in Figure 55. While the fit for $\gamma = 7$ is clearly the best, both visually and from its χ^2/N value (see below), the others for $\gamma = 4$ and 10 are quite reasonable as well. This suggests that γ for this reaction could be anywhere from 4 to 10 with 7 being the most probable value. The slight structure visible in the $\gamma = 2$ case around 10 MeV is most likely a combined effect of the extremely large deformation with the relatively narrow ground-state GDR width. The quality of the fit for $\gamma = 7$ provides the best value of the friction coefficient for this reaction. That value also agrees with much of the other GDR γ-ray work to date, falling just below the middle of the range [24, 25, 26, 28, 31, 32, 34, 79, 80].

The final fit values for the reaction $^{16}O + ^{208}Pb$ are summarized in Table 20 and the χ^2/N values are plotted in Figure 56. There is a clear minimum in χ^2/N at $\gamma = 7$. Note that the best fits for the other values of γ required superdeformed oblate shapes ($\beta \approx 1.5$, the lower limit of the initial fitting range), which would be extremely unexpected for this system. Even the final value is a quite deformed shape (though prolate), with an axis ratio of about 3:1. This is higher than expected, but not without similar precedent in such analyses [31, 32, 126]. It is also worth considering that the deformation space of the fissioning system will be sampled by GDR emission all the way up until scission, whereas most models and predictions deal with the saddle point exclusively. Still, quite possibly a smaller deformation would be required if a value of

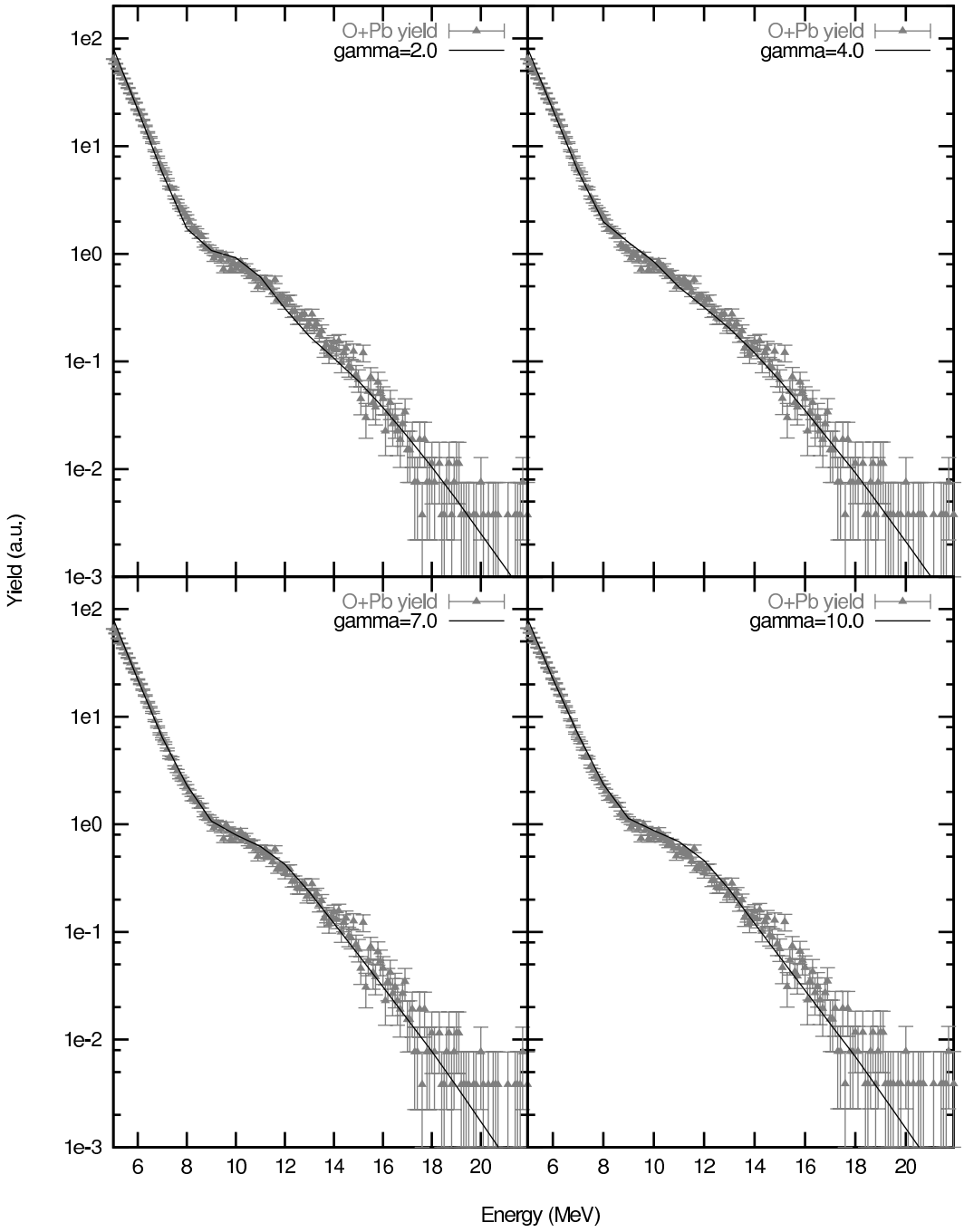

FIG. 55. Results of four of the best MINUIT fits to the $^{16}O + ^{208}Pb$ experimental γ-ray yields. The values of γ for each are indicated in each quadrant.

TABLE 20. Fit results from MINUIT linked to TIMCASC for the reaction $^{16}O + ^{208}Pb$.

γ	$S_\perp$	β	χ^2/N
0.1	0.9502	-1.4979	12.9
0.4	0.9581	-1.4995	10.1
1.0	0.9725	-1.4852	7.4
2.0	0.9695	-1.2574	6.7
4.0	0.3000	-0.3397	3.7
7.0	0.9140	0.5540	1.2
10.0	0.9260	0.6034	3.6

greater than 100% for the TRK sum rule had been used. However, the fit for $^{16}O + ^{208}Pb$ was quite satisfactory and did not require artificial enhancement of the TRK sum rule. Such measures were required for the other reactions, and will be discussed later in this section. Also apparent in Table 20 is the fact that the values for $S_\perp$ are generally heavily weighted towards favoring the perpendicular component to the GDR γ-ray energy. This suggests either that an even lower E_{cen} should be allowed or, again, that a TRK sum rule strength greater than 100% should be used.

The remaining reactions, $^4He + ^{209}Bi$ and $^{16}O + ^{176}Yb$, are not listed in Table 20 since in these cases MINUIT was repeatedly caught in local minima, regardless of starting values and step sizes. For $^4He + ^{209}Bi$, this produced χ^2/N values no smaller than 20. In the case of $^{16}O + ^{176}Yb$, the situation was even worse, with χ^2/N's no smaller than 70. Clearly, such fits are unacceptable. Samples of these for the two reactions are presented in Figure 57. The rather poor fits shown are representative of the best results the fitting procedure MINUIT was able to give using the input values

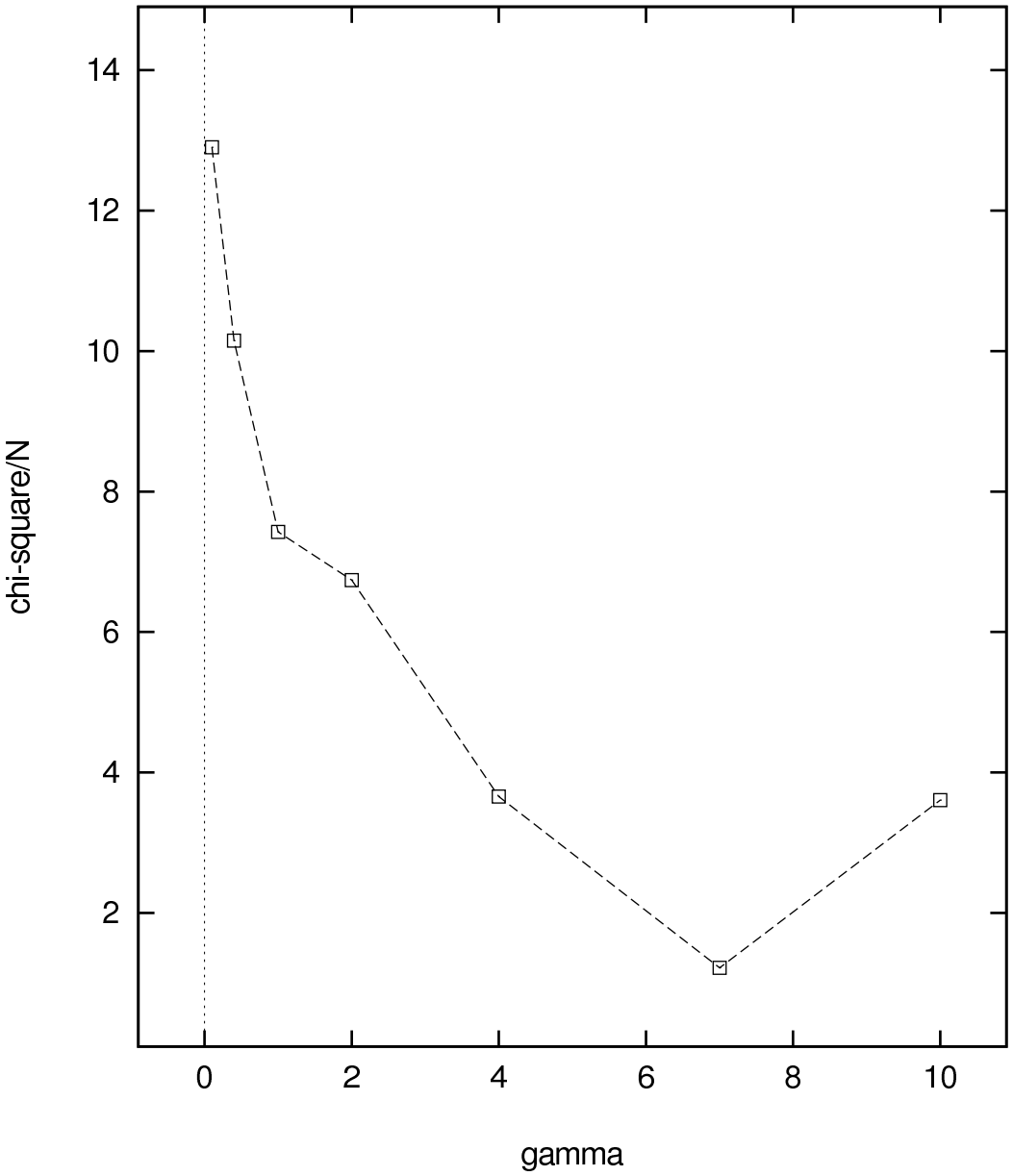

FIG. 56. Quality of the MINUIT fits for $^{16}O + ^{208}Pb$ for the various values of γ. The dotted lines connecting the points only serve to aid the eye.

listed in Table 18. In order to investigate whether MINUIT was wholly at fault or whether some other factor must be adjusted, quite a large number of calculations were run in which the separate parameters were varied by hand. This allowed careful tracking of the sensitivity of the fits to the various individual parameters.

Upon undertaking this procedure, it quickly became apparent that MINUIT was not wholly at fault. A number of other parameters were varied before more adequately fitting the experimental results. Finally, values greater than 100% for the TRK sum rule were used. This proved quite useful, and reasonable fits were obtained. Previously, some investigators have used up to 160% of the sum rule [32, 143, 144, 145]. The sum rule strength is the strongest parameter for fitting the experimentally observed spectrum, with the friction coefficient γ following and the deformation β as close seconds. The failure of the fits in the GDR region suggests that the sum rule might exceed 100%. It should be noted that strengths greater than 100% have been noted by other authors [32, 146]. Deviations from the sum rule are generally attributed to collective effects such as quasi-deuteron formation (the TRK sum rule ignores these). It is not clear from the present results why these less fissile systems would increase the strengths. However, there is essentially no other GDR γ-ray data associated with fission for similar systems. Further work is needed to clarify the situation.

The alternate fitting method used four fitting parameters: the nuclear deformation β, the friction coefficient γ, the TRK sum rule strength, and the centroid energy of the GDR of the fissioning system E_{cen}. They were varied as follows: $-0.5 \leq \beta \leq 0.5$,

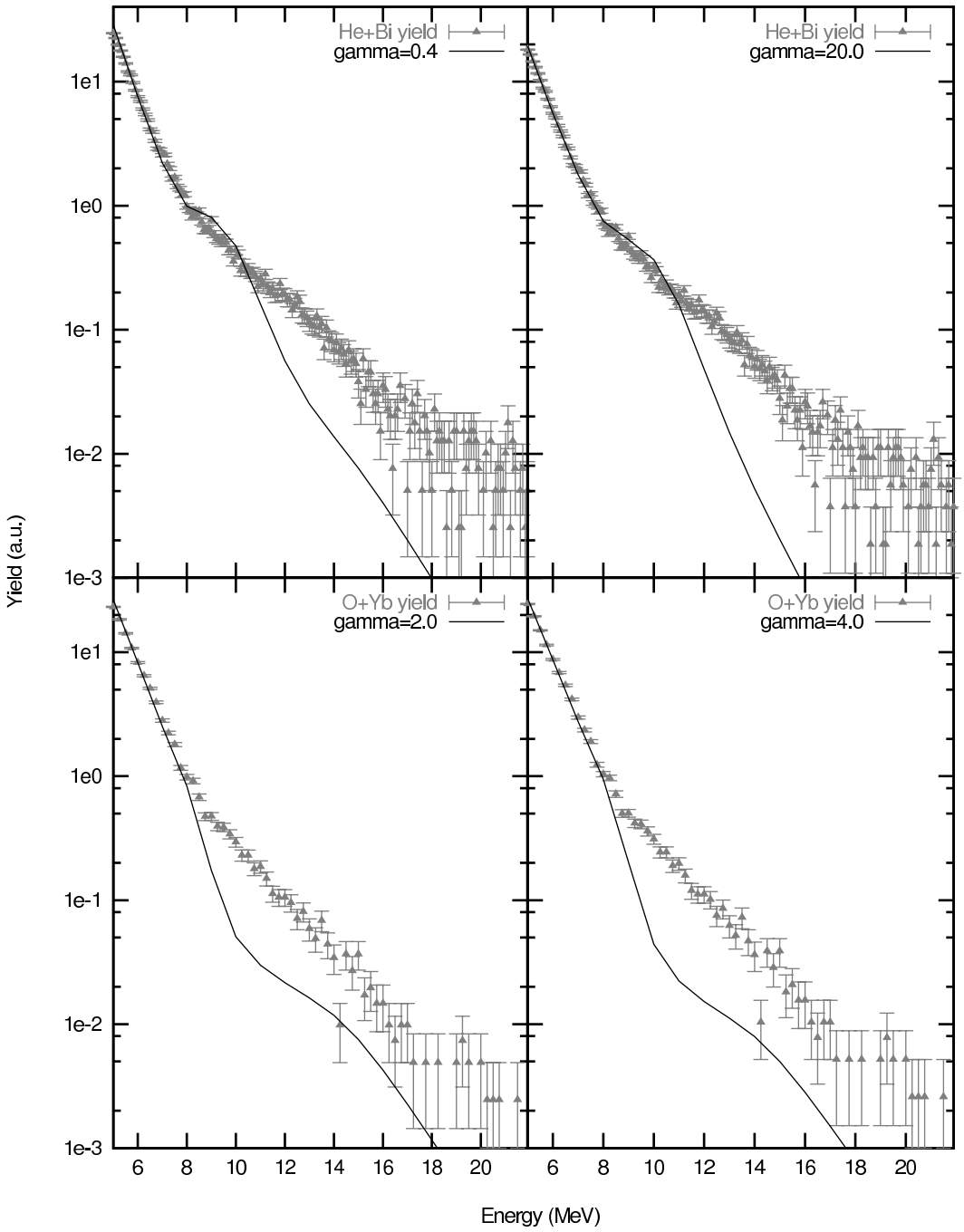

FIG. 57. Sample poor γ-ray fits for ^{4}He + ^{209}Bi and ^{16}O + ^{176}Yb obtained from MINUIT. The top two show the limits of varying γ in the He+Bi reaction. The bottom two show the mid-range of γ's for the O+Yb reaction.

$2 \leq \gamma \leq 20$, and $1.1 \leq TRK \leq 1.5$, with E_{cen} varying from 1.5 MeV below the ground state GDR energy to 0.5 MeV below. The procedure was to run all combinations of each, extract the χ^2/N, and inspect each fit visually to ensure meaningful fits.

Sample fits for ^{4}He + ^{209}Bi and ^{16}O + ^{176}Yb are shown in Figures 58 and 59, respectively. The plot in the lower right of each figure is the best obtainable fit, while the other three are the results of other parameter sets giving poorer fits. The final parameters are indicated in each plot, where "beta" is the deformation constant β, "TRK" denotes the multiplier of the TRK sum rule, "Ec" is short for E_{cen}, and "gam" denotes the friction coefficient extracted. The χ^2/N for each fit is plotted as a single point near the y axis in each plot. In both figures, it is apparent that no parameter set was able to reproduce all of the yield of GDR γ rays. While allowing the TRK sum rule strength to vary helped, the experimental spectra were still not reproduced even with a 50% increase. Increasing the TRK sum rule further might eventually find some parameter set that would fit the data much better. This however is undesirable since for these reactions one expects to observe little if any excess in sum rule strength.

In all cases, the calculations for the ^{4}He + ^{209}Bi system fail to explain the highest energy portion of the spectrum. Possibly this is due to an internuclear bremsstrahlung component in the data. Such components have been reported for lighter systems as a significant contributor for photon energies above 16 MeV [147]. For heavier systems, it is reasonable to expect that bremsstrahlung might influence the spectrum at still lower energies since the GDR contribution occurs at lower energies.

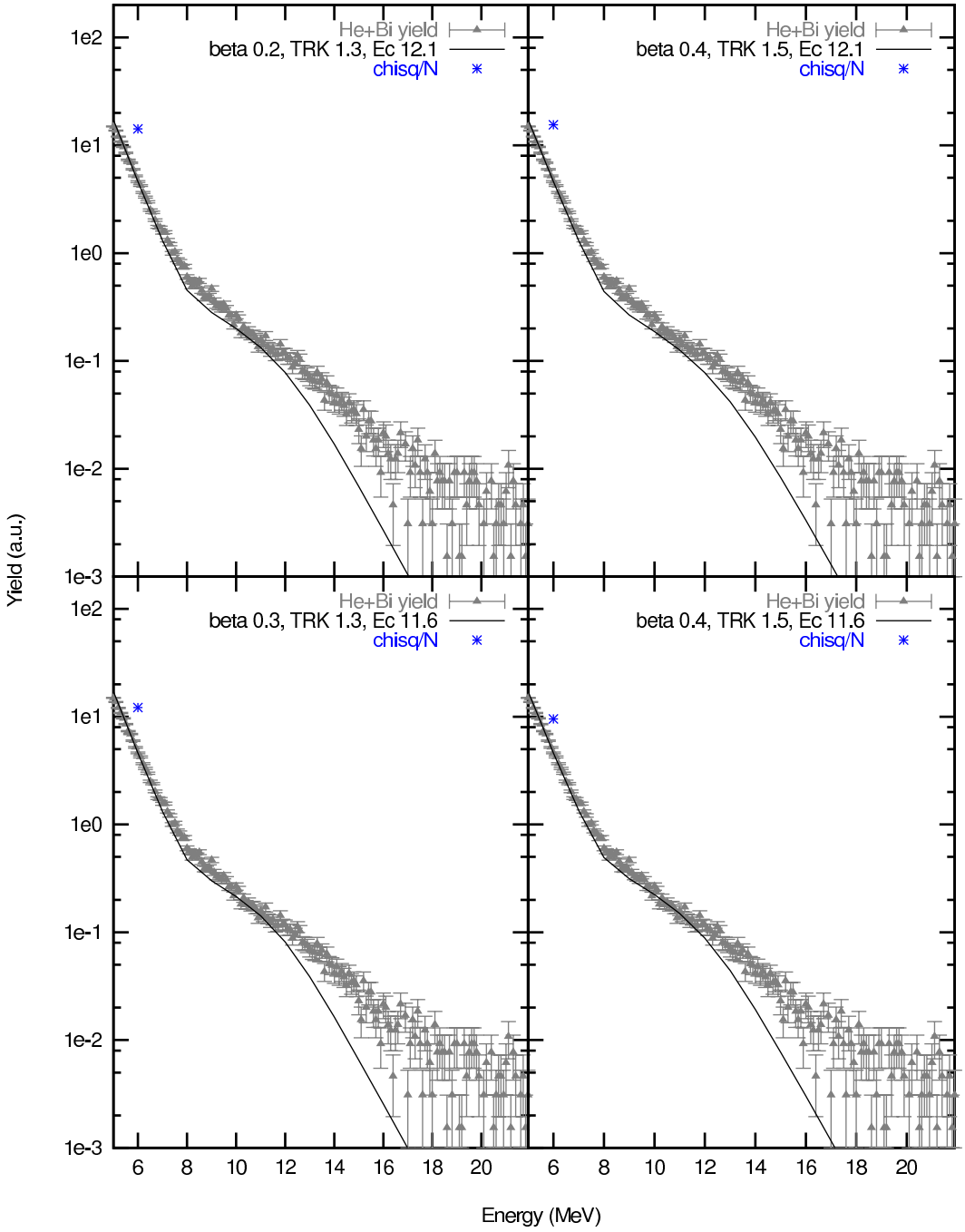

FIG. 58. Fits for ^{4}He + ^{209}Bi using various TRK strengths.

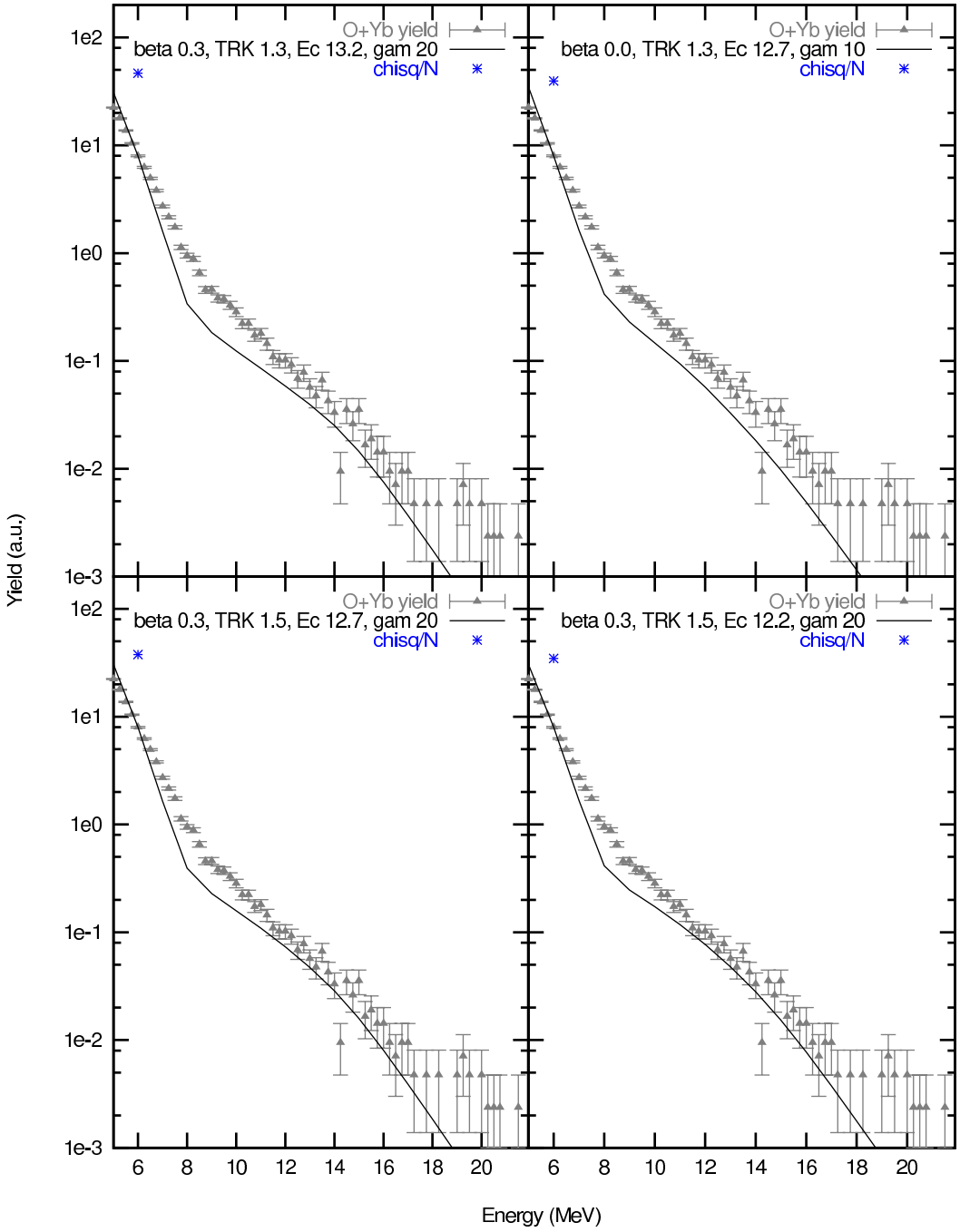

FIG. 59. Fits for ^{16}O + ^{176}Yb using various TRK strengths.

In contrast, for ^{16}O + ^{176}Ybthe fits do not reproduce the data very well in the vicinity of the region between the statistical and GDR portions of the spectrum. No reasonable variation of parameters removed this problem. The origin of this discrepancy is unknown.

Nevertheless, the fits in these two figures are far better than in Figure 57, though it was not possible to obtain the quality of fit seen for the ^{16}O + ^{208}Pb calculations. The χ^2/N values for these fits where only half as large as those obtained when using MINUIT linked to TIMCASC. Using the best fits as a starting point allows some estimates of the time scale for fission to be made.

V.8 Time Scale Extraction from TIMCASC Calculations

Comparing TIMCASC with the data led to a couple of options for determining the average fission lifetime of the compound systems. Since TIMCASC keeps track of both the time scales of each step in the cascade and their cross sections, an overall fission time scale for any given set of input parameters can be extracted in a straightforward manner. This is directly applicable to the neutron and γ-ray fits discussed in the previous sections.

Since TIMCASC reports the fission cross sections and the average fission time for each nucleus in the decay chain, the average fission time for a particular nucleus i produced in the decay cascade is given by

$$t_{f,i} = \frac{\sum_{E^*,J} \sigma_f(E^*,J)(t(E^*,J) + \Delta t(E^*,J))}{\sum_{E^*,J} \sigma_f(E^*,J)}, \tag{58}$$

with t and Δt defined as in Equation (54). Taking a nucleus which emitted a whole number x neutrons before fissioning, the average fission time $\tau_{xn,f}$ would therefore

be calculated in a straightforward manner. For a non-integer number of neutrons, interpolation (linear or exponential, as appropriate) between the two flanking whole-neutron evaporation time scales is all that is required. This is precisely the neutron method of determining fission time scales.

Taking a weighted average of $t_{f,i}$'s over the total fission cross section gives the total average fission time scale,

$$\tau_{f,tot} = \frac{\sum_i \sigma_{f,i} t_{f,i}}{\sum_i \sigma_{f,i}}, \tag{59}$$

where $\sigma_{f,i}$ denotes the fission cross section for nucleus i in the decay cascade. Values for $\tau_{f,tot}$ are strongly influenced by long fission times from a tail of long-lifetime decays with small, but finite, cross sections. While this perhaps more rigorously represents a true average lifetime for fission, it is less desirable for comparison with previous work than the neutron method since it is so strongly influenced by a small fraction of the calculated fission cross section. It is important to realize that in dealing with $\tau_{f,tot}$'s, the calculations are very sensitive to small errors in cross sections, since just the slightest overestimate of a cross section for a very long-lived state in the cascade can drastically affect the calculation. The neutron clock (i.e. $\tau_{xn,f}$) is not affected by later paths for fission and is not weighted by a tail of long-lifetime fission events. In comparison with the total average fission time scale given by Equation (59), it is perhaps better considered as a "most probable" value for the fission time scale rather than an average. The neutron clock also corresponds directly to the previous neutron time scale analyses. Furthermore, it is directly comparable to those GDR γ-ray studies which linked the GDR analysis to the neutron clock [27]. The remaining

TABLE 21. Fission time scales determined by neutron analysis. The $\tau_{f,tot}$ is the average time scale, while $\tau_{xn,f}$ is the value from the neutron clock method.

Reaction	γ	$\tau_{f,tot}$ (zs)	$\tau_{xn,f}$ (zs)
$^{16}O + ^{208}Pb$	20	170 ± 30	105 ± 10
$^{4}He + ^{209}Bi$	10	293 ± 35	72 ± 7
$^{16}O + ^{176}Yb$	20	49 ± 10	112 ± 12
$^{4}He + ^{188}Os$	10	18 ± 5	31 ± 4

TABLE 22. Fission time scales as determined using the GDR γ-ray fits. The τ's have the same significance as in Table 21.

Reaction	γ	$\tau_{f,tot}$ (zs)	$\tau_{xn,f}$ (zs)
$^{16}O + ^{208}Pb$	7	93 ± 27	67 ± 10
$^{4}He + ^{209}Bi$	20	253 ± 35	45 ± 9
$^{16}O + ^{176}Yb$	20	37 ± 9	84 ± 16

work using the GDR method has used a number of other means, largely unspecified, for producing the fission time scales. Van't Hof and co-workers are the only ones to have reported $\tau_{f,tot}$ values [32].

The results of both methods are given in Tables 21 and 22. The values for γ used in Table 21 are taken as those γ's which either came closest to reproducing the experimental ν_{pre}(e. g. for $^{4}He + ^{209}Bi$ and $^{16}O + ^{176}Yb$) or which intercepted the low end of the uncertainty in the experimental ν_{pre}(e. g. for $^{16}O + ^{208}Pb$ and $^{4}He + ^{188}Os$). These γ's are also close to the mid-range of the values listed in Table 19 for all but the $^{16}O + ^{208}Pb$case. For $^{16}O + ^{208}Pb$, the γ chosen is at the lower limit since no

upper limit was determined. Note that for both $\tau_{f,tot}$ and $\tau_{xn,f}$ in the neutron analysis (Table 21), the least fissile system has the shortest fission time scale. Because of the direct comparability of the neutron clock and the uncertainty with regards to the tail of long-lifetime events in the total average fission time scale, $\tau_{f,tot}$, the remaining discussion will only deal with $\tau_{f,tot}$.

Some general observations can be made from the extracted time scales for each system. Both the neutron analysis and the GDR γ-ray analysis show that for the oxygen-induced reactions, the system with higher angular momentum (^{16}O + ^{176}Yb) has the longer lifetime. Also, the oxygen-induced reactions take longer to fission than do the helium-induced reactions. The ^{4}He + ^{209}Bi system fissions nearly 1.5–2 times faster than either of the two oxygen-induced reactions. From the $\tau_{xn,f}$ value for the neutron method, one sees that the ^{4}He + ^{188}Os system fissions three times faster than the ^{16}O + ^{208}Pb system, depending upon which clock is used.

Another important observation is the fact that the neutron analysis does not give a consistently faster time scale for fission than the GDR analysis. In the case of ^{16}O + ^{208}Pb, this is to be expected given that the neutron data were only fitted successfully with somewhat higher friction coefficients than were necessary for the GDR analysis. Larger friction coefficients require longer time scales by their very nature. This is not addressed in previous works using either of the two methods nor in works discussing differences between the two. Still, while the GDR γ-ray method workers have all used some version of CASCADE, the neutron method workers have generally used statistical model codes other than CASCADE. This points to code

dependency in the calculations, perhaps arising from different implementations of either the friction coefficient itself or of the concept of time.

For the ^{4}He + ^{209}Bi and ^{16}O + ^{176}Yb systems, the values for γ are not the main determining factor in the quicker time scale, since their γ's are either longer or the same as for the neutron method. The difference arises from statistical considerations; i.e., raising the TRK sum rule increases its decay width relative to both neutron evaporation and fission. This has the effect of making GDR decay before fission more likely, taking away more excitation energy and making fission less likely at later steps. Therefore, fission at later decay steps is less favored and the apparent fission time scale is lowered.

Still, perhaps the most striking feature of the time scales of these two analyses arises from the reversal of the trend that GDR γ-ray analysis produces longer time scales for fission than does neutron analysis of time scales (see Chapter I). Previous results point to time scales produced from neutron analyses that are on average three times quicker than those arrived at via GDR γ-ray analysis. This is obviously not borne out here.

The time scales for the two types of analyses are also much closer than expected. The differences are only 33%, which while within the error bars of the data and analytical method, is probably an indicator of how different the two methods sample the evolution of the fissioning system. Previous works, as discussed in Chapter I, point to time scales produced from neutron analyses that are on average three times shorter than those arrived at via GDR γ-ray analysis. However, in comparisons made between those previous works it is important to note that the different analyses

not only discussed different reactions, but also used different statistical model codes, different experimental data sets, and different data reduction methods. The use in the current work of the same statistical model code, the same data reduction, and the same set of experimental data for these two disparate methods has thus proven to be quite a determining factor in evaluation of the previous discrepancies between the two methods.

The general result from all four systems, using both clocks and both analyses, is that fusion-fission reactions must take place on the order of 10^{-19} seconds. This is wholly consistent with the previous works discussed in Chapter I. It also supports the idea that fusion-fission time scales are a general property of excited systems and do not vary wildly for moderately different entrance channels.

As also discussed in Chapter I, the fission time τ_f is expected to be the sum of a variety of terms; i. e.,

$$\tau_f = \tau_{form} + \tau_{sadd} + \tau_{scis} + \tau_{acc}. \tag{60}$$

The present results and analysis do not allow for a separation of the second two terms. However, some crude estimates of the first and last terms are offered by the $\tau_{xn,f}$'s listed in Tables 21 and 22. Note that $\tau_{xn,f}$ is consistently lower for the ^{4}He-induced reactions. On average, $\tau_{xn,f} = 92 \pm 24$ zs for all the ^{16}O-induced reactions. In contrast $\tau_{xn,f} = 49 \pm 12$ zs for the ^{4}He-induced reactions. If the entire difference is due to compound nucleus reactions, one obtains $\tau_{form} = 43 \pm 26$ zs. In other works, τ_{form} combined with τ_{sadd} into a quantity τ_D, the transient delay time or fission delay.

Values reported for τ_D for the types of systems studied here have been in the range of 20–110 zs [8, 148], which is quite consistent with the above estimate of τ_{form}.

The quantity τ_{acc} can be estimated by comparing the $\tau_{xn,f}$ using the two separate methods. This yields $\tau_{acc} = 38 \pm 14$, 27 ± 11, and 28 ± 20 zs for $^{16}O + ^{208}Pb$, $^{4}He + ^{209}Bi$, and $^{16}O + ^{176}Yb$, respectively. The overall average is 31 ± 26 zs where the errors have been combined in quadrature. This is about three times as long as calculations of the time required for the fragments to reach 90% of their asymptotic velocity [117]. Still, the theoretical time for acceleration falls within the large error bars on τ_{acc} from these results, making it impossible to draw any inferences about complications arising from the dynamics at scission.

Given the large error bars, the above estimates must be regarded as very crude. Moreover, it should be pointed out that the estimates relied on calculations using quite different γ's and neglected the fact that the saddle point shapes are expected to be quite different for the various systems. This suggests that additional work is needed to clarify the situation. In that regard, it would be very useful to obtain both neutron and GDR γ-ray data for other light- and heavy-ion reactions.

CHAPTER VI

SUMMARY OF RESULTS

In this dissertation, the fission time scales were explored for several reactions: 133 MeV $^{16}O + ^{208}Pb$, 104 MeV $^{4}He + ^{209}Bi$, 133 MeV $^{16}O + ^{176}Yb$, and 104 MeV $^{4}He + ^{188}Os$. The choice of these widely different systems was motivated by several important factors.

First, the resulting compound systems are quite different. This is expected to produce quite different saddle point shapes. In the first two reactions, fission is a highly important process. The opposite is true for the latter two reactions. This is reflected in their saddle and scission point configurations. These two critical points for the two fissile systems are predicted to occur at very different deformations, while these points should be nearly coincident for the lighter systems. Comparison of the two types of systems could provide a measure of any fission time delay before the saddle point.

Second, use of both light and heavy ion projectiles provides insight into the influence of angular momentum on the fission lifetimes. Because of the low fissilities of the last two reactions, fission is expected to be confined to windows centered at the highest angular momenta. It is also important to note that the $^{16}O + ^{176}Yb$ and $^{4}He + ^{188}Os$ reactions produce the same compound system but with different angular momentum.

Third, the system $^{16}O + ^{208}Pb$ have been extensively studied in other work, thus allowing one to tie the current data with previous studies.

Two very different techniques were employed in the measurements. In one approach, the number of pre- and post-fission neutrons were used to clock the overall fission time. In the second method, GDR γ rays from the compound system were investigated to provide independent time scales.

In all cases, coincident fission fragments were detected using two PPAC's mounted in close geometry; neutrons were measured using eight large liquid scintillation detectors from the so-called DEMON array. The γ rays were detected using 144 elements from the U. S. National BaF_2 Array. Usable neutron data were obtained for all four reactions. Distinct GDR γ-ray bumps were observed for all the systems except $^{4}He + {}^{188}Os$. Unfortunately, the low fission cross section for the latter system made it impossible to obtain adequate statistics during the alloted running time, which was over a month.

The fission fragment masses and TKE's were reconstructed from the PPAC events. The results were in accord with systematics. After correcting for the thresholds and detector efficiencies, pre- and post-fission neutron multiplicities were extracted using moving source fits. The γ-ray response was determined using the γ-ray shower program EGS.

A qualitative analysis of the data showed that the GDR γ rays were insensitive to both exit channel mass asymmetry and TKE. This implies that the fission time scale does not depend on the final mass split and that most of the γ rays were emitted by the compound system (i.e. before fission). Similarly, ν_{pre} was insensitive to the exit channel mass asymmetry. The value of ν_{tot} does exhibit a TKE dependence, but this is expected due to energy conservation.

The fission time scales were extracted from the neutron data using the code TIMCASC. For ^{16}O + ^{208}Pb, ^{4}He + ^{209}Bi, ^{16}O + ^{176}Yb, and ^{4}He + ^{209}Bi this analysis gave fission time scales of 105 ± 10 zs, 72 ± 7 zs, 112 ± 12 zs, and 31 ± 4 zs, respectively. Ranges for the friction coefficient γ were also extracted from the neutron analysis and were determined to be approximately $\gamma_{O+Pb} > 25$, $7 > \gamma_{He+Bi} < 25$, $10 > \gamma_{O+Yb} < 30$, and $5 > \gamma_{He+Os} < 20$, respectively.

Using the same statistical model code and parameters, similar time scales were extracted using GDR γ-ray fits. For the same systems in order, the analysis yielded $\tau_{fiss} = 67 \pm 10$ zs, 45 ± 9 zs, and 84 ± 16 zs, while no value could be determined for the ^{4}He + ^{188}Os system due to poor statistics. The corresponding friction coefficients were 7 ± 3, 20 ± 10, and 20 ± 10, respectively.

Comparison of the time scales indicate that $\tau_{form} = 43 \pm 26$ zs while $\tau_{acc} = 31 \pm 26$ zs. Further investigation into light- and heavy-ion reactions should yield greater insight into these values. It would also be interesting to perform experiments with somewhat heavier projectiles (e.g. ^{28}Si, ^{32}S, and ^{40}Ar) to further investigate the effects of higher angular momentum upon the fission time scale.

Using the same experimental techniques and analysis procedure reverses the discrepancies between the two methods for determining τ_{fiss}. Hopefully further measurements will help in deciphering the various time scales in more detail.

REFERENCES

[1] L. L. Quill, Chem. Rev. **23**, 87 (1938).

[2] O. Hahn and F. Strassman, Naturwissenschaften **26**, 755 (1938).

[3] L. Meitner and O. R. Frisch, Nature (London) **143**, 239 (1939).

[4] O. R. Frisch, Nature (London) **143**, 276 (1939).

[5] N. Bohr and J. A. Wheeler, Phys. Rev. **56**, 426 (1939).

[6] R. Vandenbosch and J. R. Huizenga, *Nuclear Fission* (Academic Press, New York, 1973), and references therein.

[7] W. P. Zank, D. Hilscher, G. Ingold, U. Jahnke, M. Lehmann, and H. Rossner, Phys. Rev. C **33**, 519 (1986).

[8] D. J. Hinde, R. J. Charity, G. S. Foote, J. R. Leigh, J. O. Newton, S. Ogaza, and A. Chatterjee, Nucl. Phys. **A452**, 550 (1986).

[9] A. Gavron, A. Gayer, J. Boissevain, H. C. Britt, T. C. Awes, J. R. Beene, B. Cheynis, D. Drain, R. L. Ferguson, F. E. Obenshain, F. Plasil, G. R. Young, G. A. Petitt, and C. Butler, Phys. Rev. C **35**, 579 (1987).

[10] D. J. Hinde, D. Hilscher, and H. Rossner, Nucl. Phys. **A502**, 497c (1989).

[11] H. Rossner, D. Hilscher, D. J. Hinde, B. Gebauer, M. Lehmann, and W. Wilpert, Phys. Rev. C **40**, 2629 (1989).

[12] M. Strecker, R. Wien, and W. Scobel, Phys. Rev. C **41**, 2172 (1990).

[13] E. Mordhorst, M. Strecker, H. Frobeen, M. Gasthuber, W. Scobel, B. Gebauer, D. Hilscher, M. Lehmann, H. Rossner, and Th. Wilpert, Phys. Rev. C **43**, 716 (1991).

[14] D. J. Hinde, D. Hilscher, H. Rossner, B. Gebauer, M. Lehmann, and M. Wilpert, Phys. Rev. C **45**, 1229 (1992), and references therein.

[15] L. C. Vaz, D. Logan, E. Duek, J. M. Alexander, M. F. Rivet, M. S. Zisman, M. Kaplan, and J. W. Ball, Zeit. Phys. A **315**, 169 (1984).

[16] N. N. Ajitanand, J. M. Alexander, H. Delagrange, E. Duek, D. O. Eriksen, D. Guerreau, M. Kaplan, M. Kildir, L. Kowalski, R. Lacey, D. Logan, D. J.

Moses, G. F. Peaslee, L. C. Vas, and M. S. Zisman, Zeit. Phys. A **316**, 169 (1984).

[17] L. Schad, H. Ho, G. Y. Fan, B. Lindle, A. Pfoh, R. Wolski, and J. P. Wurm, Zeit. Phys. A **318**, 179 (1984).

[18] J. P. Lestone, J. R. Leigh, J. O. Newton, D. J. Hinde, J. X. Wei, J. X. Chen, S. Elfström, and D. G. Popescu, Phys. Rev. Lett. **67**, 1078 (1991).

[19] H. Ikezoe, N. Shikazono, Y. Nagame, T. Ohtsuki, Y. Sugiyama, Y. Tomita, K. Ideno, I. Kanno, H. J. Kim, B. J. Qi, and A. Iwamoto, Nucl. Phys. **A538**, 299c (1992).

[20] J. P. Lestone, J. R. Leigh, J. O. Newton, D. J. Hinde, J. X. Wei, J. X. Chen, S. Elfström, and M. Zielinska-Pfabé, Nucl. Phys. **A559**, 277 (1993).

[21] M. Gui, K. Hagel, R. Wada, Y. Lou, D. Utley, B. Xiao, J. Li, J. B. Natowitz, G. Enders, W. Kühn, V. Metag, R. Novotny, O. Schwalb, R. J. Charity, R. Freifelder, A. Gobbi, W. Henning, K. D. Hildebrand, R. Mayer, R. S. Simon, and J. P. Wessels, Phys. Rev. C **48**, 1791 (1993).

[22] A. Chatterjee, A. Navin, S. Kailas, P. Singh, D. C. Biswas, A. Karnik, and S. S. Kapoor, Phys. Rev. C **52**, 3167 (1995).

[23] M. Thoennessen, D. R. Chakrabarty, M. G. Herman, R. Butsch, and P. Paul, Phys. Rev. Lett. **59**, 2860 (1987).

[24] R. Butsch, D. J. Hofman, C. P. Montoya, P. Paul, and M. Thoennessen, Phys. Rev. C **44**, 1515 (1991).

[25] I. Diószegi, D. J. Hofman, C. P. Montoya, S. Schadmand, and P. Paul, Phys. Rev. C **46**, 627 (1992).

[26] D. J. Hofman, B. B. Back, C. P. Montoya, S. Schadmand, R. Varma, and P. Paul, Phys. Rev. C **47**, 1103 (1993).

[27] W. A. Turmel, Ph.D. Dissertation, Texas A&M University, unpublished (1993).

[28] D. J. Hofman, B. B. Back, I. Diószegi, C. P. Montoya, S. Schadmand, R. Varma, and P. Paul, Phys. Rev. Lett. **72**, 470 (1994).

[29] J. B. Fitzgerald, D. Habs, P. Reiter, D. Schwalm, P. Thirolf, and A. Wiswesser, *Proceedings of the Second International Conference on Dynamical Aspects*

of Nuclear Fission, Eds. J. Kristiak and B. I. Pustylnik, (JINR – Flerov Laboratory, Dubna, Russia, 1993), p. 68.

[30] J. Nestler, B. B. Back, K. S. Drese, D. J. Hofman, S. Schadmand, R. Varma and P. Paul, Phys. Rev. C **51**, 2218 (1995).

[31] C. R. Morton, A. Buda, P. Paul, N. P. Shaw, J. R. Beene, N. Gan, M. L. Halbert, D. W. Stracener, R. L. Varner, M. Thoennessen, and I. Diószegi, J. Phys. G: Nucl. Part. Phys. **23**, 1383 (1997).

[32] G. van 't Hof, J. C. S. Bacelar, I. Diószegi, M. N. Harakeh, W. H. A. Hesselink, N. Kalantar-Nayestanaki, A. Kugler, H. van der Ploeg, A. J. M. Plompen, and J. P. S. van Schagen, Nucl. Phys. **A638**, 613 (1998).

[33] M. Morjean, M. Chevallier, C. Cohen, D. Dauvergne, J. Dural, J. Galin, F. Goldenbaum, D. Jacquet, R. Kirsch, E. Lienard, B. Lott, A. Peghaire, Y. Perier, J. C. Poizat, G. Prevot, J. Remilleaux, D. Schmaus, and M. Toulenmonde, Nucl. Phys. **A630**, 200c (1998).

[34] P. Paul and M. Thoennessen, Ann. Rev. Nucl. Part. Sci. **44**, 65 (1994), and references therein.

[35] K. A. Snover, Ann. Rev. Nucl. Sci. **36**, 545(1986), and references therein.

[36] D. Hilscher and H. Rossner, Ann. Rev. Fr. **17**, 471 (1992), and references therein.

[37] H. A. Weidenmüller and Zhang Jing-Shang, Phys. Rev. C **29**, 879 (1984).

[38] H. A. Kramers, Physica **7**, 284 (1940).

[39] P. Grangé, S. Hassani, H. A. Weidenmuller, A. Gavron, J. R. Nix, and A. J. Sierk, Phys. Rev. C **34**, 209 (1986).

[40] A. Gavron, Nucl. Phys. **A502**, 515c (1989).

[41] R. J. Charity, Phys. Rev. C **51**, 217 (1995).

[42] A. K. Dhara, K. Krishnan, C. Bhattacharya, and S. Bhattacharya, Phys. Rev. C **57**, 2453 (1998).

[43] J. van der Plicht, H. C. Britt, M. M. Fowler, Z. Fraenkel, A. Gavron, J. B. Wilhelmy, F. Plasil, T. C. Awes, and G. R. Young, Phys. Rev. C **28**, 2022 (1983).

[44] F. Plasil, T. C. Awes, B. Cheynis, D. Drain, R. L. Ferguson, F. E. Obenshain, A. J. Sierk, S. G. Steadman, and G. R. Young, Phys. Rev. C **29**, 1145 (1984).

[45] K. T. Lesko, W. Henning, K. E. Rehm, G. Rosner, J. P. Schiffer, G. S. F. Stephans, B. Zeidman, and W. S. Freeman, Phys. Rev. Lett. **55**, 803 (1985).

[46] R. J. Charity, J. R. Leigh, J. J. M. Bokhorst, A. Chatterjee, G. S. Foote, D. J. Hinde, J. O. Newton, S. Ogaza, and D. Ward, Nucl. Phys. **A457**, 441 (1986).

[47] J. B. Natowitz, M. Gonin, M. Gui, K. Hagel, Y. Lou, D. Utley, and R. Wada, Phys. Lett. B **247**, 242 (1990).

[48] K.-T. Brinkmann, A. L. Caraley, B. J. Fineman, N. Gan, J. Velkovska, and R. L. McGrath, Phys. Rev. C **50**, 309 (1994).

[49] J. Galin, G. Ingold, U. Jahnke, D. Hilscher, M. Lehmann, H. Rossner, and E. Schwinn, Zeit. Phys. A **331**, 63 (1988).

[50] J. Piasecki, Phys. Rev. Lett. **66**, 1291 (1991).

[51] R. P. Schmitt, J. Boger, T. Botting, L. Cooke, B. Hurst, D. O'Kelly, B. K. Srivastava, and W. Turmel, *Proceedings of the Nuclear Chemical Award Symposium*, 209^{th} Meeting of the American Chemical Society, Anaheim, California (World Scientific, Singapore, 1995), p. 19.

[52] J. Galin, Nucl. Part. Phys. **20**, 1105 (1994), and references therein.

[53] E. Fermi, Z. Phys. **88**, 161 (1934).

[54] V. F. Weisskopf, Phys. Rev. **52**, 295 (1937).

[55] T. Ericson, Phil. Mag. **9**, 425 (1960).

[56] F. Pühlofer, Nucl. Phys. **A280**, 276 (1977).

[57] A. Gavron, Phys. Rev. C **21**, 230 (1980).

[58] D. Hilscher, H. Rossner, B. Cramer, B. Gebauer, U. Jahnke, M. Lehmann, E. Schwinn, M. Wilpert, Th. Wilpert, H. Frobeen, E. Mordhorst, and W. Scobel, Phys. Rev. Lett. **62**, 1099 (1989).

[59] D. J. Hinde, H. Ogata, M. Tanaka, T. Shimoda, N. Takahashi, A. Shinohara, S. Wakamatsu, K. Katori, and H. Okamura, Phys. Rev. C **39**, 2268 (1989).

[60] V. A. Rubchenya, A. V. Kuznetsov, W. H. Trzaska, D. N. Vakhtin, A. A. Alexandrov, I. D. Alkhazov, J. Äystö, S. V. Khlebnikov, V. G. Lyapin, O. I. Osetrov, Yu. E., Penionzhkevich, Yu. V. Pyatkov, and G. P. Tiourin, Phys. Rev. C **58**, 1587 (1998).

[61] A. Gavron, A. Gayer, J. Boissevain, H. C. Britt, J. R. Nix, A. J. Sierk, P. Grangé, S. Hassani, H. A. Weidenmuller, J. R. Beene, B. Cheynis, D. Drain, R. L. Ferguson, F. E. Obenshain, F. Plasil, G. R. Young, G. A. Petitt, and C. Butler, Phys. Lett. B **176**, 312 (1986).

[62] P. Grangé and H. A. Weidenmuller, Phys. Lett. **96B**, 26 (1980).

[63] W. J. Swiatecki, Nucl. Phys. **A428**, 199c (1984), and references therein.

[64] J. R. Nix and A. J. Sierk, Phys. Rev. C **21**, 396 (1980), and references therein.

[65] G. C. Baldwin and G. S. Klaiber, Phys. Rev. **71**, 3 (1947).

[66] R. E. Bertrand, Ann. Rev. Nucl. Sci. **26**, 457 (1976).

[67] S. S. Hanna, Lect. Notes Phys. **61**, 725 (1977).

[68] F. E. Bertrand, Nucl. Phys. **A354**, 129c (1981).

[69] J. Speth and A. van der Woude, Rep. Prog. Phys. **44**, 719 (1981).

[70] J. J. Gaardhøje, Ann. Rev. Nucl. Part. Sci. **42**, 483 (1992).

[71] M. Goldhaber and E. Teller, Phys. Rev. **74**, 1046 (1948).

[72] H. Steinwedel and J. H. D. Jensen, Z. Naturforschung **a**, 413 (1950).

[73] B. L. Berman and S. C. Fultz, Rev. Mod. Phys. **47**, 713 (1975).

[74] W. D. Myers, W. J. Swiatecki, T. Kodama, L. J. El-Jaick, and E. R. Hilf, Phys. Rev. C **15**. 2032 (1977).

[75] J. S. Levinger, in *Nuclear Photo-Disintegration*, (Oxford University Press, Oxford, 1960), p. 37.

[76] D. Brink, Ph.D. Dissertation, Oxford University, unpublished (1955).

[77] F. S. Dietrich, J. C. Browne, W. J. O'Connell, and M. J. Kay, Phys. Rev. C **10**, 795 (1974).

[78] J. O. Newton, B. Herskind, R. M. Diamond, E. L. Dines, J. E. Draper, K. H. Lindberger, C. Schuck, S. Shih, F. S. Stephens, Phys. Rev. Lett. **46**, 1383 (1981).

[79] T. S. Tveter, J. J. Gaardhøje, A. Maj, T. Ramsøy, A. Atac, J. Bacelar, A. Bracco, A. Buda, F. Camera, B. Herskind, W. Korten, W. Królas, A. Menthe, B. Million, H. Nifenecker, M. Pignanelli, J. A. Pinston, H. Van der Ploeg, F. Schussler, and G. Sletten, Phys. Rev. Lett. **76**, 1035 (1996).

[80] R. P. Schmitt, W. Turmel, L. Cooke, J. Boger, T. Botting, B. Hurst, and D. O'Kelly, *Proceedings of the Second International Conference on Dynamical Aspects of Nuclear Fission*, Eds. J. Kristiak and B. I. Pustylnik, (JINR – Flerov Laboratory, Dubna, Russia, 1993), p. 79.

[81] W. W. Wilke, J. R. Birkelund, H. J. Wollersheim, A. D. Hoover, J. R. Huizenga, W. U. Schröder, and L. E. Tubbs, At. Data Nucl. Data Table **25**, 389 (1980).

[82] D. S. Burnett, Phys. Rep. **134**, B952 (1964).

[83] A. Khodai-Joopari, Ph.D. Dissertaion, University of California, Berkeley, unpublished (1966).

[84] B. G. Glagola, B. B. Back, and R. R. Betts, Phys. Rev. C **29**, 486 (1984).

[85] L. G. Moretto, K. X. Jing, R. Gatti, G. J. Wozniak, and R. P. Schmitt, Phys. Rev. Lett. **75**, 4186 (1995).

[86] D. Durand, *Proceedings of the International Conference on New Nuclear Physics with Advanced Techniques*, Eds. F. A. Beck, S. Kossionides and C. A. Kalfas, (World Scientific, Singapore, 1992), p. 173.

[87] C. Mazur and M. Ribrag, Nucl. Inst. Meth. **212**, 203 (1983).

[88] G. C. Chubarian, Texas A&M Cyclotron Institute, private communication (1998).

[89] P. J. Nolan, F. A. Beck, and D. B. Fossan, Ann. Rev. Nucl. Part. Sci. **45**, 561 (1994).

[90] C. W. Beausang and J. Simpson, J. Phys. **G22**, 527 (1996).

[91] M. Laval, M. Moszynski, R. Allemand, E. Cormoreche, P. Guinet, R. Odru, and J. Vacher, Nucl. Inst. Meth. **206**, 169 (1983).

[92] S. Kubota, M. Suzuki, J.-Z. Ruan, F. Shiraishi, and Y. Takami, Nucl. Inst. Meth. **A242**, 291 (1986).

[93] J. Schoemaker, K. Wolf, and R. Choudhury, *Progress in Research, April 1, 1990 – March 31, 1991*, prepared by the Cyclotron Institute staff, (Texas A&M University, College Station, TX) p. 108.

[94] M. Halbert and R. L. Varner, Oak Ridge National Laboratory (Oak Ridge, TN), private communication (1996).

[95] DEMON Proposal, Louvain-la-Neuve and Strasbourg internal report (Universite Catholique de Louvain, Louvain, France, 1988).

[96] R. A. Winyard and G. W. McBeth, Nucl. Inst. Meth. **95**, 141 (1971).

[97] R. A. Winyard, J. E. Lutkin, and G. W. McBeth, Nucl. Inst. Meth. **98**, 525 (1972).

[98] S. Mouatassim, G. J. Costa, G. Guillame, B. Heusch, A. Huck, and M. Moszynski, Nucl. Inst. Meth. **A359**, 530 (1995).

[99] M. Moszynski, G. Bizard, G. J. Costa, D. Durand, Y. El Masri, G. Guillame, F. Hanappe, B. Heusch, A. Huck, J. Péter, Ch. Ring, and B. Tamain, Nucl. Inst. Meth. **A317**, 262 (1992).

[100] I. Tilquin, Y. El Masri, M. Parlog, Ph. Collon, M. Hadri, Th. Keutgen, J. Lehmann, P. Leleux, P. Lipnik, A. Ninane, F. Hanappe, G. Bizard, D. Durand, P. Mosrin, J. Péter, R. Régimbart, and B. Tamain, Nucl. Inst. Meth. **A365**, 446 (1995).

[101] M. Moszynski, G. J. Costa, G. Guillame, B. Heusch, A. Huck, and S. Mouatassim, Nucl. Inst. Meth. **A307**, 97 (1991).

[102] M. Moszynski, G. J. Costa, G. Guillame, B. Heusch, A. Huck, and S. Mouatassim, Nucl. Inst. Meth. **A350**, 226 (1994).

[103] L. Donadille, Ph.D. Dissertation, Universite Paris 7 - Denis Diderot, unpublished (1998).

[104] P. Désesquelles, A. J. Cole, A. Dauchy, A. Giorni, D. Heuer, A. Lleres, C. Morand, J. Saint-Martin, P. Stassi, J. B. Viano, B. Chambon, B. Cheynis, D. Drain, and C. Pastor, Nucl. Inst. Meth. **A307**, 366 (1991).

[105] W. Mills, Jr., and R. Mackin, Jr., Phys. Rep. **95**, 1206 (1954).

[106] R. Bent, T. Bonner, J. McCrary, and W. Ramken, Phys. Rep. **100**, 771 (1955).

[107] H. Jabs, M.S. Thesis, Texas A&M University, unpublished (1997).

[108] G. G. Chubaryan, V. A. Gorshkov, V. E. Zhuchko, S. M. Lukjanov, H. G. Ortlepp, V. S. Salamatin, and D. Wolffhard, Communications of the Joint Institute for Nuclear Research, P13-92-18, unpublished (Dubna, Russia, 1992).

[109] K. Hagel, LISA User Manual, Texas A&M Cyclotron Institute, unpublished (1990).

[110] I. Tilquin-Jadin, Ph.D. Dissertation, Universite Catholique de Louvain, unpublished (1997).

[111] E. V. Benton and R. P. Henke, Nucl. Inst. Meth. **76**, 87 (1969).

[112] V. E. Viola, K. Kwiatkowski, and M. Walker Phys. Rev. C **31**, 1550 (1985).

[113] K. L. Wolf, Texas A&M Cyclotron Institute, private communication (1997).

[114] P. Glässel, R. Schmidt-Fabian, D. Schwalm, D. Habs, and H. V. Helmdt, Nucl. Phys. **A502**, 315c (1989).

[115] R. L. Ford and W. R. Nelson, Stanford Linear Accelerator Report 210, unpublished (Stanford, 1978).

[116] E. Holub, D. Hilscher, G. Ingold, U. Jahnke, H. Orf, and H. Rossner, Phys. Rev. C **28**, 252 (1983).

[117] D. J. Hinde, R. J. Charity, G. S. Foote, J. R. Leigh, J. O. Newton, S. Ogaza, and A. Chatterjee, Phys. Rev. Lett. **52**, 986 (1984).

[118] D. J. Hinde, J. R. Leigh, J. J. M. Bokhorst, J. O. Newton, R. Walsh, and J. E. Boldman, Nucl. Phys. **A472**, 318 (1987).

[119] J. O. Newton, D. J. Hinde, R. J. Charity, J. R. Leigh, J. J. M. Bokhorst, A. Chatterjee, G. S. Foote, and S. Ogaza, Nucl. Phys. **A483**, 126 (1988).

[120] S. Borne, Nucl. Inst. Meth. **A385**, 339 (1997).

[121] E. Martinez, Nucl. Inst. Meth. **A385**, 345 (1997).

[122] R. A. Cecil, B. D. Anderson, and R. Madey, Nucl. Inst. Meth. **161**, 439 (1979).

[123] J. B. Fitzgerald, D. Habs, F. Heller, P. Reiter, D. Schwalm, P. Thirolf, and A. Wiswesser, Zeit. Phys. A **355**, 401 (1996).

[124] A. Hotzel, P. Thirolf, Ch. Ender, D. Schwalm, M. Mutterer, P. Singer, M. Klemens, J. P. Theobald, M. Hesse, F. Gønnenwein, and H. v. d. Ploeg, Zeit. Phys. A **356**, 299 (1996).

[125] P. Singer, M. Mutterer, Yu. N. Kopach, M. Klemens, A. Hotzel, D. Schwalm, P. Thirolf, and M. Hesse, Zeit. Phys. A **359**, 41 (1997).

[126] R. Butsch, M. Thoennessen, D. R. Chakrabarty, M. G. Herman, and P. Paul, Phys. Rev. C **41**, 1530 (1990).

[127] D. J. Hofman, B. B. Back, and P. Paul, Phys. Rev. C **51**, 2597 (1995).

[128] J. B. Fitzgerald, Ph.D. Dissertation, University of Manchester, unpublished (1991).

[129] D. J. Hinde, H. Ogata, M. Tanaka, T. Shimoda, N. Takahashi, A. Shinohara, S. Wakamatsu, K. Katori, and H. Okamura, Phys. Rev. C **37**, 2923 (1988).

[130] C. J. Bishop, I. Halpern, R. W. Shaw Jr., and R. Vandenbosch, Nucl. Phys. **A278**, 161 (1972).

[131] D. Ward, R. J. Charity, D. J. Hinde, J. R. Leigh, and J. O. Newton, Nucl. Phys. **A403**, 189 (1983).

[132] F. Hanappe, Université Louis Pasteur (Strasbourg Cedex, France), private communication (1999).

[133] H. Eyring, J. Chem. Phys. **3**, 107 (1935).

[134] B. H. Mahan, J. Chem. Ed. **51**, 711 (1974).

[135] V. M. Strutinsky, Phys. Lett. **47B**, 121 (1973).

[136] S. Cohen, F. Plasil, and W. J. Swiatecki, Ann. Phys. (N.Y.) **82**, 557 (1974).

[137] J. P. Lestone, Phys. Rev. C **59**, 1540 (1999).

[138] B. J. Hurst, Ph.D. Dissertation, Texas A&M University, unpublished (1996).

[139] R. P. Schmitt, G. Mouchaty, and D. R. Haenni, Nucl. Phys. **A427**, 614 (1984).

[140] A. J. Sierk, Phys. Rev. C **33**, 2039 (1986).

[141] F. James and M. Roos, Comp. Phys. Comm. **10**, 343 (1975).

[142] D. R. Chakrabarty, S. Sen, M. Thoennessen, N. Alamanos, P. Paul, R. Schicker, J. Stachel, and J. J. Gaardhøje, Phys. Rev. C **36**, 1886 (1987).

[143] G. Feldman, K. A. Snover, J. A. Behr, C. A. Gossett, J. H. Gundlach, and M. Kicińska-Habior, Phys. Rev. C **47**, 1436 (1993).

[144] M. Kicińska-Habior, K. A. Snover, J. A. Behr, C. A. Gossett, J. H. Gundlach, and G. Feldman, Phys. Rev. C **45**, 569 (1992).

[145] M. Kicińska-Habior, K. A. Snover, J. A. Behr, C. A. Gossett, Y. Alhassid, and N. Whelan, Phys. Lett. B **308**, 225 (1993).

[146] G. R. Satchler, Phys. Rep. **14**, 99 (1974), and references therein.

[147] G. Enders, F. D. Berg, K. Hagel, W. Kühn, V. Metag, R. Novotny, M. Pfeiffer, O. Schwalb, R. J. Charity, A. Gobbi, R. Freifelder, W. Henning, K. D. Hildenbrand, R. Holzmann, R. S. Mayer, R. S. Simon, J. P. Wessels, G. Casini, A. Olmi, and A. A. Stefanini, Phys. Rev. Lett. **69**, 249 (1992).

[148] M. Thoennessen, J. R. Beene, F. E. Bertrand, C. Baktash, M. L. Halbert, D. J. Horen, D. G. Sarantites, W. Spang, and D. W. Stracener, Phys. Rev. Lett. **70**, 4055 (1993).

APPENDIX A

ALTERNATE SEMI-CLASSICAL DERIVATION OF TST

From semi-classical statistical mechanics, the probability of finding a system in a particular point in phase space is [134]

$$\frac{d^{6n}N}{N} = \frac{e^{-H/T}dq_1 \ldots dp_{3n}/\hbar^{3n}}{\int \ldots \int e^{-H/T}dq_1 \ldots dp_{3n}/\hbar^{3n}}, \tag{61}$$

where n is the number of degrees of freedom, N is the number of systems, and H is the Hamiltonian.

For a system with one degree of freedom (reaction coordinate, or fission mode), the rate $-\frac{dN}{dt}$ at which the system passes through a surface S is obtained by integrating Equation (61) over $dq_2 \ldots dp_{3n}$ where p_1 takes only position values. If we can write

$$H = H' + \frac{p_1^2}{2m}, \tag{62}$$

then Equation (61) yields

$$-\frac{dN}{dt} = \frac{N}{m_1 h}\int_0^\infty p_1 e^{\frac{p_1^2}{2m}} \frac{\int \ldots \int e^{-H/T}dq_1 \ldots dp_{3n}/n^{3n-1}}{\int \ldots \int e^{-H/T}dq_1 \ldots dp_{3n}/n^{3n}}, \tag{63}$$

since

$$\frac{dq_1}{dt} = \frac{m_1 dp_1}{dt}. \tag{64}$$

Integrating over p_1 yields

$$-\frac{dN}{dt} = \frac{T}{h}\frac{\int \ldots \int `}{\int \ldots \int}. \tag{65}$$

Now the phase space integrals can be identified with partition functions of the form

$$\int \ldots \int e^{-H/T}dv \approx \sum_E \omega(E)e^{-E/T} \tag{66}$$

where dv is the differential in coordinates and momenta and $\omega(E)$ is the degeneracy.

It is well known that $\omega(E)e^{-E/T}$ is a sharply peaked function of E and the $\omega(E)$ can be replaced by the level density [ref McQuarrie]. Thus

$$-\frac{dN}{dt} = \frac{NT}{h}\frac{\rho_f}{\rho_{CN}}. \tag{67}$$

Also,

$$-\frac{dN}{dt} = N\lambda = \frac{N}{\tau} = \frac{N\Gamma}{\hbar}, \tag{68}$$

giving

$$\Gamma = \frac{\rho_f}{2\pi\rho_{CN}}. \tag{69}$$

If there is a barrier at the saddle, B_f, then

$$H' = H'' + B_f \tag{70}$$

and one obtains

$$\Gamma_f = \frac{T}{2\pi}e^{-B_f/T}. \tag{71}$$

Note that this is of the same form as is used in Equations (8)–(10).

Equation (71) does not properly account for the zero of potential energy, which means that the limits of p_1 are not 0 to ∞. Proper accounting for these limits gives [135]

$$\Gamma_f = \frac{h\omega_{eq}}{2\pi}e^{-B_f/T}. \tag{72}$$

VITA

Tye William Botting was born in Anacortes, Washington on June 6, 1965. He attended Texas A&M University, College Station, Texas and graduated in August 1987 with a Bachelor of Science in chemistry. In January 1990 he enrolled at Texas A&M University to pursue a Doctor of Philosophy program in chemistry. He received his Ph.D. in chemistry from Texas A&M University, College Station, Texas in December 1999. Requirements for the degree were completed with the support of the Robert Welch Foundation and the United States Department of Energy. His permanent address is 1808 Carrabba St., Bryan, TX 77803-1995. He can also be reached at the Nuclear Science Center, Texas A&M University, Building 1307, Nuclear Science Road, College Station, Texas 77843-3575.